JOURNAL OF PETROLOGY | VOLUME 00 | NUMBER 0 | PAGES 1–39 | 2009 | doi:10.1093/petrology/egp008
Journal of Petrology Advance Access published March 9, 2009

Melting History and Magmatic Evolution of Basalts and Picrites from the Accreted Wrangellia Oceanic Plateau, Vancouver Island, Canada

ANDREW R. GREENE[1]*, JAMES S. SCOATES[1], DOMINIQUE WEIS[1], GRAHAM T. NIXON[2] AND BRUNO KIEFFER[1]

[1]PACIFIC CENTRE FOR ISOTOPIC AND GEOCHEMICAL RESEARCH, DEPARTMENT OF EARTH AND OCEAN SCIENCES, UNIVERSITY OF BRITISH COLUMBIA, VANCOUVER, BC, V6T1Z4, CANADA

[2]BRITISH COLUMBIA GEOLOGICAL SURVEY, P.O. BOX 9320, STN PROV GOVT, VICTORIA, BC, V8W9N3, CANADA

RECEIVED MARCH 18, 2008; ACCEPTED JANUARY 23, 2009

The accreted Wrangellia oceanic plateau in the Pacific Northwest of North America provides important insights into the volcanic architecture of major oceanic plateaus, as well as the nature of their mantle source, conditions of melting and subsequent magmatic evolution. The ~20 000 km^2 Karmutsen Formation flood basalts (Vancouver Island) were emplaced at c. 225–230 Ma onto Middle Triassic marine sediments and Late Devonian to Early Permian island-arc volcanic and sedimentary sequences, and are overlain by Late Triassic platformal carbonates. The basalts form an emergent sequence consisting of a basal sediment–sill complex (600–900 m thick), pillowed and massive submarine flows (>2·5 km), pillow breccia and hyaloclastite (<1·5 km), and massive subaerial flows (<2·5 km). Although the Karmutsen Formation is predominantly composed of tholeiitic basalt, the submarine part of the stratigraphy on northern Vancouver Island also contains picritic basalts. These high-MgO (9–20 wt %) lavas are depleted in light rare earth elements (LREE; $La/Yb_{CN} = 0{\cdot}5 \pm 0{\cdot}2$), whereas the tholeiitic lavas (6–8 wt % MgO) are LREE-enriched ($La/Yb_{CN} = 2{\cdot}2 \pm 0{\cdot}3$). Both lava groups have overlapping initial $\varepsilon_{Hf}(+10{\cdot}3 \pm 2{\cdot}1)$ and $\varepsilon_{Nd}(+7{\cdot}7 \pm 1{\cdot}3)$, indicating a common, plume-type Pacific mantle source with geochemical characteristics similar to the source of basalts from the Ontong Java and Caribbean plateaus. Major-element modeling results indicate that the picrites formed by extensive melting (23–27%) of anomalously hot mantle (~1500°C), which is consistent with a mantle plume initiation model for formation of the Karmutsen flood basalts on Vancouver Island. Trace element constraints indicate that the picrites require melting of a depleted spinel lherzolite source, whereas the tholeiitic basalts involved melting of garnet and spinel lherzolite. The tholeiitic basalts underwent significant fractional crystallization (>50%) and the fractionated residues may be represented by high-velocity rocks beneath Vancouver Island identified from seismic reflection studies.

KEY WORDS: *Karmutsen Formation; mantle plume; large igneous province; picrite; tholeiitic basalt*

INTRODUCTION

Oceanic plateaus are transient large igneous provinces that together with continental flood basalts represent the products of the largest magmatic events preserved on Earth from the Phanerozoic era. There are some 10 oceanic plateaus that have formed in the last 145 Myr, ranging in size from 100 000 to 2×10^6 km^2, and collectively they cover an area of about 10×10^6 km^2 (~3%) of the ocean basins, mostly in the Pacific and Indian oceans (e.g. Eldholm & Coffin, 2000). Oceanic plateaus form submarine or subaerial flood basalt sequences that can be ≥6 km thick, with total crustal thicknesses (extrusive plus intrusive rocks) of 8–33 km (e.g. Coffin & Eldholm, 1994). Several key aspects of most large igneous provinces are that they form as a

*Corresponding author. E-mail: agreene@eos.ubc.ca

result of unusually high melt production rates, are predominantly basaltic in composition, and their formation is not directly attributable to seafloor spreading processes (e.g. Saunders, 2005). The high melt production rates are best explained by high mantle source temperatures in rapidly upwelling mantle (i.e. mantle plumes); direct evidence of high mantle temperatures is the eruption of primitive, high-MgO lavas (Kerr & Mahoney, 2007). Studies of oceanic plateaus can be used to constrain aspects of mantle plume-related magmatism, including the composition of the mantle source involved, the temperature and depth of melting, the volume of magma and melt production rates, and the mechanisms of emplacement of voluminous lava sequences. From a geochemical perspective, the study of oceanic plateaus is important because the chemistry of the lavas has generally been unaffected by continental crustal contamination.

At present, one of the great challenges in studying oceanic plateaus in the ocean basins is the difficulty in drilling to depths of more than a few hundred meters into the basaltic basement rocks (e.g. Kerguelen, Ontong Java). Accreted sections of oceanic plateaus (e.g. Caribbean, Ontong Java) provide an opportunity to closely examine their volcanic stratigraphy. Wrangellia flood basalts in the Pacific Northwest of North America are part of a major large igneous province that erupted in a marine setting in the Late Triassic (*c.* 225–231 Ma) and accreted to western North America in the Late Jurassic or Early Cretaceous (Richards *et al.*, 1991). Although their original areal distribution was probably considerably larger, much of the original stratigraphic thickness (~6 km on Vancouver Island; ~3·5 km in Alaska) is intact. Current exposures of the flood basalts are preserved in a narrow belt over 2300 km in length, resulting from transform fault motions after accretion, which extends from southern British Columbia through the Yukon and into Alaska. Richards *et al.* (1991) proposed a plume initiation model for the Wrangellia flood basalts based on the short duration and estimated high eruption rate of the volcanism, evidence of uplift prior to volcanism, and lack of evidence of associated rifting (i.e. few dikes and abundant sills).

The Wrangellia flood basalts are perhaps the most extensive accreted remnants of an oceanic plateau in the world where parts of the entire volcanic stratigraphy are exposed; however, they have been the focus of few integrated field, geochemical, and radiogenic isotopic studies. The internal architecture of oceanic plateaus can provide constraints on the sequence of melting events associated with mantle plumes that occur beneath the oceans in an analogous way to the use of continental flood basalts to elucidate the sequential development of mantle plumes and rifting within continental lithosphere (e.g. Peate, 1997; Storey *et al.*, 1997). The internal stratigraphy of continental flood basalts is far more complex than previously realized (e.g. Jerram & Widdowson, 2005) and, because of their relative inaccessibility, the structure of flood basalt sequences in oceanic plateaus is not well known. In this study, we examine the field relationships, petrography, major and trace elements, and Sr–Nd–Hf–Pb isotopic compositions of Wrangellia flood basalts from various areas of Vancouver Island to assess the nature of the mantle source, conditions of melting, and magmatic history of the basalts in the context of the construction of this major oceanic plateau. This study is part of a comprehensive research project on the nature, origin and evolution of the Triassic Wrangellia flood basalt province in British Columbia, Yukon and Alaska (Greene *et al.*, 2008, 2009).

GEOLOGICAL SETTING

Wrangellia on Vancouver Island

Wrangellia flood basalts form the core of the Wrangellia terrane, or Wrangellia, one of the largest outboard terranes accreted to western North America (Jones *et al.*, 1977). Middle to Late Triassic flood basalts extend in a discontinuous belt from Vancouver and Queen Charlotte Islands (Karmutsen Formation), through SE Alaska and SW Yukon, and into the Wrangell Mountains, Alaska Range, and Talkeetna Mountains in east and central Alaska (Nikolai Formation; Fig. 1).

Wrangellia covers ~80% of Vancouver Island, which is 460 km long by 130 km wide (Fig. 1). Wrangellia is the uppermost sheet of a stack of SW-vergent thrust sheets that form the crust of Vancouver Island and has a cumulative thickness of >10 km (Monger & Journeay, 1994). Pre-Karmutsen units of Wrangellia on Vancouver Island include Devonian arc sequences of the Sicker Group and Mississippian to Early Permian siliciclastic and carbonate rocks of the Buttle Lake Group (Muller, 1980; Sutherland-Brown *et al.*, 1986). These Paleozoic sequences have variable estimated thicknesses (~2–5 km; Muller, 1980; Massey, 1995a) and are exposed only on central and southern Vancouver Island (Fig. 1). The Karmutsen Formation is overlain by the shallow-water Quatsino limestone (30–750 m) and shallow- to deeper-water Parson Bay Formation (~600 m), which is intercalated with and overlain by Bonanza arc volcanics (169–202 Ma; Nixon *et al.*, 2006*b*). Bonanza arc plutonic rocks (167–197 Ma) also intrude the Karmutsen Formation and are some of the youngest units of Wrangellia that formed prior to accretion with North America (Nixon *et al.*, 2006b). Following accretion, Wrangellia units were intruded by the predominantly Cretaceous Coast Plutonic Complex (Wheeler & McFeely, 1991).

The Karmutsen Formation (19 142 km^2; calculation based on digital geological compilations) is composed of basal sediment–sill complexes, a lower unit of pillowed

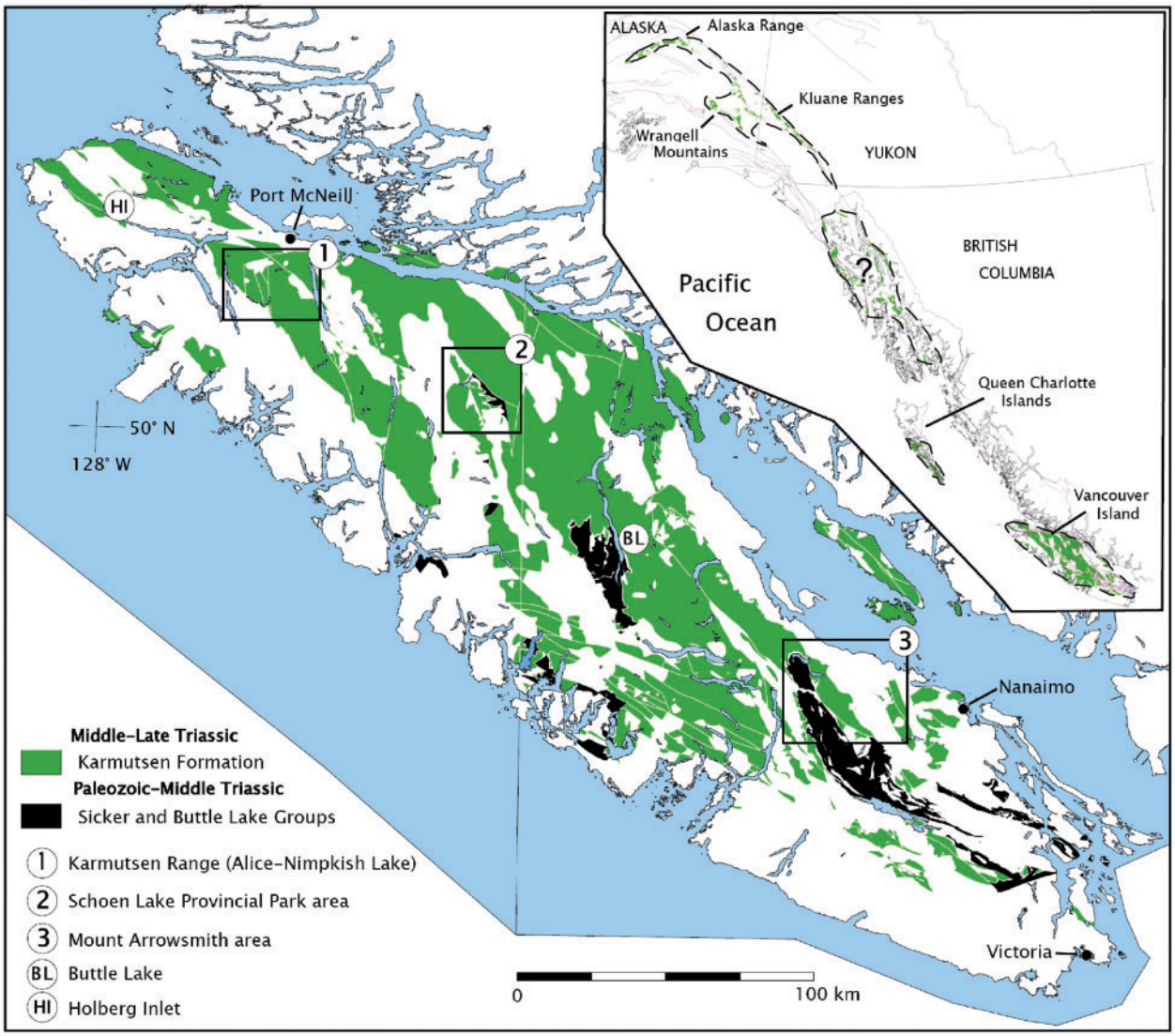

Fig. 1. Simplified map of Vancouver Island showing the distribution of the Karmutsen Formation and underlying Paleozoic formations (after Massey *et al.*, 2005*a*, 2005*b*). Areas in white are mostly younger units. The main areas of field study are indicated with boxes or circles with capital letters (see legend). Ocean is light blue. The inset shows the extent of the Wrangellia flood basalts (green) in British Columbia, Yukon, and Alaska.

and massive submarine flows, a middle unit of mostly pillow breccia and hyaloclastite, and an upper unit of predominantly massive subaerial flows (Carlisle & Suzuki, 1974). The pillow basalts directly overlie Middle Triassic and late Paleozoic marine sedimentary sequences that are intruded by Karmutsen mafic sills. The boundary between pillow breccia–hyaloclastite and massive lava flows represents the transition from a submarine to a subaerial eruptive environment. The uppermost flows of the Karmutsen are intercalated with and overlain by shallow-water limestone and local occurrences of pillowed flows and hyaloclastite deposits occur within the upper subaerial member. The Karmutsen Formation and Wrangellia on Vancouver Island have been the focus of detailed mapping and stratigraphic studies by Carlisle (Carlisle, 1963, 1972; Carlisle & Suzuki, 1974) and Muller (Muller *et al.*, 1974; Muller, 1977). Recent descriptions of the Karmutsen Formation on northern Vancouver Island have been made during regional mapping studies (1:50 000 scale) by Nixon and coworkers (Nixon *et al.*, 2006*b*, 2008; Nixon & Orr, 2007).

Age of the Karmutsen Formation

The age and duration of Karmutsen volcanism are constrained by fossils in the underlying and overlying sedimentary units and by three U–Pb isotopic age

determinations on intrusive rocks that are considered to be related to the Karmutsen volcanics. *Daonella*-bearing shale 100–200 m below the base of the pillow basalts on Schoen Mountain and *Halobia*-rich shale interlayered with flows in the upper part of the Karmutsen indicate eruption of most of the flood basalts between the Middle Ladinian (*c.* 232–235 Ma; Middle Triassic) and latest Carnian or possibly earliest Norian (*c.* 216–227 Ma; Late Triassic; Carlisle & Suzuki, 1974). The only published U–Pb age is based on a single concordant analysis of a multi-grain baddeleyite fraction from a gabbro on southern Vancouver Island that yielded a $^{206}Pb/^{238}U$ age of 227·3 ± 2·6 Ma (Parrish & McNicoll, 1992). Two unpublished $^{206}Pb/^{238}U$ baddeleyite ages, also from a gabbro on southern Vancouver Island, are 226·8 ± 0·5 Ma (five multi-grain fractions) and 228·4 ± 2·5 Ma (two multi-grain fractions; Sluggett, 2003).

VOLCANIC STRATIGRAPHY AND PETROGRAPHY

Fieldwork undertaken on Vancouver Island as part of this study in 2004–2006 explored the volcanic stratigraphy of the Karmutsen flood basalts in three main areas: the Karmutsen Range (between Alice and Nimpkish lakes), the area around Schoen Lake Provincial Park, and at Mount Arrowsmith (Greene *et al.*, 2005, 2006); areas around Holberg Inlet, in northernmost Vancouver Island, and Buttle Lake, in central Vancouver Island, were also investigated (Fig. 1). The character and thickness of the flood basalt sequences vary locally, although the tripartite succession of the Karmutsen Formation appears to be present throughout Vancouver Island. The stratigraphic thicknesses for the pillow, volcaniclastic, and subaerial flow units in the type area around Buttle Lake are estimated to be ~2600 m, 1100 m, and 2900 m, respectively (Surdam, 1967); estimated thicknesses on northern Vancouver Island are >3000 m, 400–1500 m, and >1500 m, respectively (Nixon *et al.*, 2008); in the vicinity of Mount Arrowsmith and nearby areas on southern Vancouver Island, thicknesses are 1100 m, 950 m, and 1200 m, respectively (Yorath *et al.*, 1999; Fig. 1).

Picritic pillow lavas west of the Karmutsen Range on northern Vancouver Island occur in a roughly triangular-shaped area (~30 km across) bounded by Keogh, Maynard and Sara lakes (Figs 2 and 3; Greene *et al.*, 2006; Nixon *et al.*, 2008). Excellent exposures of picritic pillow lavas occur in roadcuts along the north shore of Keogh Lake, the type locality (Greene *et al.*, 2006). The Keogh Lake picrites form pillowed and massive flow units (<15 m thick; Fig. 3) with pillows and tubes of varied dimensions (typically <1 m wide). Numerous thermal contraction features in the pillows are filled with quartz–carbonate, such as drain-back ledges and tortoise-shell jointing (Greene *et al.*, 2006). The picritic pillow basalts are not readily distinguishable in the field from basalt, except by their density, non-magnetic character and comparatively minor amounts of interpillow quartz–carbonate. Fieldwork and mapping indicates that the picrites occur near the transition between the uppermost pillow lavas and the lowermost part of the volcaniclastic unit (Nixon *et al.*, 2008).

In and around Schoen Lake Provincial Park where the base of the Karmutsen Formation is exposed is a sediment–sill complex consisting of Middle Triassic and Pennsylvanian to Permian limestones and fine-grained siliciclastic sedimentary rocks intruded by mafic sills and overlain by pillow basalt (Figs 2 and 4; Carlisle, 1972). The sediment–sill complex is ~600–900 m thick, which includes 150–200 m of pre-intrusive sedimentary rocks (Carlisle, 1972). The Triassic sedimentary rocks range from thinly bedded siliceous and calcareous shales to banded cherts and finely laminated, *Daonella*-bearing shales (Carlisle, 1972). Basal sills and pre-Karmutsen sediments are also exposed around Buttle Lake (Fig. 1).

Exposures with considerable vertical relief around Mount Arrowsmith (see Electronic Appendix 1; available for downloading at http//petrology.oxfordjournals.org/) and Buttle Lake preserve thick successions of submarine pillow basalts and pillow breccias with rare intercalations of sediment, and subaerial flows. Massive submarine flows in the pillow unit are locally recognizable by their irregular, hackly columnar jointing. The massive subaerial flows form monotonous sequences marked mainly by amygdaloidal horizons; brecciated flow tops are rarely observed. A locality with well-preserved pahoehoe flow features is well exposed north of Holberg Inlet (Fig. 3; Nixon & Orr, 2007; Nixon *et al.*, 2008). There is no evidence of significant detrital material from a continental source in the sediments associated with the flood basalts anywhere on Vancouver Island. The uppermost Karmutsen flows are interbedded with thin (commonly 0–4 m thick) lenses of limestone, and rarely siliciclastic sedimentary rocks (Nixon *et al.*, 2006*b*). Plagioclase-phyric lavas characterize the upper part of the subaerial sequence and locally include distinctive plagioclase-megacrystic (1–2 cm crystals), trachytoid-textured flows (Nixon *et al.*, 2006*b*).

A total of 129 samples were collected from the Karmutsen Formation on Vancouver Island, from which 63 samples were selected for geochemical analysis based on the relative degree of alteration and geographical distribution of the samples. Fifty-six of these samples were divided into four main groups based on petrography (Table 1) and geochemistry: tholeiitic basalt, picrite, high-MgO basalt, and coarse-grained mafic rocks. In addition, two outlying samples and a mineralized sill are distinguished in Table 1. The tholeiitic basalts are dominantly glomeroporphyritic, and less commonly aphanitic, with an intersertal to intergranular groundmass (Table 1).

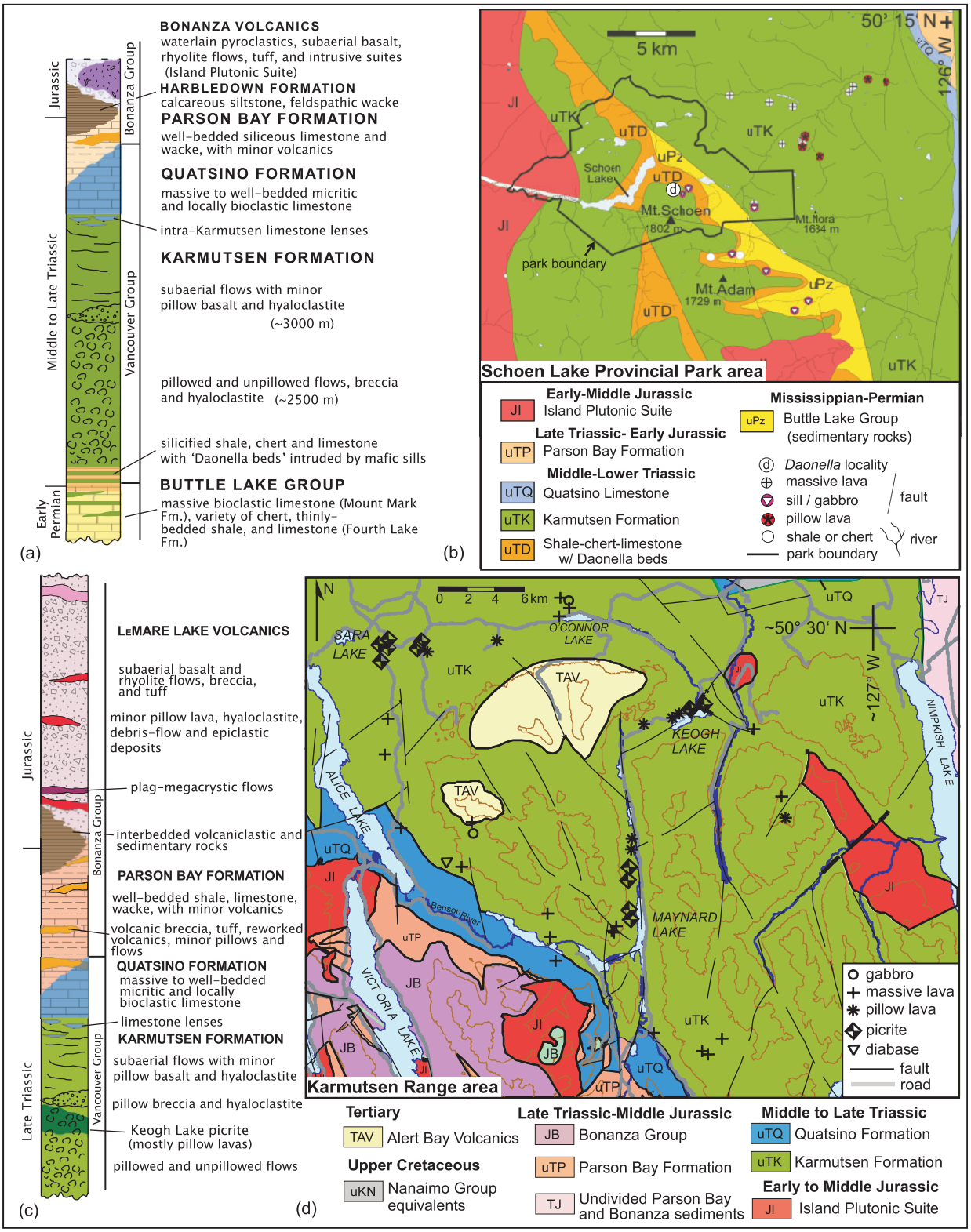

Fig. 2. Geological map and stratigraphy of the Schoen Lake Provincial Park and Karmutsen Range areas (locations shown in Fig. 1, northern Vancouver Island). (a) Stratigraphic column depicts units exposed in the Schoen Lake area, derived from Carlisle (1972) and fieldwork. (b) Generalized geology for the Schoen Lake area with sample locations. Map derived from Massey *et al.* (2005*a*). The exposures in the Schoen Lake area are the lower volcanic stratigraphy and base of the Karmutsen Formation. (c) Stratigraphic column for geology in the Alice–Nimpkish Lake area, derived from Nixon & Orr (2007). (d) Geological map from mapping of Nixon *et al.* (2006*a*, 2008). Sample sites and lithologies are denoted in the legend. The Keogh Lake picrites are exposed near Keogh, Sara, and Maynard lakes and areas to the east of Maynard Lake (Nixon *et al.*, 2008).

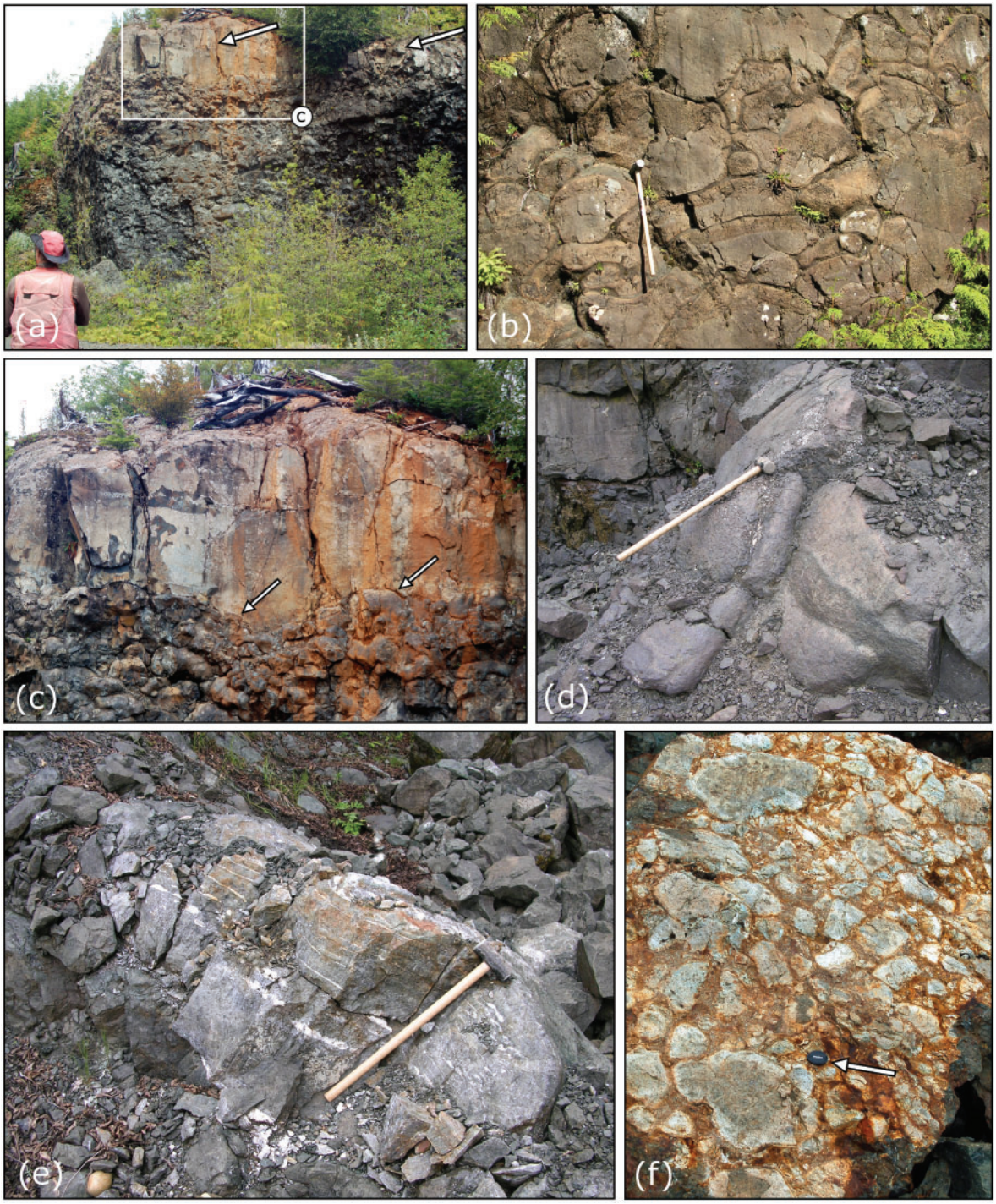

Fig. 3. Photographs of picritic and tholeiitic pillowed and massive basalt flows from the Karmutsen Range (Alice and Nimpkish Lake area) and Holberg Inlet (HI) areas, northern Vancouver Island (locations shown in Fig. 1). (a) Massive submarine flow (marked with arrows) draped over high-MgO pillow basalt of similar composition. (b) Picritic pillow basalts in cross-section near Maynard Lake. (Note vesicular upper margin to pillows.) (c) Close-up photograph of undulating contact of massive submarine flow draped over high-MgO pillow basalt (marked with arrows) from photograph (a) (area of photograph indicated with a white box). (d) Photograph of margin of pahoehoe lobe (sledgehammer for scale). (e) Cross-section of a large picritic pillow lobe with infilling of quartz–carbonate in cooling–contraction cracks (sledgehammer for scale). (f) High-MgO pillow breccia stratigraphically between submarine and subaerial flows (arrow points to lens cap, ~7 cm diameter, for scale).

Fig. 4. Photographs showing field relations from the Schoen Lake Provincial Park area, northern Vancouver Island. (a) Sediment–sill complex at the base of the Karmutsen Formation on the north side of Mt. Schoen ~100 m below the *Daonella* locality (see Fig. 2 for location). (b) Interbedded mafic sills and deformed, finely banded chert and shale with calcareous horizons, from location between Mt. Adam and Mt. Schoen.

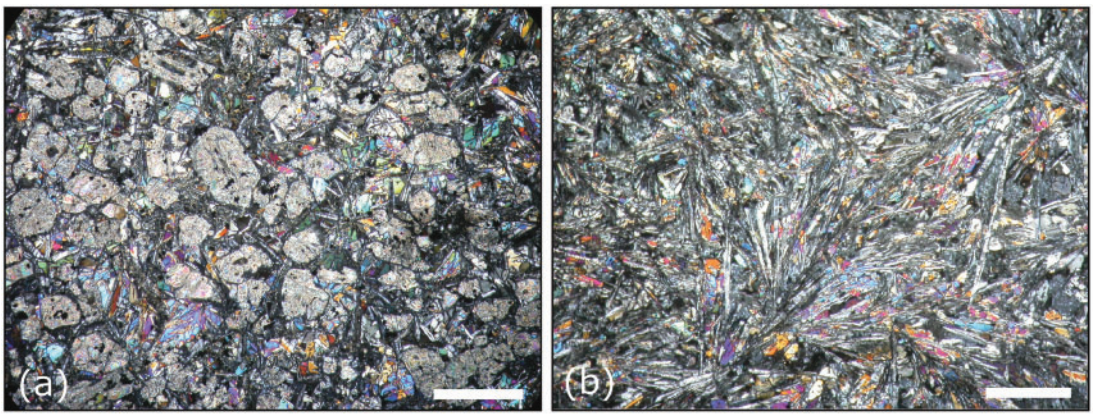

Fig. 5. Photomicrographs of picritic pillow basalts, Karmutsen Formation, northern Vancouver Island. Scale bars represent 1 mm. (a) Picrite with abundant euhedral olivine pseudomorphs from Keogh Lake type locality (Fig. 2) in cross-polarized light (XPL) (sample 4722A4; 19–19·8 wt % MgO, four analyses). Samples contain dense clusters (24–42 vol. %) of olivine pseudomorphs (<2 mm) in a groundmass of curved and branching sheaves of acicular plagioclase and intergrown with clinopyroxene and altered glass. In many cases, plagioclase nucleated on the edges of the olivine phenocrysts. (b) Sheaves of intergrown plagioclase and clinopyroxene in aphyric picrite pillow lava from west of Maynard Lake (Fig. 2) in XPL (sample 4723A2; 10·8 wt % MgO).

Plagioclase forms most of the phenocrysts and glomerocrysts and the groundmass is fine-grained comprising plagioclase microlites, clinopyroxene granules, small grains of Fe–Ti oxide, devitrified glass, and secondary minerals; there is no fresh glass preserved. The picritic and high-MgO basaltic lavas are characterized by spherulitic plagioclase and clinopyroxene with abundant euhedral olivine phenocrysts (Fig. 5; Table 1). Olivine is completely replaced

Table 1: Summary of petrographic characteristics and phenocryst proportions of Karmutsen basalts on Vancouver Island, B.C.

Sample	Area	Flow	Group	Texture	vol.% Ol	Plag	Cpx	Ox	Alteration	Notes
4718A1	MA	PIL	THOL	intersertal		20	5		3	few plag glcr <2 mm, cpx <1 mm
4718A2	MA	PIL	THOL	intersertal, glomero		15			1	plag glcr <2 mm, very fresh
4718A5	MA	FLO	THOL	intersertal, glomero		10			2	mottled, few plag glcr <4 mm
4718A6	MA	BRE	THOL	porphyritic		20			2	plag 5–6 mm, sericite alteration
4718A7	MA	PIL	THOL	glomero		10			3	plag glcr <3 mm
4719A2	MA	PIL	THOL	porphyritic, intersertal		5			3	plag glcr <2 mm
4719A3	MA	PIL	THOL	glomero		10			2	plag glcr <3 mm
4720A2	SL	BRE	THOL	glomero		5			3	plag glcr <2 mm
4720A3	SL	FLO	THOL	glomero		3			3	plag glcr <3 mm
4720A4	SL	FLO	THOL	glomero		5			1	plag glcr <5 mm, slightly c.g., very fresh
4720A5	SL	PIL	THOL	seriate		20			3	plag glcr <2 mm, plag needles and laths
4720A8	SL	FLO	THOL	glomero		20			2	plag glcr <2 mm, plag needles and laths
4720A9	SL	FLO	THOL	glomero		10			2	plag glcr <1·5 mm
4721A1	SL	PIL	THOL	glomero		15			3	plag glcr <1·5 mm, plag needles aligned
4721A2	SL	FLO	THOL	glomero		10			1	plag glcr <3 mm, very fresh
4721A3	SL	FLO	THOL	glomero		20			3	plag glcr <2 mm, plag needles
4721A4	SL	FLO	THOL	glomero, ophimottled		20	5		1	plag glcr <1·5 mm, cpx <1 mm (oik), very fresh
4721A5	SL	FLO	THOL	glomero, ophimottled		5	15		3	plag glcr <1·5 mm, cpx <1 mm (oik)
4722A2	KR	FLO	THOL	intergranular, intersertal		1			1	few plag phenos <2 mm
4723A10	KR	FLO	THOL	intergranular		5	3	10	3	few plag glcr <1 mm, ox 0·5–1 mm
4724A5	SL	FLO	THOL	porphyritic		25			3	plag 7–8 mm
5614A10	KR	FLO	THOL	intergranular, intersertal		2		5	3	ox <0·5 mm
5614A11	KR	FLO	THOL	intergranular, intersertal		5		7	3	ox 0·5–1 mm
5614A13	KR	FLO	THOL	intergranular, porphyritic		5		5	3	ox 0·5–1 mm
5615A1	KR	PIL	THOL	aphyric, intersertal		1			2	f.g., no phenos
5615A8	KR	PIL	THOL	intergranular				3	1	f.g., abundant small ox, very fresh
5615A10	KR	PIL	THOL	intergranular		3			3	2 plag glcr <4 mm
5616A2	KR	FLO	THOL	intergranular, intersertal		5		7	3	ox 0·2–0·5 mm
5618A1	QI	FLO	THOL	intergranular		3	2	10	3	ox 0·5–2 mm, c.g., plag laths >2 mm
4720A6	SL	FLO	CG	subophitic			15		1	plag glcr <3 mm, cpx <3 mm
4720A7	SL	FLO	CG	subophitic			25		1	plag chad <1·5 mm, cpx oik <2 mm, very fresh
4720A10	SL	SIL	CG	subophitic, intrafasciculate				5	3	plag chad <2 mm, cpx oik <3 mm, ox <1 mm, c.g.
4724A3	SL	FLO	CG	ophimottled, subophitic		5	30	5	3	plag glcr 4–5 mm, cpx oik <2 mm, ox <1 mm
5614A14	KR	SIL	CG	intergranular			10	5	3	plag <1 mm, cpx <2 mm
5614A15	KR	SIL	CG	subophitic			25	3	1	plag <1 mm, cpx oik <3 mm, ox <0·2 mm
5615A5	KR	GAB	CG	intergranular, plag-phyric		30		5	3	ox <0·5 mm, plag laths <4 mm
5615A6	KR	GAB	CG	intergranular, plag-phyric		15		10	3	plag <3 mm, ox 0·5–1·5 mm
5616A3	KR	GAB	CG	subophitic			25	5	1	plag laths <1 mm, cpx oik <2 mm, ox 0·5–1 mm
5617A1	SL	SIL	CG	intergranular, intergrowths			30		3	plag <3 mm, cpx <5 mm, cpx–plag intergrowths
5617A5	SL	SIL	CG	intergranular, intersertal		1			1	plag <1 mm, f.g., mottled
93G171	KR	PIL	PIC	subophitic	23					ol <2·3 mm, cpx <1·5 mm, partially enc plag
4722A4	KR	PIL	PIC	cumulus, intergranular	35		10		3	ol <1·5 mm, cpx <2 mm enc plag
4723A3	KR	PIL	PIC	spherulitic	31				3	ol <1 mm, swtl plag <1·5 mm
4723A4	KR	PIL	PIC	intergranular, intersertal	0				3	swtl plag <1 mm, no ol phenos
4723A13	KR	PIL	PIC	spherulitic	24				3	swtl plag <1 mm

(continued)

Table 1: Continued

Sample	Area	Flow	Group	Texture	vol.% Ol	Plag	Cpx	Ox	Alteration	Notes
5614A1	KR	PIL	PIC	spherulitic	24				1	ol <1·5 mm, swtl plag <1 mm
5615A7	KR	PIL	PIC	cumulus, intergranular	42		10		1	ol <1·5 mm, cpx <1·5 mm enc plag
5615A12	KR	PIL	PIC	spherulitic	13				1	ol <2 mm, swtl plag <1 mm
5616A1	KR	PIL	PIC	intergranular, intersertal	25				1	ol <2 mm
4723A2	KR	PIL	HI-MG	spherulitic	0				3	swtl plag <2 mm, no ol phenos
5614A3	KR	PIL	HI-MG	spherulitic, intrafasciculate	12				1	ol <1·5 mm, swtl plag <2 mm
5614A5	KR	BRE	HI-MG	porphyritic, ophimottled	13				2	ol <2 mm, cpx <2 mm enc plag
5616A7	KR	PIL	HI-MG	intersertal	2				2	ol <2 mm, plag needles <1 mm
4722A5	KR	FLO	OUTLIER	intersertal					3	mottled, very f.g., v. small pl needles
5615A11	KR	PIL	OUTLIER	intersertal					3	mottled, very f.g., v. small pl needles
5617A4	SL	SIL	MIN	intersertal				5	3	f.g.

Sample number: last digit of year, month, day, initial, sample station (except 93G171). MA, Mount Arrowsmith; SL, Schoen Lake; KR, Karmutsen Range. PIL, pillow; BRE, breccia; FLO, flow; SIL, sill; GAB, gabbro; THOL, tholeiitic basalt; PIC, picrite; HI-MG, high-MgO basalt; CG,coarse-grained; MIN, mineralized sill. glomero, glomeroporphyritic. Olivine modes for picrites are based on area calculations from scans (see 'Olivine accumulation in high-MgO and picritic lavas' section and Fig. 11). Visual alteration index is based primarily on degree of plagioclase alteration and presence of secondary minerals (1, least altered; 3, most altered). Plagioclase phenocrysts are commonly altered to albite, pumpellyite, and chlorite; olivine is altered to talc, tremolite, and clinochlore (determined using the Rietveld method of X-ray powder diffraction); clinopyroxene is unaltered; Fe–Ti oxide is commonly replaced by sphene. glcr, glomerocrysts; f.g., fine-grained; c.g., coarse-grained, oik, oikocryst; chad, chadacryst; enc, enclosing; swtl, swallow-tail; ol, olivine pseudomorphs; plag, plagioclase; cpx, clinopyroxene; ox, oxides (includes ilmenite + titanomagnetite).

by an assemblage of talc–tremolite–serpentine–opaque oxides; there is no fresh olivine present in the Karmutsen lavas on Vancouver Island. Plagioclase and clinopyroxene phenocrysts are absent in the high-MgO lavas. The coarse-grained mafic rocks are characterized by sub-ophitic textures with an average grain size typically >1 mm, and are generally not glomeroporphyritic; these rocks are mainly from the interiors of massive flows, although some may represent sills.

Sample preparation and analytical methods for major- and trace-element and Sr–Nd–Hf–Pb isotopic compositions of the Karmutsen volcanic rocks are given in the Appendix.

WHOLE-ROCK CHEMISTRY

Major- and trace-element compositions

The most abundant type of volcanic rock in the Karmutsen Formation is tholeiitic basalt with a restricted range of major- and trace-element compositions. The tholeiitic basalts have similar compositions to the coarse-grained mafic rocks, and both groups are distinct from the picrites and high-MgO basalts [Fig. 6; picrites >12 wt % MgO (LeBas, 2000); high-MgO basalts 8–12 wt % MgO]. The tholeiitic basalts have lower MgO (5·7–7·7 wt % MgO) and higher TiO_2 (1·4–2·2 wt % TiO_2) than the picrites (13·0–19·8 wt % MgO, 0·5–0·7 wt % TiO_2) and high-MgO basalts (9·1–11·6 wt % MgO, 0·5–0·8 wt % TiO_2; Fig. 6; Table 2). Almost all compositions plot within the tholeiitic field in a total alkalis vs silica plot, although there has been substantial K loss in most samples from the Karmutsen Formation (see below), and the tholeiitic basalts generally have higher SiO_2, $Na_2O + K_2O$, CaO, and FeO_T (total iron expressed as FeO) than the picrites. The tholeiitic basalts also have noticeably lower loss on ignition (LOI; mean $1·7 \pm 1·3$ wt %) than the picrites (mean $5·4 \pm 0·8$ wt %) and high-MgO basalts (mean $3·8 \pm 1·5$ wt %) (Fig. 6) reflecting the presence of abundant altered olivine phenocrysts in the latter groups. Ni concentrations are significantly higher for the picrites (339–755 ppm) and high-MgO basalts (122–551 ppm) than the tholeiitic basalts (58–125 ppm, except for one anomalous sample) and coarse-grained rocks (70–213 ppm) (Fig. 6; Table 2). An anomalous tholeiitic pillowed flow (two samples; outlier in Tables 1 and 2), from near the picrite type locality at Keogh Lake, and a mineralized sill (disseminated sulfide), from the basal sediment–sill complex at Schoen Lake, are distinguished by higher TiO_2 and FeO_T than the main group of tholeiitic basalts. The tholeiitic basalts are similar in major-element composition to previously published results for samples from the Karmutsen Formation; however, the Keogh Lake picrites, which encompass the

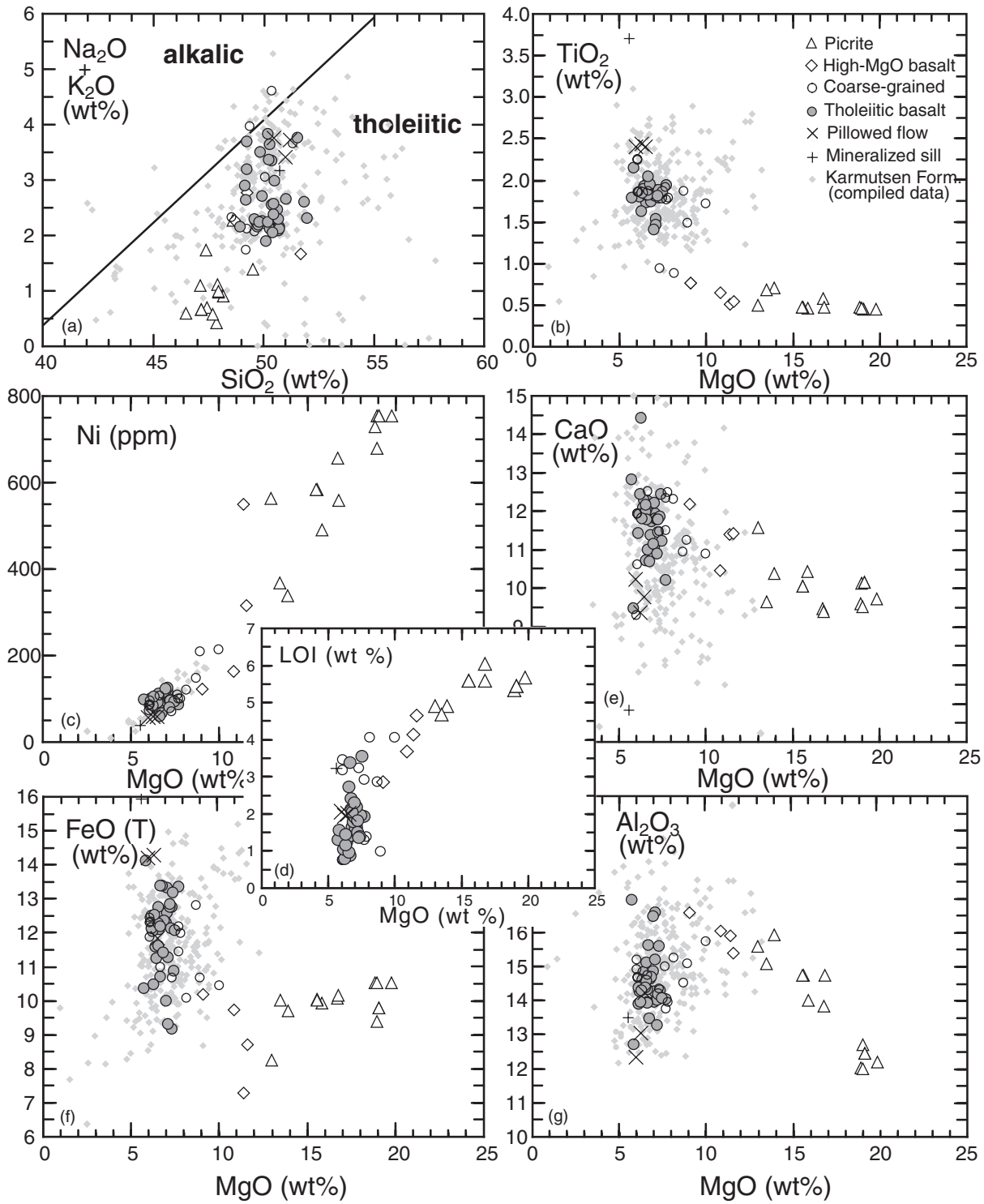

Fig. 6. Whole-rock major-element, Ni, and LOI variation diagrams for the Karmutsen Formation. New samples from this study (Table 2) are shown by symbols with black outlines (see legend). Previously published analyses are shown by small gray symbols without black outlines. The boundary of the alkaline and tholeiitic fields is that of MacDonald & Katsura (1964). Total iron expressed as FeO; LOI, loss on ignition; oxides are plotted on an anhydrous, normalized basis. References for the 322 compiled analyses for the Karmutsen Formation are Surdam (1967), Kuniyoshi (1972), Muller *et al.* (1974), Barker *et al.* (1989), Lassiter *et al.* (1995), Massey (1995*a*, 1995*b*), Yorath *et al.* (1999) and G. Nixon (unpublished data). It should be noted that the compiled dataset has not been filtered; many of the samples with high SiO_2 (>52 wt %) are probably not Karmutsen flood basalts, but younger Bonanza basalts and andesites. Three pillowed flow samples and a mineralized sill are distinguished separately because of their anomalous chemistry. Coarse-grained samples are indicated separately. Three tholeiitic basalt samples (4724A5, 4718A5, 4718A6) with >16 wt % Al_2O_3 and >270 ppm Sr contain 10–25 modal% of large plagioclase phenocrysts (7–8 mm) or glomerocrysts (>4 mm).

Table 2: Major element (wt % oxide) and trace element (ppm) abundances in whole-rock samples of Karmutsen basalts, Vancouver Island, B.C.

Sample:	4718A1	4718A2(1)	4718A2(2)	4718A5	4718A6	4718A7	4719A2	4719A3	4720A2	4720A3
Group:	THOL	THOL	THOL	THOL	THOL	THOL	THOL	THOL	THOL	THOL
Area:	MA	MA	MA	MA	MA	MA	MA	MA	SL	SL
Flow:	Pillow	Pillow	Pillow	Flow	Breccia	Pillow	Pillow	Pillow	Breccia	Flow
UTM EW:	5455062	5455150	5455150	5455459	5455518	5455280	5454625	5454625	5567712	5567305
UTM NS:	384113	384260	384260	383424	383237	382261	381761	381761	708686	707890
Unnormalized major element oxides (wt %)										
SiO_2	47·93	48·65	49·07	48·41	48·69	48·44	49·68	49·08	49·24	48·47
TiO_2	1·65	1·86	1·84	1·40	1·36	1·49	1·71	1·68	1·58	1·72
Al_2O_3	14·41	14·30	14·15	15·89	15·92	14·74	14·93	14·06	13·54	13·52
Fe_2O_3*	12·29	12·07	12·48	9·90	10·74	12·13	9·75	12·21	11·30	11·61
MnO	0·17	0·18	0·18	0·16	0·16	0·17	0·19	0·18	0·21	0·19
MgO	6·25	6·21	6·16	6·81	6·74	6·89	6·98	6·55	6·09	7·12
CaO	10·22	11·85	11·70	11·31	10·76	11·56	10·96	10·94	14·00	11·94
Na_2O	3·22	2·28	2·25	2·51	2·89	2·39	2·23	2·24	2·12	2·18
K_2O	0·24	0·18	0·14	0·35	0·34	0·24	0·27	0·31	0·10	0·29
P_2O_5	0·15	0·14	0·15	0·10	0·12	0·12	0·08	0·13	0·12	0·12
LOI	2·72	1·38	1·22	2·17	2·28	1·64	1·97	1·63	1·15	1·95
Total	99·24	99·09	99·33	99·01	99·98	99·81	98·75	99·00	99·45	99·11
Trace elements (ppm)										
La	7·88	9·03	8·72	6·50	6·58	6·10	7·17	7·02	7·20	7·88
Ce	19·0	22·2	21·6	15·5	16·2	15·4	18·0	17·7	17·3	19·0
Pr	2·71	3·10	3·02	2·15	2·20	2·23	2·62	2·52	2·42	2·72
Nd	13·0	15·2	14·5	10·7	11·2	11·4	13·2	12·5	12·2	13·5
Sm	3·57	4·11	4·05	3·03	3·13	3·42	3·67	3·66	3·43	3·85
Eu	1·40	1·57	1·48	1·18	1·20	1·25	1·47	1·39	1·33	1·47
Gd	4·39	4·77	4·87	3·59	3·64	3·90	4·32	4·24	4·12	4·48
Tb	0·76	0·82	0·82	0·63	0·64	0·68	0·76	0·74	0·71	0·78
Dy	4·55	5·02	4·79	3·80	3·87	4·12	4·68	4·41	4·28	4·78
Ho	0·90	0·99	0·96	0·77	0·78	0·84	0·94	0·89	0·87	0·95
Er	2·57	2·79	2·72	2·20	2·27	2·34	2·66	2·45	2·48	2·69
Tm	0·36	0·40	0·39	0·32	0·32	0·33	0·37	0·35	0·34	0·38
Yb	2·15	2·39	2·32	1·90	1·96	2·00	2·23	2·11	2·05	2·33
Lu	0·31	0·33	0·32	0·27	0·27	0·28	0·30	0·30	0·29	0·33
Sc	40·7	41·3	40·4	38·9	38·3	40·2	42·8	42·8	41·1	46·2
V	328	351	353	285	279	317	341	341	325	344
Cr	93	146	125	290	297	252	130	131	151	168
Co	48·7	49·9	48·9	46·1	45·4	51·4	53·1	53·4	50·5	56·2
Ni	87	90	88	125	122	115	94	103	83	93
Cu	177	201	198	167	158	159	180	168	167	184
Zn	83	91	91	77	73	82	86	87	79	88
Ga	19	19	20	17	19	18	16	18	19	17
Ge	1·6	1·5	1·4	1·1	1·5	1·5	0·7	1·5	1·9	1·1
Rb	4	2	2	6	6	4	5	5		6
Sr	418	231	228	282	332	263	281	286	192	214
Y	25	28	28	22	22	24	26	26	25	27
Zr	86	97	94	72	71	77	86	83	83	90
Nb	8·4	10·1	10·0	7·0	6·8	6·5	7·4	7·3	7·9	8·6
Cs	0·7	0·3	0·2	0·5	0·5	0·2	0·2	0·2		0·2
Ba	173	50	49	71	98	62	143	133	28	81
Hf	2·6	2·8	2·8	2·0	2·2	2·1	2·6	2·5	2·4	2·6
Ta	0·59	0·68	0·65	0·45	0·46	0·41	0·53	0·49	0·51	0·60
Pb	4	7	7	10	4	6	7	11	7	9
Th	0·65	0·74	0·72	0·52	0·53	0·54	0·61	0·61	0·57	0·64
U	0·20	0·23	0·24	0·17	0·16	0·17	0·22	0·19	0·18	0·20

(continued)

Table 2: Continued

Sample:	4720A4	4720A5	4720A8	4720A9	4721A1	4721A2	4721A3	4721A4	4721A5	4722A2(1)[1]
Group:	THOL	THOL	THOL	THOL	THOL	THOL	THOL	THOL	THOL	THOL
Area:	SL	SL	SL	SL	SL	SL	SL	SL	SL	KR
Flow:	Flow	Pillow	Flow	Flow	Pillow	Flow	Flow	Flow	Flow	Flow
UTM EW:	5566984	5563304	5566800	5564002	5563843	5563936	5564229	5564285	5564343	5590769
UTM NS:	707626	705978	700781	703739	704932	704941	704928	704896	705008	634318
Unnormalized major element oxides (wt %)										
SiO_2	49·16	48·88	48·02	48·06	48·17	49·56	48·17	49·49	49·37	48·33
TiO_2	1·78	1·78	1·77	1·77	1·89	1·77	1·77	1·79	1·81	1·80
Al_2O_3	14·00	13·84	14·34	14·11	14·96	13·92	14·16	13·98	13·98	13·59
$Fe_2O_3^*$	13·30	13·46	13·18	13·73	11·40	13·07	13·24	13·13	13·53	13·75
MnO	0·19	0·18	0·20	0·19	0·18	0·17	0·18	0·18	0·20	0·19
MgO	6·39	6·12	6·73	6·35	6·39	6·06	6·61	6·46	5·98	6·97
CaO	11·85	11·43	11·37	11·61	11·75	12·15	11·30	11·76	11·59	11·42
Na_2O	1·86	2·16	1·97	2·08	1·93	2·01	2·03	1·92	1·92	2·03
K_2O	0·14	0·14	0·11	0·11	0·10	0·09	0·15	0·12	0·15	0·14
P_2O_5	0·15	0·16	0·15	0·16	0·13	0·16	0·14	0·14	0·15	0·15
LOI	0·93	1·42	1·91	1·37	2·11	0·76	1·78	0·87	1·04	1·48
Total	99·75	99·56	99·73	99·52	99·01	99·73	99·53	99·85	99·71	99·84
Trace elements (ppm)										
La	8·44	8·07	6·86	7·06	7·31	7·86	7·42	7·21	7·62	6·95
Ce	20·5	19·5	17·5	17·3	18·9	19·2	18·3	17·9	18·8	17·8
Pr	2·88	2·73	2·54	2·46	2·78	2·70	2·66	2·57	2·73	2·53
Nd	14·3	13·5	12·6	12·3	13·5	13·5	13·3	13·0	13·9	12·9
Sm	4·07	3·87	3·72	3·51	4·06	3·84	3·84	3·81	3·91	3·72
Eu	1·49	1·45	1·37	1·36	1·47	1·46	1·40	1·38	1·47	1·41
Gd	4·70	4·74	4·40	4·19	4·72	4·47	4·59	4·28	4·73	4·42
Tb	0·81	0·83	0·77	0·75	0·81	0·79	0·79	0·77	0·83	0·77
Dy	4·90	4·92	4·86	4·62	4·99	4·75	4·88	4·77	5·12	4·61
Ho	0·99	0·98	0·98	0·93	1·03	0·96	0·98	0·97	1·04	0·94
Er	2·81	2·79	2·78	2·65	2·96	2·72	2·82	2·80	2·99	2·65
Tm	0·39	0·40	0·40	0·37	0·41	0·38	0·39	0·40	0·42	0·38
Yb	2·31	2·46	2·51	2·27	2·50	2·35	2·42	2·40	2·55	2·32
Lu	0·33	0·35	0·35	0·33	0·36	0·32	0·35	0·34	0·35	0·32
Sc	42·9	44·5	42·0	44·0	44·4	42·1	42·3	42·2	39·7	39·2
V	349	362	362	362	378	351	364	364	367	365
Cr	122	156	155	166	158	118	164	151	122	143
Co	53·7	54·8	54·5	55·5	54·8	51·6	54·9	53·3	46·5	50·0
Ni	92	105	116	112	106	91	115	108	90	107
Cu	202	185	218	187	208	195	206	211	210	189
Zn	92	93	109	90	86	90	87	92	92	104
Ga	20	19	19	18	18	19	19	19	19	19
Ge	1·6	1·6	1·8	1·4	1·3	1·7	1·3	1·7	1·6	1·4
Rb	2	1		1	2	1	1	1	1	2
Sr	179	188	174	196	174	187	162	160	171	190
Y	27	28	28	28	30	26	28	29	29	27
Zr	97	92	95	88	97	97	95	95	96	96
Nb	9·1	8·2	8·3	7·8	8·5	9·0	8·5	8·6	8·5	8·3
Cs	0·2	0·1	0·2	0·1	0·6	0·2	0·4	0·3	0·2	0·2
Ba	34	38	33	35	36	39	34	28	34	34
Hf	2·7	2·6	2·7	2·6	2·9	2·8	2·8	2·7	2·9	2·8
Ta	0·60	0·56	0·55	0·53	0·58	0·60	0·57	0·55	0·59	0·55
Pb	7	8	8	8	14	8	9	9	5	11
Th	0·68	0·61	0·62	0·61	0·68	0·69	0·62	0·62	0·67	0·66
U	0·20	0·19	0·19	0·18	0·22	0·21	0·20	0·19	0·20	0·19

(continued)

Table 2: Continued

Sample:	4722A2(2)[1]	4722A2(3)[1]	4722A2(4)[1]	4723A10	4724A5	5614A10	5614A11	5614A13	5615A1	5615A8
Group:	THOL	THOL	THOL	THOL	THOL	THOL	THOL	THOL	THOL	THOL
Area:	KR	KR	KR	KR	SL	KR	KR	KR	KR	KR
Flow:	Flow	Flow	Flow	Flow	Flow	Flow	Flow	Flow	Pillow	Pillow
UTM EW:	5590769	5590769	5590769	5578863	5580653	5595261	5593546	5588018	5599424	5595513
UTM NS:	634318	634318	634318	630940	704736	615253	615098	618867	620187	629434
Unnormalized major element oxides (wt %)										
SiO_2	48·67	47·23	48·16	50·03	48·08	46·69	48·06	47·78	47·61	48·31
TiO_2	1·82	1·78	1·78	2·08	1·73	1·76	1·74	1·86	1·87	1·75
Al_2O_3	13·74	13·77	13·62	12·31	16·39	13·32	13·35	12·91	13·55	13·45
Fe_2O_3*	13·05	14·13	13·76	15·21	11·13	12·72	12·96	14·23	14·34	13·48
MnO	0·19	0·19	0·19	0·22	0·20	0·17	0·19	0·21	0·19	0·20
MgO	7·02	7·09	7·09	5·66	5·54	7·09	6·38	6·47	7·42	6·78
CaO	11·42	11·43	11·48	9·19	12·38	10·62	10·51	10·24	9·86	11·77
Na_2O	2·05	2·02	2·08	2·94	2·01	3·49	3·23	2·91	2·87	1·80
K_2O	0·13	0·06	0·14	0·70	0·10	0·01	0·44	0·44	0·21	0·03
P_2O_5	0·14	0·14	0·12	0·18	0·15	0·14	0·13	0·15	0·15	0·14
LOI	1·34	1·38	1·37	1·55	1·29	3·53	2·39	2·02	1·92	1·74
Total	99·56	99·22	99·79	100·07	99·01	99·43	99·37	99·21	100	99·43
Trace eements (ppm)										
La	7·34	7·65	6·95	8·93	7·98	8·04	7·23	8·51	8·17	7·32
Ce	18·5	19·3	17·8	21·5	19·4	19·7	18·0	20·9	20·2	18·4
Pr	2·64	2·94	2·67	3·10	2·72	2·96	2·68	3·08	3·01	2·69
Nd	12·7	13·6	13·3	15·5	13·3	13·7	12·3	14·7	14·3	12·9
Sm	3·66	4·05	3·77	4·20	3·69	3·88	3·6	4·2	4·12	3·78
Eu	1·42	1·55	1·42	1·62	1·42	1·44	1·39	1·59	1·58	1·47
Gd	4·62	4·76	4·59	5·21	4·58	4·47	4·24	4·79	4·88	4·4
Tb	0·77	0·83	0·80	0·90	0·75	0·79	0·77	0·87	0·85	0·79
Dy	4·60	4·92	4·77	5·40	4·53	4·59	4·57	5·12	5·01	4·65
Ho	0·94	0·92	0·95	1·11	0·89	0·85	0·89	0·98	0·94	0·89
Er	2·70	2·64	2·69	3·23	2·54	2·47	2·53	2·83	2·7	2·58
Tm	0·38	0·389	0·37	0·45	0·36	0·37	0·36	0·413	0·404	0·379
Yb	2·27	2·41	2·28	2·71	2·26	2·27	2·26	2·54	2·51	2·34
Lu	0·34	0·349	0·34	0·39	0·32	0·325	0·329	0·375	0·365	0·339
Sc	29·2	41·6	41·5	38·3	34·4	43·8	43·8	42·4	44·5	40·4
V	365	362	362	496	299	354	362	372	380	353
Cr	98	162	165	34·2	207	195	76	71·9	172	173
Co	37·7	55·7	53·5	47·1	43·1	48·9	53·6	51·5	57·4	53
Ni	105	93	93	61	98	93	67	65	86	96
Cu	189	178	174	306	198	134	181	165	182	175
Zn	103	98	94	107	76	80	93	102	84	88
Ga	19	20	17	20	21	20	17	20	19	20
Ge	1·5	1·5	1·2	1·6	1·5	1·4	0·9	1·6	1·3	1·4
Rb	2	2	2	12			9	8	5	2
Sr	193	178	190	299	272	86	381	274	287	194
Y	28	26	27	32	25	26	27	29	29	28
Zr	87	94	102	110	92	90	86	98	98	91
Nb	8·4	8·5	8·5	9·7	8·6	8·1	8·0	9·0	8·6	8·0
Cs	0·2	0·4	0·2	0·4	0·1	0·8	0·4	0·1	0·9	0·6
Ba	34	28	33	152	32	11	80	85	39	39
Hf	2·6	2·8	2·8	3·1	2·7	2·7	2·5	2·9	3·0	2·7
Ta	0·54	0·6	0·57	0·65	0·60	0·6	0·5	0·7	0·6	0·6
Pb	12	91		5		97	97	98	97	91
Th	0·64	0·59	0·68	0·77	0·69	0·75	0·62	0·66	0·64	0·59
U	0·20	0·23	0·15	0·27	0·25	0·3	0·24	0·26	0·27	0·22

(continued)

Table 2: Continued

Sample:	5615A10	5616A2	5618A1	5618A3	5618A4	4720A6	4720A7(1)	4720A7(2)	4720A10	4724A3
Group:	THOL	THOL	THOL	THOL	THOL	CG	CG	CG	CG	CG
Area:	KR	KR	QI	QI	QI	SL	SL	SL	SL	SL
Flow:	Pillow	Flow	Flow	Pillow	Breccia	Flow	Flow	Flow	Sill	Flow
UTM EW:	5595376	5585731	5557892	5552258	5552258	5566161	5566422	5566422	5560585	5581870
UTM NS:	629069	623077	338923	341690	341690	704411	703056	703056	702230	704472
Unnormalized major element oxides (wt %)										
SiO_2	47·29	46·72	48·61	47·90	40·29	48·90	49·60	49·53	47·38	49·08
TiO_2	1·81	1·94	1·75	1·36	2·16	1·80	1·81	1·81	0·83	1·46
Al_2O_3	13·70	13·21	12·82	13·79	16·27	14·21	14·34	14·36	14·42	14·77
$Fe_2O_3^*$	14·23	14·11	13·81	11·62	18·10	11·78	13·37	13·39	10·58	11·60
MnO	0·20	0·24	0·21	0·16	0·28	0·20	0·20	0·20	0·16	0·13
MgO	6·77	6·29	6·96	6·57	9·70	6·40	5·93	5·94	7·69	8·73
CaO	10·65	11·19	10·54	12·08	6·78	12·08	11·69	11·68	11·66	11·02
Na_2O	2·58	2·49	2·76	3·13	0·58	1·82	1·97	1·97	2·77	1·99
K_2O	0·21	0·01	0·50	0·12	0·52	0·31	0·15	0·13	0·12	0·15
P_2O_5	0·14	0·16	0·14	0·10	0·18	0·12	0·16	0·15	0·06	0·12
LOI	1·57	3·38	1·80	3·17	4·77	1·38	0·75	0·75	4·07	0·98
Total	99·14	99·66	99·9	99·99	99·63	99·00	99·97	99·90	99·75	100·02
Trace elements (ppm)										
La	7·34	8·87	7·72	6·57	10·7	7·75	7·84	7·74	2·24	5·57
Ce	18·5	21·0	19·1	15·4	24·3	19·0	19·0	19·3	5·6	14·3
Pr	2·84	3·02	2·85	2·22	3·48	2·71	2·67	2·74	0·85	2·09
Nd	13·2	14·4	13·5	10·5	15·9	13·9	13·3	13·7	4·8	10·4
Sm	3·92	4·16	3·98	2·98	4·53	4·03	3·86	3·89	1·76	2·98
Eu	1·48	1·59	1·47	1·21	2·04	1·43	1·42	1·43	0·75	1·21
Gd	4·65	4·81	4·56	3·56	5·64	4·62	4·73	4·66	2·58	3·85
Tb	0·81	0·86	0·79	0·63	0·99	0·81	0·81	0·82	0·50	0·65
Dy	4·79	5·07	4·71	3·84	5·95	5·01	4·95	4·97	3·38	4·01
Ho	0·91	0·92	0·88	0·75	1·15	1·01	1·01	1·01	0·76	0·81
Er	2·58	2·72	2·56	2·16	3·36	2·89	2·92	2·89	2·31	2·27
Tm	0·38	0·413	0·375	0·331	0·495	0·41	0·42	0·40	0·34	0·33
Yb	2·42	2·62	2·35	2·12	3·11	2·51	2·49	2·44	2·16	1·98
Lu	0·348	0·378	0·342	0·296	0·455	0·36	0·34	0·35	0·31	0·28
Sc	39·8	41·6	42·9	41·8	54·2	43·4	44·2		49·9	35·1
V	363	401	367	313	499	363	366	367	288	287
Cr	166	76	114	194	159	152	154		311	352
Co	52·4	50·8	53	46	62	52·5	52·6		49·5	52·4
Ni	94	58	79	67	68	107	97	85	121	209
Cu	185	210	25	125	109	188	212	210	134	208
Zn	86	85	89	92	75	96	93	94	64	83
Ga	20	22	19	18	24	18	19	19	14	19
Ge	1·3	1·6	1·5	1·5	1·3	1·2	1·6	1·7	1·4	1·6
Rb	9		8	3	10	10	2	2	2	2
Sr	279	67	227	170	220	155	173	174	130	167
Y	28	30	27	21	38	27	29	28	21	23
Zr	96	100	89	67	112	94	94	93	38	73
Nb	8·5	9·2	8·1	6·6	9·8	8·7	8·6	8·7	1·7	6·5
Cs	1·3		0·4		0·6	0·9	0·3	0·3	0·3	0·3
Ba	61	8	103	17	109	39	45	43	68	55
Hf	2·8	2·9	2·7	2	3·3	2·7	2·7	2·8	1·2	2·1
Ta	0·6	0·6	0·6	0·5	0·7	0·57	0·56	0·55	0·09	0·42
Pb	92	96	83	66	65	7	14	6		7
Th	0·61	0·63	0·57	0·45	0·71	0·64	0·61	0·61	0·24	0·43
U	0·24	0·25	0·22	0·22	0·34	0·21	0·19	0·19	0·11	0·16

(continued)

Table 2: Continued

Sample:	5614A14	5614A15	5615A5	5615A6	5616A3	5617A1	5617A5(1)[1]	5617A5(2)[1]	4722A4(1)[1]	4722A4(2)[1]
Group:	CG	CG	CG	CG	CG	CG	CG	CG	PIC	PIC
Area:	KR	KR	KR	KR	KR	SL	SL	SL	KR	KR
Flow:	Sill	Flow	Flow	Sill	Flow	Sill	Sill	Sill	Pillow	Pillow
UTM EW:	5588246	5589935	5601095	5601095	5584647	5560375	5557712	5557712	5595528	5595528
UTM NS:	618183	615917	624103	624103	623236	702240	700905	700905	629490	629490
Unnormalized major element oxides (wt %)										
SiO_2	46·17	46·20	47·76	46·53	46·77	49·10	49·31	47·40	43·85	43·84
TiO_2	1·77	1·61	2·13	2·12	1·81	0·90	1·71	1·71	0·43	0·43
Al_2O_3	13·80	14·77	14·41	14·06	14·23	13·72	13·39	13·33	11·56	11·74
$Fe_2O_3^*$	13·53	10·89	12·50	13·01	12·85	11·34	12·39	12·71	10·11	9·65
MnO	0·14	0·12	0·19	0·18	0·19	0·16	0·17	0·17	0·16	0·16
MgO	8·25	9·37	5·71	5·70	7·28	6·99	7·50	7·46	17·74	17·51
CaO	10·41	10·22	8·81	10·00	10·92	10·96	12·01	11·93	9·43	9·36
Na_2O	2·01	1·55	4·16	3·64	1·86	3·46	1·83	1·80	0·53	0·53
K_2O	0·21	0·08	0·20	0·09	0·16	0·03	0·22	0·17	0·10	0·13
P_2O_5	0·14	0·13	0·18	0·19	0·13	0·08	0·13	0·14	0·04	0·00
LOI	2·87	4·07	3·17	3·45	2·92	3·23	1·28	1·38	5·45	5·33
Total	99·3	99·03	99·2	98·96	99·14	99·97	99·95	98·21	99·39	98·66
Trace elements (ppm)										
La	7·31	6·88	11·6	11·7	7·14	2·84	8·13	7·94	1·06	0·96
Ce	18·7	17·6	28·4	26·9	17·9	6·9	19·7	19·2	2·6	2·5
Pr	2·81	2·68	4·01	3·95	2·72	1·1	2·89	2·85	0·41	0·38
Nd	13·2	12·5	17·7	17·7	12·9	6·1	13·3	13·3	2·6	2·3
Sm	3·89	3·43	4·74	4·76	3·82	2·14	3·83	3·77	0·92	0·84
Eu	1·47	1·34	1·78	1·73	1·47	0·888	1·45	1·43	0·38	0·37
Gd	4·61	4·03	5·49	5·32	4·49	3·05	4·36	4·32	1·40	1·42
Tb	0·81	0·7	0·93	0·93	0·79	0·63	0·75	0·75	0·30	0·30
Dy	4·76	4·11	5·49	5·31	4·66	4·19	4·35	4·25	2·16	2·17
Ho	0·9	0·76	1·02	0·98	0·9	0·86	0·83	0·81	0·49	0·50
Er	2·55	2·18	2·91	2·86	2·6	2·65	2·37	2·31	1·53	1·54
Tm	0·375	0·324	0·441	0·43	0·373	0·415	0·341	0·342	0·24	0·23
Yb	2·35	2	2·75	2·73	2·35	2·66	2·13	2·14	1·58	1·52
Lu	0·336	0·29	0·392	0·391	0·34	0·401	0·304	0·298	0·23	0·23
Sc	39·3	32·3	35·7	38·5	40	54·5	40·8	37·7	38·3	40·1
V	332	271	381	376	349	327	342	338	201	189
Cr	328	400	127	164	317	210	274	255	1710	1830
Co	58·9	56·8	39·4	43·7	52·6	46·8	51·8	47·6	80·3	84·6
Ni	147	213	73	85	110	70	98	97	755	755
Cu	83	111	105	148	164	160	161	160	92	83
Zn	86	72	86	102	87	69	77	76	77	55
Ga	20	19	21	21	20	16	19	19	10	9
Ge	1·3	1·1	1·4	1·4	1·3	1·3	1·1	0·7	1·0	0·7
Rb	3			2	3		7	7	5	4
Sr	283	183	128	170	237	58	255	254	100	97
Y	28	23	32	31	25	27	24	23	16	13
Zr	91	86	116	121	91	45	89	86	16	19
Nb	8·2	7·7	12·7	13·0	8·1	2·1	8·9	8·5	0·7	0·9
Cs	0·1	0·2	0·2		1·2	0·2	0·2	0·2	2·8	2·7
Ba	62	32	36	34	39	12	38	37	19	18
Hf	2·8	2·6	3·4	3·5	2·7	1·4	2·6	2·5	0·5	0·6
Ta	0·5	0·5	0·9	0·9	0·6	0·1	0·6	0·6	0·09	0·03
Pb	94	82	110	118	93	48	85	83	7	4
Th	0·54	0·52	0·92	0·93	0·52	0·28	0·61	0·57	0·10	0·11
U	0·21	0·22	0·34	0·33	0·23	0·16	0·23	0·25	0·05	0·03

(continued)

Table 2: Continued

Sample:	4722A4(3)[1]	4723A3[1]	4723A4[1]	4723A13(1)[1]	4723A13(2)[1]	5614A1[1]	5615A7[1]	5615A12[1]	5616A1[1]	93G171
Group:	PIC	PIC	PIC	PIC	PIC	PIC	PIC	PIC	PIC	PIC
Area:	KR	KR	KR	KR	KR	KR	KR	KR	KR	KR
Flow:	Pillow	Pillow	Pillow	Pillow	Pillow	Pillow	Pillow	Pillow	Pillow	Pillow
UTM EW:	5595528	5588274	5586081	5599233	5599233	5599183	5595569	5586126	5598448	5599395
UTM NS:	629490	626641	626835	616507	616507	616472	629573	626824	616507	616613
Unnormalized major element oxides (wt %)										
SiO_2	42·94	44·41	44·39	44·62	44·71	46·24	44·08	45·35	43·70	47·93
TiO_2	0·42	0·54	0·66	0·44	0·44	0·47	0·45	0·64	0·44	0·46
Al_2O_3	11·26	12·75	14·93	13·71	13·75	14·57	11·68	14·07	13·66	14·02
$Fe_2O_3^*$	10·82	10·33	10·11	10·38	10·37	8·57	10·98	10·40	10·47	9·93
MnO	0·16	0·15	0·14	0·14	0·14	0·15	0·18	0·14	0·16	0·19
MgO	18·28	15·42	13·02	14·47	14·48	12·11	17·94	12·56	15·55	15·84
CaO	8·98	8·73	9·73	9·37	9·36	10·81	9·19	9·00	8·71	10·42
Na_2O	0·54	0·78	1·56	0·86	0·86	1·30	0·37	2·11	0·98	1·02
K_2O	0·02	0·07	0·07	0·06	0·07	0·01	0·11	0·02	0·04	0·11
P_2O_5	0·03	0·05	0·06	0·05	0·05	0·04	0·04	0·06	0·04	0·08
LOI	5·70	5·61	4·91	5·59	5·59	4·91	4·98	4·68	6·05	
Total	99·16	98·83	99·58	99·68	99·81	99·14	100·00	99·02	99·8	100·00
Trace elements (ppm)										
La	1·08	1·80	1·78	1·40	1·36	1·79	1·02	1·73	1·52	1·4
Ce	2·6	4·5	4·5	3·4	3·4	4·3	2·6	4·7	3·6	3·6
Pr	0·43	0·67	0·71	0·52	0·51	0·65	0·41	0·77	0·55	0·56
Nd	2·5	3·8	4·1	3·0	2·9	3·4	2·4	4·4	3·0	2·9
Sm	0·87	1·27	1·48	1·00	1·01	1·11	0·85	1·47	1·02	1·23
Eu	0·405	0·51	0·63	0·46	0·44	0·501	0·361	0·607	0·454	0·47
Gd	1·45	1·86	2·16	1·71	1·69	1·74	1·35	2·13	1·57	2·10
Tb	0·3	0·37	0·42	0·36	0·35	0·37	0·3	0·42	0·34	0·32
Dy	2·11	2·60	2·79	2·54	2·50	2·67	2·12	2·78	2·44	2·38
Ho	0·47	0·59	0·60	0·59	0·56	0·6	0·46	0·59	0·55	0·64
Er	1·54	1·86	1·79	1·89	1·79	1·87	1·46	1·78	1·73	2·11
Tm	0·242	0·29	0·26	0·29	0·28	0·297	0·236	0·267	0·268	0·297
Yb	1·62	1·85	1·67	1·89	1·84	2·01	1·58	1·75	1·77	1·97
Lu	0·244	0·28	0·25	0·29	0·28	0·308	0·245	0·269	0·277	0·282
Sc	36·4	41·0	38·1	43·5		45	39·5	38·3	37·5	
V	194	218	235	219	222	222	222	215	204	140
Cr	1750	1570	725	1370		1370	1850	906	3000	606
Co	80	72·9	60·4	72·2		68·7	89·3	67·2	67·9	
Ni	755	656	339	583	583	564	680	368	559	491
Cu	83	110	106	142	98	104	80	83	77	91
Zn	55	60	63	106	62	53	54	50	53	57
Ga	11	12	13	12	12	11	10	14	12	
Ge	1·2	1·1	1·1	1·2	1·3	0·9	0·9	1·1	1·1	
Rb	6	2	2	2	1		6	2		
Sr	93	64	132	73	73	120	120	189	112	
Y	15	17	18	16	17	18	15	16	16	13
Zr	16	29	36	24	22	22	15	35	22	24
Nb	0·7	1·3	1·1	0·8	0·7	0·7	0·7	1·4	0·9	0·9
Cs	5·8	0·9	0·8	0·7	0·7	0·4	4·5	0·6	0·8	
Ba	27	15	20	13	13	18	24	15	20	20
Hf	0·6	0·9	1·0	0·7	0·7	0·7	0·5	1·1	0·7	0·8
Ta		0·06	0·05	0·04	0·04					0·1
Pb	22	4		8		26	22	34	22	
Th	0·09	0·20	0·10	0·15	0·14	0·15	0·08	0·09	0·14	0·15
U	0·07	0·09	0·05	0·08	0·07	0·11	0·07	0·07	0·1	

(continued)

Table 2: Continued

Sample:	4723A2[1]	5614A3[1]	5614A5[1]	5616A7	4722A5(1)[1]	4722A5(2)[1]	5615A11	5617A4
Group:	HI-MG	HI-MG	HI-MG	HI-MG	OUTLIER	OUTLIER	OUTLIER	MIN SIL
Area:	KR	KR	KR	KR	KR	KR	KR	SL
Flow:	Pillow	Pillow	Breccia	Pillow	Flow	Flow	Pillow	Sill
UTM EW:	5588266	5599183	5599192	5589833	5595029	5595029	5595029	5557712
UTM NS:	626698	616472	614756	626879	627605	627605	627605	700905
Unnormalized major element oxides (wt %)								
SiO_2	46·73	48·43	47·10	46·75	48·95	48·45	49·08	48·06
TiO_2	0·61	0·48	0·51	0·73	2·30	2·33	2·30	3·51
Al_2O_3	15·24	14·90	14·52	15·92	13·61	12·51	11·86	12·79
$Fe_2O_3^*$	10·26	7·59	9·12	10·88	12·56	15·24	15·20	16·78
MnO	0·16	0·13	0·14	0·15	0·19	0·19	0·22	0·16
MgO	10·27	10·66	10·92	8·70	6·18	5·99	5·73	5·25
CaO	9·93	10·68	10·78	11·69	9·33	8·99	9·84	6·48
Na_2O	2·26	1·51	2·10	2·12	3·26	3·30	3·25	2·31
K_2O	0·38	0·06	0·01	0·07	0·30	0·30	0·04	0·69
P_2O_5	0·06	0·04	0·05	0·04	0·13	0·19	0·22	0·35
LOI	3·70	4·13	4·67	2·86	2·00	1·95	2·07	3·22
Total	99·60	98·6	99·89	99·91	98·80	99·45	99·81	99·6
Trace elements (ppm)								
La	1·94	1·71	0·91	1·51	8·77	9·46	6·41	22·3
Ce	5·0	4·0	2·5	3·8	23·0	25·2	17·3	51·5
Pr	0·74	0·59	0·43	0·59	3·37	3·68	2·89	7·19
Nd	4·2	3·2	2·7	3·5	17·2	17·9	15·6	32·7
Sm	1·41	1·09	1·02	1·36	5·20	5·21	5·06	8·86
Eu	0·52	0·483	0·526	0·638	1·74	1·79	1·88	3·33
Gd	2·09	1·71	1·6	2·05	6·39	6·63	6·19	9·84
Tb	0·42	0·37	0·34	0·43	1·11	1·20	1·13	1·64
Dy	2·91	2·66	2·35	2·9	6·59	7·08	6·65	9·58
Ho	0·67	0·59	0·52	0·61	1·34	1·39	1·24	1·78
Er	2·10	1·87	1·67	1·91	3·85	3·94	3·67	5·06
Tm	0·32	0·292	0·27	0·305	0·55	0·57	0·547	0·73
Yb	2·06	1·99	1·8	2·02	3·31	3·48	3·44	4·56
Lu	0·31	0·312	0·267	0·302	0·45	0·51	0·493	0·637
Sc	47·2	48·8	43·7	50·7	38·7	33·1	43·8	44·2
V	261	217	206	270	481	495	520	517
Cr	358	1420	797	346	79·7	59·0	107	64·4
Co	48·8	76·1	68·6	56·7	45·6	40·7	53·4	38·3
Ni	163	551	315	122	59	59	56	39
Cu	111	111	96	111	116	114	208	232
Zn	61	51	48	51	106	103	94	160
Ga	13	12	13	15	17	20	18	27
Ge	1·2	0·8	0·9	1	0·7	1·3	0·7	2
Rb	10				6	6		21
Sr	271	130	141	181	225	229	143	197
Y	20	17	16	19	39	39	39	52
Zr	33	24	19	26	127	126	124	229
Nb	1·5	0·8	0·5	1·1	10·0	10·6	9·9	19·7
Cs	6·5	0·4		0·3	0·3	0·4	0·1	1·2
Ba	84	20	9	23	87	88	20	771
Hf	1·0	0·7	0·6	0·8	3·7	3·7	3·8	6·4
Ta	0·08				0·67	0·70	0·7	1·4
Pb		28	29	37	6	7	113	151
Th	0·23	0·17	0·08	0·14	1·08	1·08	1·01	2·09
U	0·10	0·11	0·06	0·09	0·38	0·39	0·41	0·88

[1]Ni concentrations for these samples were determined by XRF.
THOL, tholeiitic basalt; PIC, picrite; HI-MG, high MgO basalt; CG, coarse-grained (sill or gabbro); MIN SIL, mineralized sill; OUTLIER, anomalous pillowed flow in plots; MA, Mount Arrowsmith; SL, Schoen Lake; KR, Karmutsen Range; QI, Quadra Island. Sample locations are given using the Universal Transverse Mercator (UTM) coordinate system (NAD83; zones 9 and 10). Analyses were performed at Activation Laboratory (ActLabs). $Fe_2O_3^*$ is total iron expressed as Fe_2O_3. LOI, loss on ignition. All major elements, Sr, V, and Y were measured by ICP quadrupole OES on solutions of fused samples; Cu, Ni, Pb, and Zn were measured by total dilution ICP; Cs, Ga, Ge, Hf, Nb, Rb, Ta, Th, U, Zr, and REE were measured by magnetic-sector ICP on solutions of fused samples; Co, Cr, and Sc were measured by INAA. Blanks are below detection limit. See Electronic Appendices 2 and 3 for complete XRF data and PCIGR trace element data, respectively. Major elements for sample 93G17 are normalized, anhydrous. Sample 5615A7 was analyzed by XRF. Samples from Quadra Island are not shown in figures.

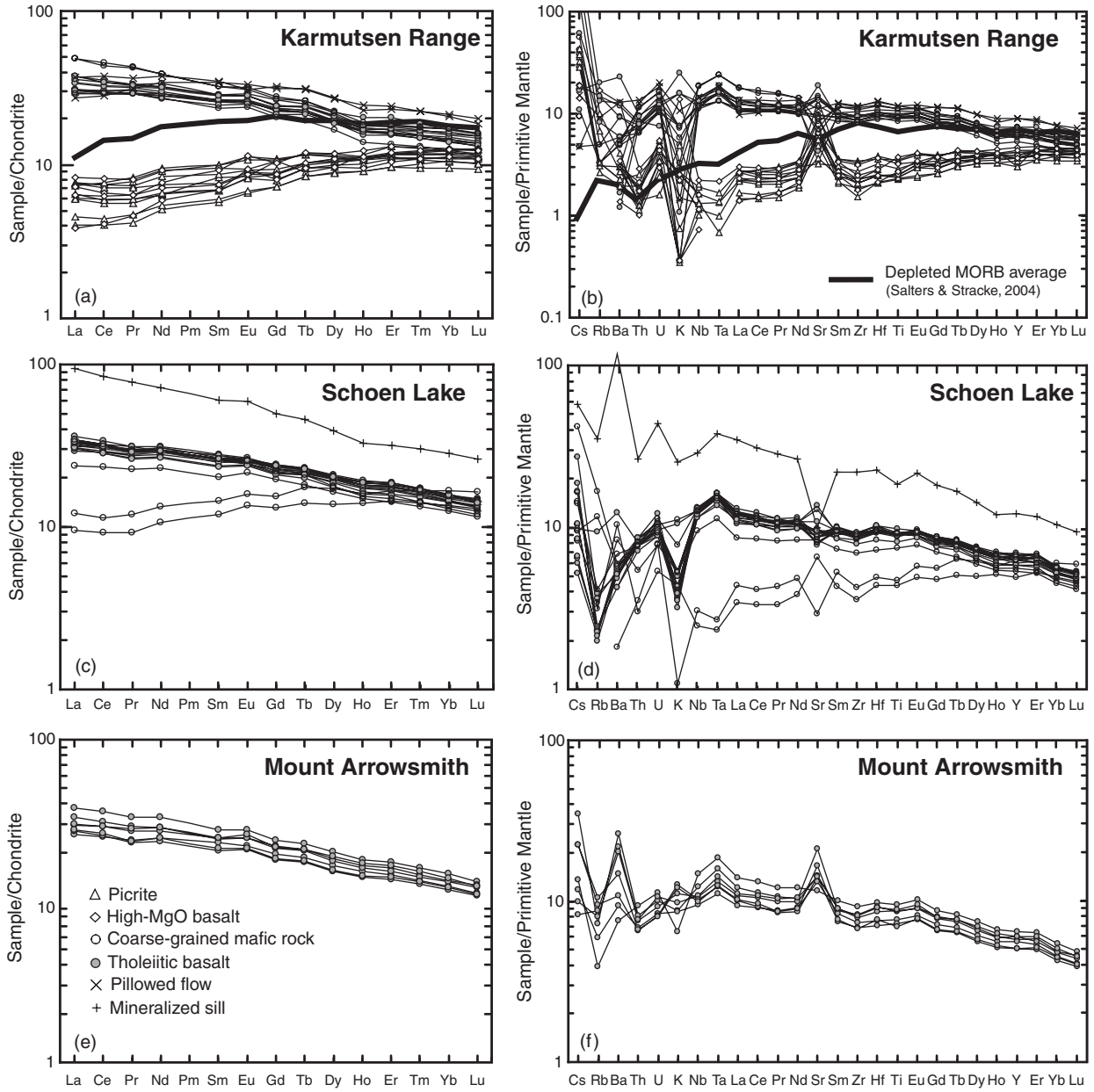

Fig. 7. Whole-rock REE and other incompatible-element concentrations for the Karmutsen Formation. (a), (c), and (e) are chondrite-normalized REE patterns for samples from each of the three main field areas on Vancouver Island. (b), (d), and (f) are primitive mantle-normalized trace-element patterns for samples from each of the three main field areas. All normalization values are from McDonough & Sun (1995). The clear distinction between LREE-enriched tholeiitic basalts and LREE-depleted picrites, the effects of alteration on the LILE (especially loss of K and Rb), and the different range for the vertical scale in (b) (extends down to 0·1) should be noted.

picritic and high-MgO basalt pillow lavas, extend to ~20 wt % MgO (Fig. 6, and references listed in the caption).

The tholeiitic basalts from the Karmutsen Range display a tight range of parallel light rare earth element (LREE)-enriched REE patterns ($La/Yb_{CN} = 2{\cdot}1–2{\cdot}4$; mean $2{\cdot}2 \pm 0{\cdot}2$), whereas the picrites and high-MgO basalts are characterized by sub-parallel LREE-depleted patterns ($La/Yb_{CN} = 0{\cdot}3–0{\cdot}7$; mean $0{\cdot}6 \pm 0{\cdot}2$) with lower REE abundances than the tholeiitic basalts (Fig. 7). Tholeiitic basalts from the Schoen Lake and Mount Arrowsmith areas have similar REE patterns to samples from the Karmutsen Range (Schoen Lake: $La/Yb_{CN} = 2{\cdot}1–2{\cdot}6$; mean $2{\cdot}3 \pm 0{\cdot}3$; Mount Arrowsmith: $La/Yb_{CN} = 1{\cdot}9–2{\cdot}5$; mean $2{\cdot}2 \pm 0{\cdot}4$), and the coarse-grained mafic rocks have similar REE patterns to the tholeiitic

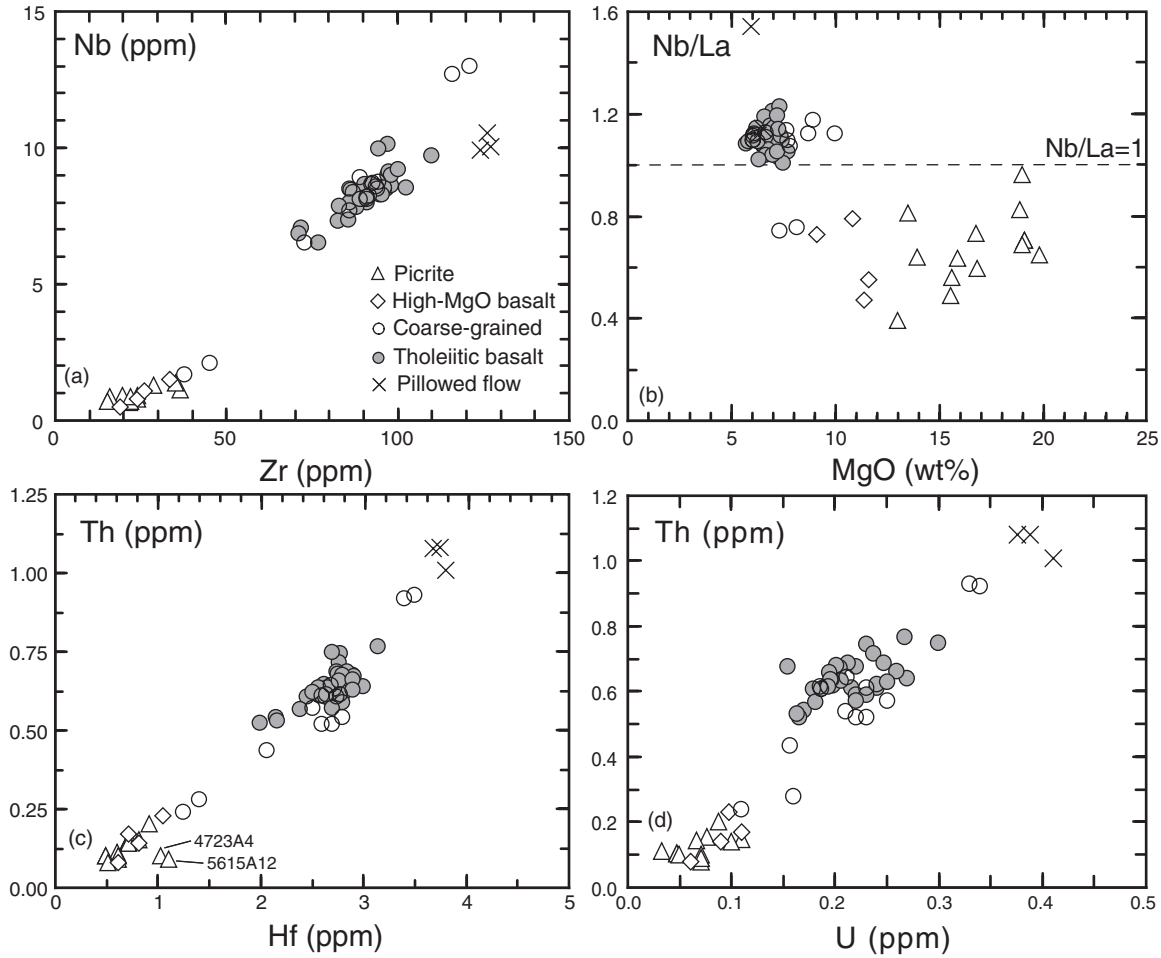

Fig. 8. Whole-rock trace-element concentrations and ratios for the Karmutsen Formation [except (b), which is vs wt % MgO]. (a) Nb vs Zr; (b) Nb/La vs MgO; (c) Th vs Hf; (d) Th vs U. There is a clear distinction between the tholeiitic basalts and picrites in Nb and Zr, both in concentration and the slope of each trend.

basalts ($La/Yb_{CN} = 2{\cdot}1–2{\cdot}9$; mean $2{\cdot}5 \pm 0{\cdot}8$). Two LREE-depleted coarse-grained mafic rocks from the Schoen Lake area have similar REE patterns ($La/Yb_{CN} = 0{\cdot}7$) to the picrites from the Keogh Lake area, indicating that this distinctive suite of rocks is exposed as far south as Schoen Lake; that is, 75 km away (Fig. 7). The anomalous pillowed flow from the Karmutsen Range has lower La/Yb_{CN} (1·3–1·8) than the main group of tholeiitic basalts from the Karmutsen Range (Fig. 7). The mineralized sill from the Schoen Lake area is distinctly LREE-enriched ($La/Yb_{CN} = 3{\cdot}3$), with the highest REE abundances ($La_{CN} = 94{\cdot}0$) of all Karmutsen samples; this may reflect contamination by adjacent sediment, also evident in thin-section where sulfide blebs are cored by quartz (Greene *et al.*, 2006).

The primitive mantle-normalized trace-element patterns (Fig. 7), and trace-element variations and ratios (Fig. 8), highlight the differences in trace-element concentrations between the four main groups of Karmutsen flood basalts on Vancouver Island. The tholeiitic basalts from all three areas have relatively smooth, parallel trace-element patterns; some samples have small positive Sr anomalies, relative to Nd and Sm, and many samples have prominent negative K anomalies relative to U and Nb, reflecting K loss during alteration (Fig. 7). The large ion lithophile elements (LILE) in the tholeiitic basalts (mainly Rb and K, not Cs) are depleted relative to the high field strength elements (HFSE) and LREE; LILE segments, especially for the Schoen Lake area (Fig. 7d), are remarkably parallel. The picrites and high-MgO basalts form a tight band of parallel trace-element patterns and are depleted in HFSE and LREE with positive Sr anomalies and relatively low Rb. The coarse-grained mafic rocks from the Karmutsen Range have identical trace-element patterns to the tholeiitic basalts. Samples from the Schoen Lake area have similar

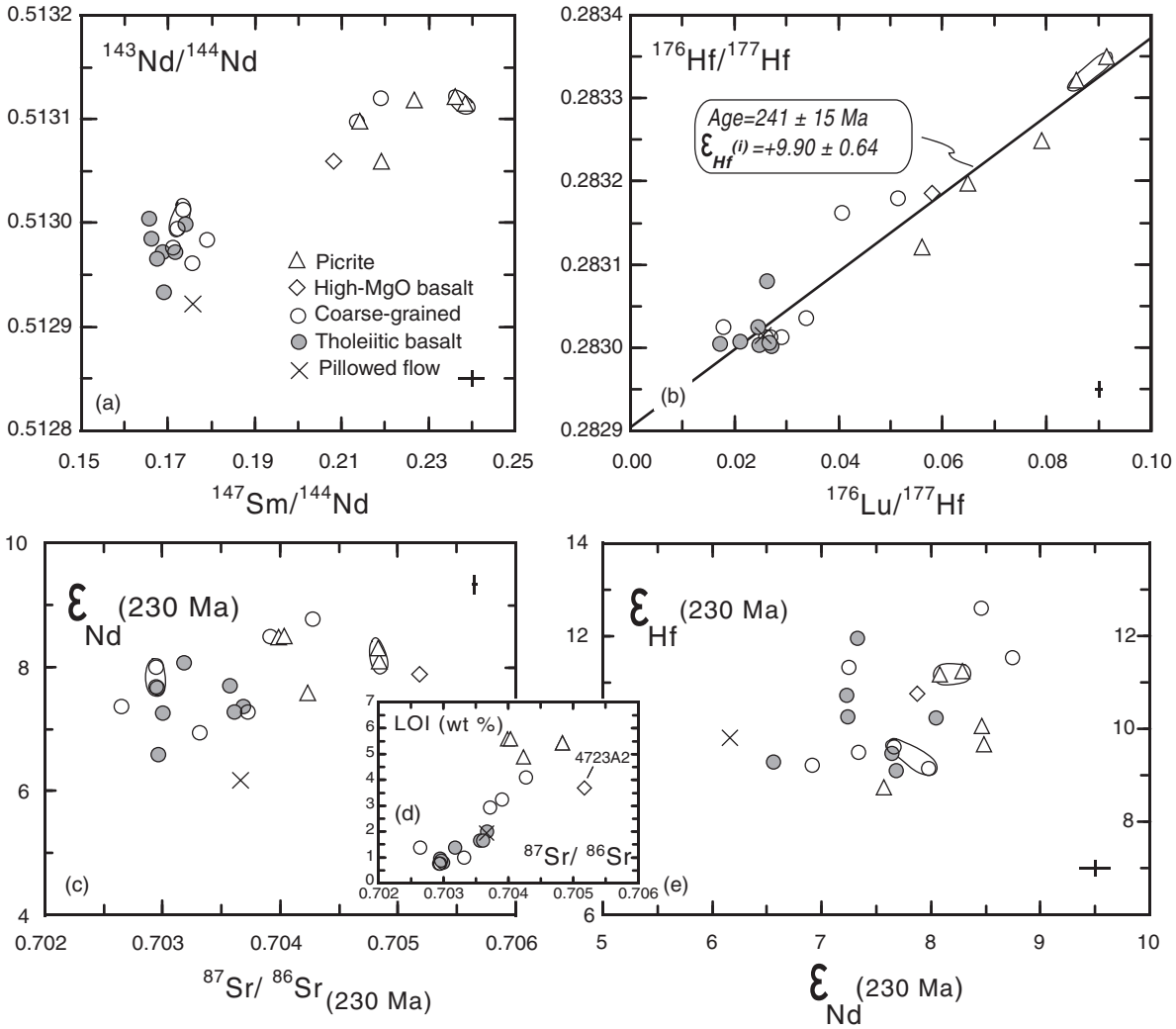

Fig. 9. Whole-rock Sr, Nd, and Hf isotopic compositions for the Karmutsen Formation. (a) $^{143}Nd/^{144}Nd$ vs $^{147}Sm/^{144}Nd$. (b) $^{176}Hf/^{177}Hf$ vs $^{176}Lu/^{177}Hf$. The slope of the best-fit line for all samples corresponds to an age of 241 ±15 Ma. (c) Initial ε_{Nd} vs $^{87}Sr/^{86}Sr$. Age-correction to 230 Ma. (d) LOI vs $^{87}Sr/^{86}Sr$. (e) Initial ε_{Hf} vs ε_{Nd}. Average 2σ error bars are shown in a corner of each panel. Complete chemical duplicates, shown in Tables 3 and 4 (samples 4720A7 and 4722A4), are circled in each plot.

trace-element patterns to the Karmutsen Range, except for the two LREE-depleted coarse-grained mafic rocks and the mineralized sill (Fig. 7d).

Sr–Nd–Hf–Pb isotopic compositions

A total of 19 samples from the four main groups of the Karmutsen Formation were selected for radiogenic isotopic geochemistry on the basis of major- and trace-element variation, stratigraphic position, and geographical location. The samples have overlapping age-corrected Hf and Nd isotope ratios and distinct ranges of Sr isotopic compositions (Fig. 9). The tholeiitic basalts, picrites, high-MgO basalt, and coarse-grained mafic rocks have initial $\varepsilon_{Hf} = +8{\cdot}7$ to $+12{\cdot}6$ and $\varepsilon_{Nd} = +6{\cdot}6$ to $+8{\cdot}8$ corrected for *in situ* radioactive decay since 230 Ma (Fig. 9; Tables 3 and 4). All the Karmutsen samples form a well-defined linear array in a Lu–Hf isochron diagram corresponding to an age of 241 ±15 Ma (Fig. 9). This is within error of the accepted age of the Karmutsen Formation and indicates that the Hf isotope systematics behaved as a closed system since *c.* 230 Ma. The anomalous pillowed flow has similar initial ε_{Hf} (+9·8) and slightly lower initial ε_{Nd} (+6·2) compared with the other Karmutsen samples. The picrites and high-MgO basalt have higher initial $^{87}Sr/^{86}Sr$ (0·70398–0·70518) than the tholeiitic basalts (initial $^{87}Sr/^{86}Sr = 0{\cdot}70306$–$0{\cdot}70381$) and the coarse-grained mafic rocks (initial $^{87}Sr/^{86}Sr = 0{\cdot}70265$–$0{\cdot}70428$)

Table 3: Sr and Nd isotopic compositions of Karmutsen basalts, Vancouver Island, B.C.

Sample:	Group	Area	Rb (ppm)	Sr (ppm)	$^{87}Sr/^{86}Sr$	$2\sigma_m$	$^{87}Rb/^{86}Sr$	$^{87}Sr/^{86}Sr_t$ 230 Ma	Sm (ppm)	Nd (ppm)	$^{143}Nd/^{144}Nd$	$2\sigma_m$	ε_{Nd}	$^{147}Sm/^{144}Nd$	$^{143}Nd/^{144}Nd_t$ 230 Ma	$\varepsilon_{Nd}(t)$
4718A2	THOL	MA	1·28	202	0·703247	6	0·0183	0·70319	4·60	16·8	0·513004	6	7·1	0·1656	0·51275	8·1
4718A7	THOL	MA	3·78	283	0·703702	8	0·0387	0·70358	4·79	16·6	0·512998	6	7·0	0·1742	0·51274	7·7
4719A2	THOL	MA	3·27	244	0·703811	9	0·0387	0·70368	4·48	16·1	0·512972	6	6·5	0·1688	0·51272	7·3
4719A3	THOL	MA	3·49	229	0·703757	6	0·0441	0·70361	4·22	14·8	0·512972	6	6·5	0·1718	0·51271	7·2
4720A4	THOL	SL	2·54	215	0·703066	8	0·0341	0·70295	5·77	21·0	0·512984	7	6·7	0·1662	0·51273	7·6
4721A2	THOL	SL	1·58	209	0·703076	7	0·0220	0·70300	4·05	14·6	0·512965	7	6·4	0·1675	0·51271	7·2
4721A4	THOL	SL	1·65	172	0·703062	7	0·0277	0·70297	5·48	19·6	0·512933	6	5·8	0·1691	0·51268	6·6
4720A6	CG	SL	6·11	123	0·703121	9	0·1438	0·70265	4·75	16·8	0·512976	7	6·6	0·1711	0·51272	7·3
4720A7	CG	SL	2·18	157	0·703078	6	0·0401	0·70295	4·96	17·3	0·513012	6	7·3	0·1735	0·51275	8·0
4720A7(dup)	CG	SL	1·79	140	0·703067	9	0·0369	0·70295	4·56	16·0	0·512994	6	6·9	0·1722	0·51273	7·7
4720A10	CG	SL	0·11	60	0·704294	7	0·0055	0·70428	2·05	5·7	0·513120	7	9·4	0·2191	0·51279	8·7
4724A3	CG	SL	1·44	135	0·703421	8	0·0310	0·70332	3·84	13·2	0·512961	6	6·3	0·1757	0·51270	6·9
5616A3	CG	KR	3·00	237	0·703849	7	0·0366	0·70373	3·82	12·9	0·512983	6	6·7	0·1790	0·51271	7·2
5617A1	CG	SL	2·00	58	0·704241	7	0·0998	0·70391	2·14	6·06	0·513097	7	9·0	0·2135	0·51278	8·5
4722A4	PIC	KR	3·16	77	0·705220	8	0·1184	0·70483	1·07	2·70	0·513115	6	9·3	0·2384	0·51276	8·1
4722A4(dup)	PIC	KR	3·16	77	0·705214	7	0·1184	0·70483	0·97	2·48	0·513122	6	9·4	0·2361	0·51277	8·3
4723A3	PIC	KR	1·65	69	0·704209	9	0·0696	0·70398	2·09	5·91	0·513098	7	9·0	0·2142	0·51278	8·5
4723A4	PIC	KR	1·43	110	0·704352	8	0·0375	0·70423	2·14	5·90	0·513060	10	8·2	0·2192	0·51273	7·6
4723A13	PIC	KR	0·67	63	0·704132	8	0·0312	0·70403	1·33	3·54	0·513118	7	9·4	0·2268	0·51278	8·5
4723A2	HI-MG	KR	8·23	269	0·705466	7	0·0885	0·70518	1·99	5·79	0·513059	8	8·2	0·2081	0·51275	7·9
4722A5	OUTLIER	KR	4·46	191	0·703877	7	0·0678	0·70366	6·10	21·0	0·512922	6	5·5	0·1756	0·51266	6·2

THOL, tholeiitic basalt; CG, coarse-grained mafic rock; PIC, picrite; HI-MG, high-MgO basalt; OUTLIER, anomalous pillowed flow in plots; KR, Karmutsen Range; SL, Schoen Lake; MA, Mount Arrowsmith. (dup) indicates complete chemistry duplicate from the sample sample powder. All isotopic and elemental analyses carried out at the PCIGR; the complete trace element analyses are given in Electronic Appendix 3.

overlap the ranges of the picrites and tholeiitic basalts (Fig. 9; Table 3).

The measured Pb isotopic compositions of the tholeiitic basalts are more radiogenic than those of the picrites, and the most magnesian Keogh Lake picrites have the least radiogenic Pb isotopic compositions. The range of initial Pb isotope ratios for the picrites is $^{206}Pb/^{204}Pb = 17{\cdot}868–18{\cdot}580$, $^{207}Pb/^{204}Pb = 15{\cdot}547–15{\cdot}562$, and $^{208}Pb/^{204}Pb = 37{\cdot}873–38{\cdot}257$, and the range for the tholeiitic basalts is $^{206}Pb/^{204}Pb = 18{\cdot}782–19{\cdot}098$, $^{207}Pb/^{204}Pb = 15{\cdot}570–15{\cdot}584$, and $^{208}Pb/^{204}Pb = 37{\cdot}312–38{\cdot}587$ (Fig. 10; Table 5). The coarse-grained mafic rocks overlap the range of initial Pb isotopic compositions for the tholeiitic basalts with $^{206}Pb/^{204}Pb = 18{\cdot}652–19{\cdot}155$, $^{207}Pb/^{204}Pb = 15{\cdot}568–15{\cdot}588$, and $^{208}Pb/^{204}Pb = 38{\cdot}153–38{\cdot}735$. One high-MgO basalt has the highest initial $^{206}Pb/^{204}Pb$ (19·242) and $^{207}Pb/^{204}Pb$ (15·590), and the lowest initial $^{208}Pb/^{204}Pb$ (37·676). The Pb isotopic ratios for Karmutsen samples define broadly linear relationships in Pb isotope plots. The age-corrected Pb isotopic compositions of several picrites have been affected by U and Pb (and/or Th) mobility during alteration (Fig. 10).

ALTERATION

The Karmutsen basalts have retained most of their original igneous structures and textures; however, secondary alteration and low-grade metamorphism have produced zeolitic- and prehnite–pumpellyite-bearing mineral assemblages (Table 1; Cho *et al.*, 1987). Alteration and metamorphism have primarily affected the distribution of the LILE and the Sr isotopic systematics. The Keogh Lake picrites have been affected more by alteration than the tholeiitic basalts and have higher LOI (up to 5·5 wt %), variable LILE, and higher measured Sr, Nd, and Hf and lower measured Pb isotope ratios than the tholeiitic basalts. Sr and Pb isotope compositions for picrites and tholeiitic basalts show a relationship with LOI (Figs 9 and 10), whereas Nd and Hf isotopic compositions do not correlate

Table 4: Hf isotopic compositions of Karmutsen basalts, Vancouver Island, B.C.

Sample	Group	Area	Lu (ppm)	Hf (ppm)	$^{176}Hf/^{177}Hf$	$2\sigma_m$	ε_{Hf}	$^{176}Lu/^{177}Hf$	$^{176}Hf/^{177}Hf_t$ 230 Ma	$\varepsilon_{Hf}(t)$
4718A2	THOL	MA	0·38	2·53	0·283007	4	8·3	0·0211	0·28291	10·2
4718A7	THOL	MA	0·46	2·41	0·283001	7	8·1	0·0271	0·28288	9·1
4719A2	THOL	MA	0·40	2·16	0·283079	5	10·9	0·0262	0·28296	12·0
4719A3	THOL	MA	0·37	2·12	0·283024	9	8·9	0·0246	0·28291	10·2
4720A4	THOL	SL	0·53	3·04	0·283002	7	8·1	0·0247	0·28289	9·5
4721A2	THOL	SL	0·36	2·99	0·283004	10	8·2	0·0173	0·28293	10·7
4721A4	THOL	SL	0·53	2·79	0·283006	6	8·3	0·0268	0·28289	9·3
4720A6	CG	SL	0·45	2·38	0·283012	5	8·5	0·0269	0·28289	9·5
4720A7	CG	SL	0·46	2·23	0·283012	6	8·5	0·0291	0·28288	9·1
4720A7(dup)	CG	SL	0·43	2·35	0·283012	4	8·5	0·0260	0·28290	9·6
4720A10	CG	SL	0·36	1·00	0·283179	7	14·4	0·0515	0·28295	11·5
4724A3	CG	SL	0·34	1·41	0·283035	8	9·3	0·0339	0·28288	9·2
5616A3	CG	KR	0·34	2·70	0·283024	7	8·9	0·0179	0·28294	11·3
5617A1	CG	SL	0·40	1·40	0·283161	4	13·8	0·0407	0·28298	12·6
4722A4	PIC	KR	0·29	0·48	0·283321	10	19·4	0·0857	0·28294	11·2
4722A4(dup)	PIC	KR	0·29	0·45	0·283350	11	20·4	0·0915	0·28294	11·3
4723A3	PIC	KR	0·45	0·98	0·283197	6	15·0	0·0649	0·28291	10·1
4723A4	PIC	KR	0·35	0·90	0·283121	26	12·3	0·0561	0·28287	8·7
4723A13	PIC	KR	0·35	0·63	0·283250	7	16·9	0·0791	0·28290	9·7
4723A2	HI-MG	KR	0·43	1·06	0·283186	7	14·7	0·0579	0·28293	10·8
4722A5	OUTLIER	KR	0·56	3·15	0·283015	6	8·6	0·0254	0·28290	9·8

THOL, tholeiitic basalt; CG, coarse-grained mafic rock; PIC, picrite; HI-MG, high-MgO basalt; OUTLIER, anomalous pillowed flow in plots; KR, Karmutsen Range; SL, Schoen Lake; MA, Mount Arrowsmith. (dup) indicates complete chemistry duplicate from the sample sample powder. All isotopic and elemental analyses were carried out at the PCIGR; the complete trace element analyses are given in Electronic Appendix 3.

with LOI (not shown). The relatively high apparent initial Sr isotopic compositions for the high-MgO lavas (up to 0·7052) probably resulted from post-magmatic loss of Rb, or an increase in $^{87}Sr/^{86}Sr$ through addition of seawater Sr (e.g. Hauff *et al.*, 2003). High-MgO lavas from the Caribbean plateau have similarly high $^{87}Sr/^{86}Sr$ compared with basalts (Révillon *et al.*, 2002). The correction for *in situ* decay on initial Pb isotopic ratios has been affected by mobilization of U and Th (and Pb) in the whole-rocks since their formation. A thorough acid leaching during sample preparation was used that has been shown to effectively remove alteration phases (Weis *et al.*, 2006; Nobre Silva *et al.*, in preparation). Whole-rock Sm/Nd ratios and age-correction of Nd isotopes may be affected by the leaching procedure for submarine rocks older than ~50 Ma (Thompson *et al.*, 2008; Fig. 9); there is, however, very little variation in Nd isotopic compositions of the picrites or tholeiitic basalts and this system does not appear to be disturbed by alteration. The HFSE abundances for tholeiitic and picritic basalts exhibit clear linear correlations in binary diagrams (Fig. 8), whereas plots of LILE vs HFSE are highly scattered (not shown) because of the mobility of some of the alkali and alkaline earth LILE (Cs, Rb, Ba, K) and Sr for most samples during alteration.

The degree of alteration in the Karmutsen samples does not appear to be related to eruption environment or depth of burial. Pillow rims are compositionally different from pillow cores (Surdam, 1967; Kuniyoshi, 1972), and aquagene tuffs are chemically different from isolated pillows within pillow breccias; however, submarine and subaerial basalts exhibit a similar degree of alteration. There is no clear correlation between the submarine and subaerial basalts and some commonly used chemical alteration indices (e.g. Ba/Rb vs K_2O/P_2O_5; Huang & Frey, 2005). There is also no definitive correlation between the petrographic alteration index (Table 1) and chemical alteration indices, although 10 of 13 tholeiitic basalts with the highest K and LILE abundances have the highest petrographic alteration index of three (see Table 1).

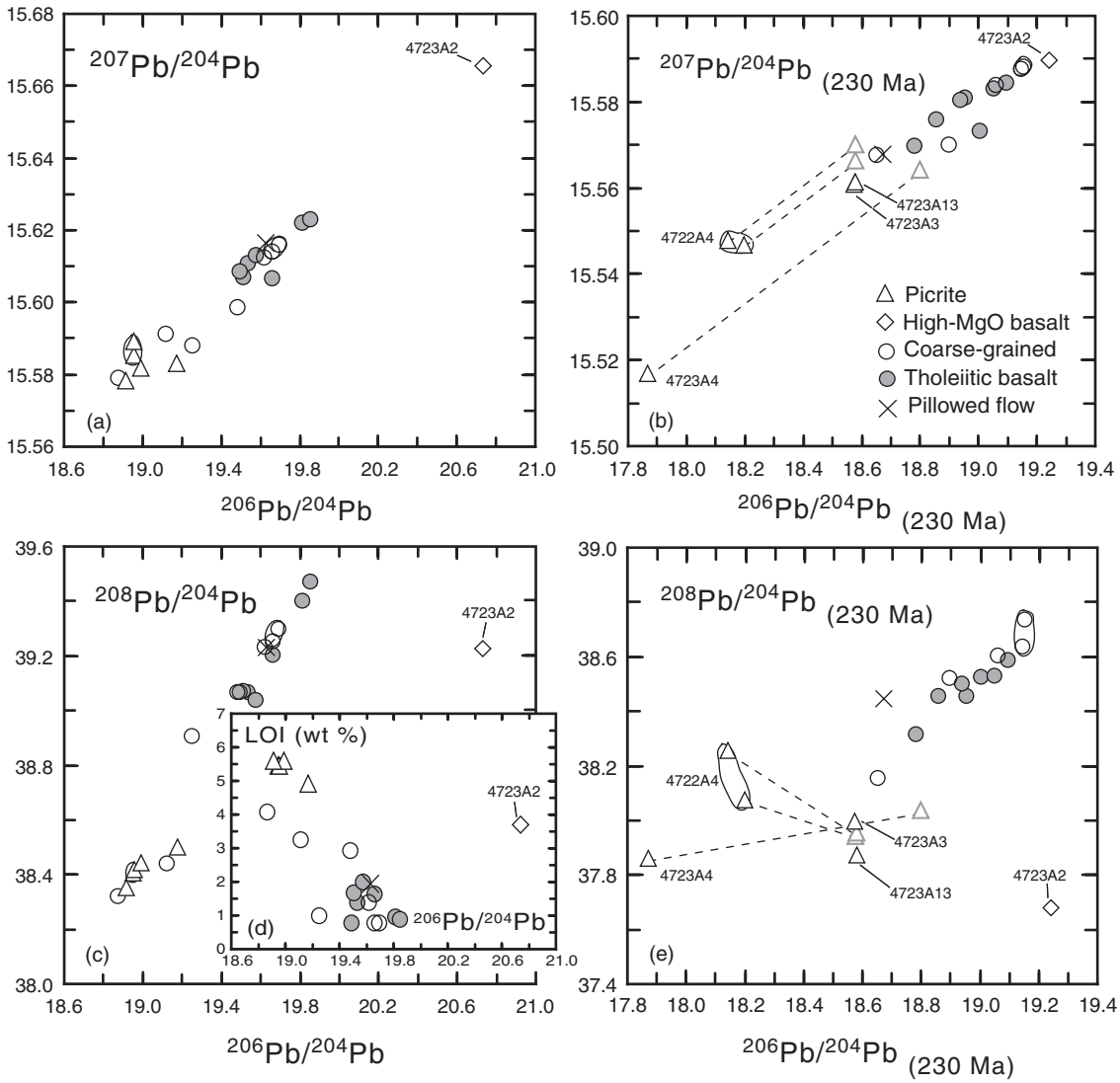

Fig. 10. Pb isotopic compositions of leached whole-rock samples measured by MC-ICP-MS for the Karmutsen Formation. Error bars are smaller than symbols. (a) Measured $^{207}Pb/^{204}Pb$ vs $^{206}Pb/^{204}Pb$. (b) Initial $^{207}Pb/^{204}Pb$ vs $^{206}Pb/^{204}Pb$. Age-correction to 230 Ma. (c) Measured $^{208}Pb/^{204}Pb$ vs $^{206}Pb/^{204}Pb$. (d) LOI vs $^{206}Pb/^{204}Pb$. (e) Initial $^{208}Pb/^{204}Pb$ vs $^{206}Pb/^{204}Pb$. Complete chemical duplicates, shown in Table 5 (samples 4720A7 and 4722A4), are circled in each plot. The dashed lines in (b) and (e) show the differences in age-corrections for two picrites (4723A4, 4722A4) using the measured U, Th, and Pb concentrations for each sample and the age-corrections when concentrations are used from the two picrites (4723A3, 4723A13) that appear to be least affected by alteration.

OLIVINE ACCUMULATION IN HIGH-MgO AND PICRITIC LAVAS

Geochemical trends and petrographic characteristics indicate that accumulation of olivine played an important role in the formation of the high-MgO basalts and picrites from the Keogh Lake area on northern Vancouver Island. The Keogh Lake samples show a strong linear correlation in plots of Al_2O_3, TiO_2, Sc, Yb, and Ni vs MgO and many of the picrites have abundant clusters of olivine pseudomorphs (Table 1; Fig. 11). There is a strong linear correlation between modal per cent olivine and whole-rock magnesium content; magnesium contents range between 10 and 19 wt % MgO and the proportion of olivine phenocrysts in these samples varies from 0 to 42 vol. % (Fig. 11). With a few exceptions, both the size range and median size of the olivine phenocrysts in most samples are comparable. The clear correlation between the proportion of olivine phenocrysts and whole-rock magnesium contents indicates that accumulation of olivine was directly responsible for the high MgO contents (>10 wt %) in most of the picritic lavas.

Table 5: Pb isotopic compositions of Karmutsen basalts, Vancouver Island, B.C.

Sample	Group	Area	U (ppm)	Th (ppm)	Pb (ppm)	$^{206}Pb/^{204}Pb$	$2\sigma_m$	$^{207}Pb/^{204}Pb$	$2\sigma_m$	$^{208}Pb/^{204}Pb$	$2\sigma_m$	$^{238}U/^{204}Pb$	$^{235}U/^{204}Pb$	$^{232}Th/^{204}Pb$	$^{206}Pb/^{204}Pb_t$ 230 Ma	$^{207}Pb/^{204}Pb_t$ 230 Ma	$^{208}Pb/^{204}Pb_t$ 230 Ma
4718A2	THOL	MA	0·18	0·56	0·71	19·5369	0·0021	15·6105	0·0017	39·0684	0·0035	16·0	0·116	53·2	18·957	15·581	38·455
4718A7	THOL	MA	0·17	0·52	0·54	19·5133	0·0016	15·6070	0·0015	39·0697	0·0042	20·1	0·146	65·7	18·782	15·570	38·312
4719A2	THOL	MA	0·18	0·47	0·68	19·5780	0·0015	15·6130	0·0012	39·0359	0·0032	17·6	0·127	46·4	18·940	15·581	38·501
4719A3	THOL	MA	0·14	0·45	0·52	19·6614	0·0017	15·6066	0·0015	39·2027	0·0042	18·0	0·131	58·8	19·007	15·573	38·524
4720A4	THOL	SL	0·21	0·72	0·65	19·8169	0·0012	15·6218	0·0010	39·3997	0·0026	21·0	0·153	75·7	19·053	15·583	38·527
4721A2	THOL	SL	0·25	0·72	0·91	19·4972	0·0019	15·6084	0·0015	39·0661	0·0039	17·6	0·127	53·1	18·859	15·576	38·454
4721A4	THOL	SL	0·17	0·61	0·54	19·8552	0·0009	15·6229	0·0008	39·4709	0·0020	20·9	0·151	76·7	19·098	15·584	38·587
4720A6	CG	SL	0·13	0·45	0·56	19·6209	0·0017	15·6124	0·0013	39·2307	0·0039	15·4	0·112	54·4	19·062	15·584	38·603
4720A7	CG	SL	0·13	0·48	0·61	19·6640	0·0009	15·6138	0·0006	39·2547	0·0019	14·2	0·103	53·5	19·149	15·588	38·638
4720A7(dup)	CG	SL	0·14	0·44	0·61	19·6951	0·0006	15·6157	0·0006	39·2975	0·0022	14·9	0·108	48·8	19·154	15·588	38·735
4720A10	CG	SL	0·05	0·11	0·51	18·8745	0·0018	15·5788	0·0016	38·3176	0·0042	6·1	0·044	14·3	18·652	15·568	38·153
4724A3	CG	SL	0·09	0·30	0·60	19·2520	0·0014	15·5880	0·0013	38·9072	0·0032	9·7	0·070	33·6	18·900	15·570	38·519
5616A3	CG	KR				19·4845	0·0007	15·5986	0·0006	39·0679	0·0015						
5617A1	CG	SL				19·1202	0·0007	15·5910	0·0006	38·4401	0·0016						
4722A4	PIC	KR	0·05	0·07	0·17	18·9514	0·0017	15·5852	0·0017	38·4063	0·0041	20·8	0·151	28·8	18·197	15·547	38·074
4722A4(dup)	PIC	KR	0·05	0·03	0·16	18·9539	0·0013	15·5890	0·0012	38·4186	0·0029	22·4	0·162	14·1	18·142	15·548	38·257
4723A3	PIC	KR	0·06	0·19	0·32	18·9873	0·0012	15·5820	0·0011	38·4434	0·0027	11·4	0·083	38·8	18·573	15·561	37·996
4723A4	PIC	KR	0·05		0·09	19·1733	0·0013	15·5832	0·0012	38·4984	0·0033	35·9	0·261	55·5	17·868	15·517	37·858
4723A13	PIC	KR	0·03	0·11	0·18	18·9131	0·0011	15·5784	0·0011	38·3518	0·0030	9·2	0·067	41·5	18·580	15·561	37·873
4723A2	HI-MG	KR	0·06	0·19	0·09	20·7321	0·0037	15·6656	0·0030	39·2295	0·0073	41·0	0·298	134·7	19·242	15·590	37·676
4722A5	OUTLIER	KR	0·33	0·82	0·81	19·6272	0·0016	15·6164	0·0012	39·2322	0·0034	26·3	0·191	68·0	18·673	15·568	38·448

THOL, tholeiitic basalt; CG, coarse-grained mafic rock; PIC, picrite; HI-MG, high-MgO basalt; OUTLIER, anomalous pillowed flow in plots; KR, Karmutsen Range; SL, Schoen Lake; MA, Mount Arrowsmith. (dup) indicates complete chemistry duplicate from the sample sample powder. All isotopic and elemental analyses were carried out at the PCIGR; the complete trace element analyses are given in Electronic Appendix 3.

DISCUSSION

The compositional and spatial development of the erupted lava sequences of the Wrangellia oceanic plateau on Vancouver Island provide information about the evolution of a mantle plume upwelling beneath oceanic lithosphere, in an analogous way to the interpretation of continental flood basalts. The Caribbean and Ontong Java plateaus are the two primary examples of accreted parts of oceanic plateaus that have been studied to date and comparisons can be made with the Wrangellia oceanic plateau. However, the Wrangellia oceanic plateau is a distinctive occurrence of an oceanic plateau because it formed on the crust of a Devonian to Mississippian intra-oceanic island arc overlain by Mississippian to Permian limestones and pelagic sediments. The nature and thickness of oceanic lithospheric mantle are considered to play a fundamental role in the decompression and evolution of a mantle plume and thus the compositions of the erupted lava sequences (Greene *et al.*, 2008). The geochemical and stratigraphic relationships observed in the Karmutsen Formation on Vancouver Island, and the focus of the subsequent discussion sections, provide constraints on: (1) the temperature and degree of melting required to generate the primary picritic magmas; (2) the composition of the mantle source; (3) the depth of melting and residual mineralogy in the source region; (4) the low-pressure evolution of the Karmutsen tholeiitic basalts; (5) the growth of the Wrangellia oceanic plateau.

Melting conditions and major-element composition of the primary magmas

The primary magmas to most flood basalt provinces are believed to be picritic (e.g. Cox, 1980) and they have been found in many continental and oceanic flood basalt sequences worldwide (e.g. Siberia, Karoo, Paraná–Etendeka, Caribbean, Deccan; Saunders, 2005). Near-primary picritic lavas with low total alkali abundances

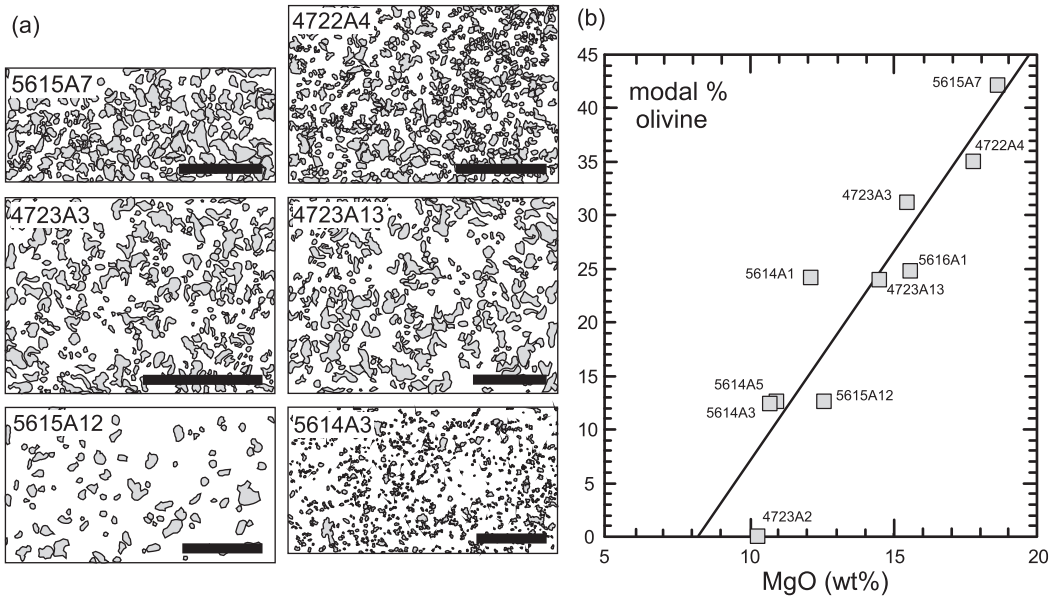

Fig. 11. Relationship between abundance of olivine phenocrysts and whole-rock MgO contents for the Keogh Lake picrites. (a) Tracings of olivine grains (gray) in six high-MgO samples made from high resolution (2400 d.p.i.) scans of petrographic thin-sections. Scale bars represent 10 mm; sample numbers are indicated at the upper left. (b) Modal% olivine vs whole-rock MgO. Continuous line is the best-fit line for 10 high-MgO samples. The areal proportion of olivine was calculated from raster images of olivine grains using ImageJ® image analysis software, which provides an acceptable estimation of the modal abundance (e.g. Chayes, 1954).

require high-degree partial melting of the mantle source (e.g. Herzberg & O'Hara, 2002). The Keogh Lake picrites from northern Vancouver Island are the best candidates for identifying the least modified partial melts of the mantle plume source, despite having accumulated olivine phenocrysts, and can be used to estimate conditions of melting and the composition of the primary magmas for the Karmutsen Formation.

Primary magma compositions, mantle potential temperatures and source melt fractions for the picritic lavas of the Karmutsen Formation were calculated from primitive whole-rock compositions using PRIMELT1.XLS software (Herzberg *et al.*, 2007) and are presented in Fig. 12 and Table 6. A detailed discussion of the computational method has been given by Herzberg & O'Hara (2002) and Herzberg *et al.* (2007); key features of the approach are outlined below.

Primary magma composition is calculated for a primitive lava by incremental addition of olivine and comparison with primary melts of mantle peridotite. Lavas that had experienced plagioclase and/or clinopyroxene fractionation are excluded from this analysis. All calculated primary magma compositions are assumed to be derived by accumulated fractional melting of fertile peridotite KR-4003. Uncertainties in fertile peridotite composition do not propagate to significant variations in melt fraction and mantle potential temperature; melting of depleted peridotite propagates to calculated melt fractions that are too high, but with a negligible error in mantle potential temperature. PRIMELT1.XLS calculates the olivine liquidus temperature at 1 atm, which should be similar to the actual eruption temperature of the primary magma, and is accurate to $\pm 30^{\circ}$C at the 2σ level of confidence. Mantle potential temperature is model dependent, with a precision that is similar to the accuracy of the olivine liquidus temperature (C. Herzberg, personal communication, 2008).

With regard to the evidence for accumulated olivine in the Keogh Lake picrites, it should not matter whether the modeled lava composition is aphyric or laden with accumulated olivine phenocrysts. PRIMELT1 computes the primary magma composition by adding olivine to a lava that has experienced olivine fractionation; in this way, it inverts the effects of fractional crystallization. The only requirement is that the olivine phenocrysts are not accidental or exotic to the lava compositions. Support for this procedure can be seen in the calculated olivine liquid-line-of-descent shown by the curved arrays with 5% olivine addition increments (Fig. 12c). Fractional crystallization of olivine from model primary magmas having 8·5–9·5 wt % FeO and 15·3–17·5 wt % MgO will yield arrays of derivative liquids and randomly sorted olivines that, in most but not all cases, connect the picrites and high-MgO basalts. A newer version of the PRIMELT software (Herzberg & Asimow, 2008) can perform olivine addition to and subtraction from lavas with highly variably olivine phenocryst contents, and yields results that converge with those shown in Fig. 12.

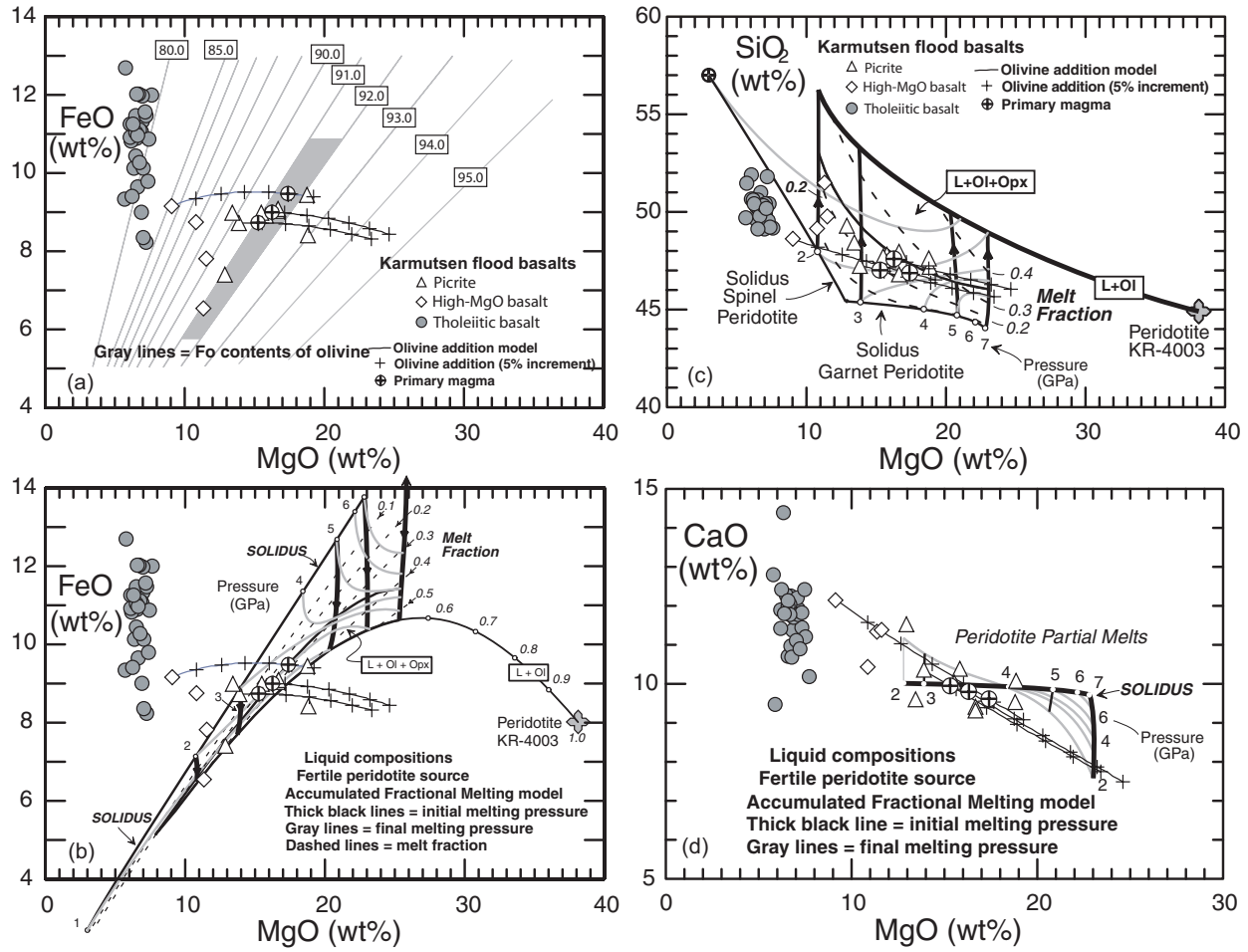

Fig. 12. Estimated primary magma compositions for three Keogh Lake picrites and high-MgO basalts (samples 4723A4, 4723A13, 5616A7) using the forward and inverse modeling technique of Herzberg *et al.* (2007). Karmutsen compositions and modeling results are overlain on diagrams provided by C. Herzberg. (a) Whole-rock FeO vs MgO for Karmutsen samples from this study. Total iron estimated to be FeO is 0·90. Gray lines show olivine compositions that would precipitate from liquid of a given MgO–FeO composition. Black lines with crosses show results of olivine addition (inverse model) using PRIMELT1 (Herzberg *et al.*, 2007). Gray field highlights olivine compositions with Fo contents of 91–92 predicted to precipitate. (b) FeO vs MgO showing Karmutsen lava compositions and results of a forward model for accumulated fractional melting of fertile peridotite KR-4003 (Kettle River Peridotite; Walter, 1998). (c) SiO_2 vs MgO for Karmutsen lavas and model results. (d) CaO vs MgO showing Karmutsen lava compositions and model results. To briefly summarize the technique [see Herzberg *et al.* (2007) for complete description], potential parental magma compositions for the high-MgO lava series were selected (highest MgO and appropriate CaO) and, using PRIMELT1 software, olivine was incrementally added to the selected compositions to show an array of potential primary magma compositions (inverse model). Then, using PRIMELT1, the results from the inverse model were compared with a range of accumulated fractional melts for fertile peridotite, derived from parameterization of the experimental results for KR-4003 from Walter (1998); forward model: Herzberg & O'Hara (2002). A melt fraction was sought that was unique to both the inverse and forward models (Herzberg *et al.*, 2007). A unique solution was found when there was a common melt fraction for both models in FeO–MgO and CaO–MgO–Al_2O_3–SiO_2 (CMAS) projection space. This modeling assumes that olivine was the only phase crystallizing and ignores chromite precipitation, and possible augite fractionation in the mantle (Herzberg & O'Hara, 2002). Results are best for a residue of spinel lherzolite (not pyroxenite). The presence of accumulated olivine in samples of the Keogh Lake picrites used as starting compositions does not significantly affect the results because we are modeling addition of olivine (see text for further description). The tholeiitic basalts cannot be used for modeling because they are all saturated in plag + cpx + ol. Thick black line for initial melting pressure at 4 GPa is not shown in (c) for clarity. Gray area in (a) indicates parental magmas that will crystallize olivine with Fo 91–92 at the surface. Dashed lines in (c) indicate melt fraction. Solidi for spinel and garnet peridotite are labelled in (c).

Table 6: Estimated primary magma compositions for Karmutsen basalts and other oceanic plateaus or islands

Sample	4723A4	4723A13	5616A7	93G171	Average	OJP*	Mauna Kea†	Gorgona‡
wt %								
SiO_2	47·0	47·6	46·9	47·8	47·3	48·0	46·3	46·1
TiO_2	0·68	0·46	0·60	0·46	0·55	0·62	1·93	0·56
Al_2O_3	15·3	14·3	13·0	13·9	14·1	12·3	9·6	11·7
Cr_2O_3	0·10	0·20	0·04	0·09	0·11	0·07	0·26	0·16
Fe_2O_3	1·03	1·08	0·89	1·09	1·02	0·90	1·08	1·18
FeO	8·7	9·0	9·5	8·9	9·0	9·2	10·3	10·1
MnO	0·15	0·15	0·16	0·19	0·16	0·17	0·18	0·18
MgO	15·3	16·3	17·4	16·1	16·3	16·8	18·3	18·8
CaO	9·9	9·8	9·6	10·3	9·9	10·3	10·1	10·0
Na_2O	1·59	0·90	1·74	1·01	1·31	1·36	1·67	1·04
K_2O	0·07	0·06	0·05	0·11	0·07	0·08	0·41	0·03
NiO	0·05	0·08	0·08	0·07	0·07	0·10	0·08	0·11
Eruption T (°C)	1354	1375	1397	1369	1374	1382	1415	1422
Potential T (°C)	1467	1491	1517	1486	1490	1500		1606
Fo content (olivine)	91·2	91·2	91·6	91·2	91·3	90·5	91·4	90·6
Melt fraction	0·23	0·27	0·26	0·27	0·26	0·27		0·28
%ol addition	4·2	2·5	24·3	0·8	7·9	18		

*Ontong Java primary magma composition for accumulated fraction melting (AFM) from Herzberg (2004).
†Mauna Kea primary magma composition is average of four samples of Herzberg (2006, table 1).
‡Gorgona primary magma composition for AFM for 1F, fertile source, from Herzberg & O'Hara (2002, table 4).
Total iron estimated to be FeO is 0·90.

The PRIMELT1 results indicate that, if the Karmutsen picritic lavas were derived from accumulated fractional melting of fertile peridotite, the primary magmas would have contained 15–17 wt % MgO and ~10 wt % CaO (Fig. 12; Table 6), formed from 23–27% partial melting, and would have crystallized olivine with a Fo content of ~91 (Fig. 12; Table 6). Calculated mantle temperatures for the Karmutsen picrites (~1490°C) indicate melting of anomalously hot mantle (100–200°C above ambient) compared with ambient mantle that produces mid-ocean ridge basalt (MORB; ~1280–1400°C; Herzberg *et al.*, 2007), which initiated between 3 and 4 GPa. Several picrites appear to be near-primary melts and required very little addition of olivine (e.g. sample 93G171, with measured 15·8 wt % MgO). These temperature and melting estimates of the Karmutsen picrites are consistent with decompression of hot mantle peridotite in an actively convecting plume head (i.e. plume initiation model). Three samples (picrite 5614A1 and high-MgO basalts 5614A3 and 5614A5) are lower in iron than the other Karmutsen lavas, with FeO in the 6·5–8·0 wt % range (Fig. 12c), and have MgO and FeO contents that are similar to primitive MORB from the Sequeiros fracture zone of the East Pacific Rise (EPR; Perfit *et al.*, 1996). These samples, however, differ from EPR MORB in having higher SiO_2 and lower Al_2O_3, and they are restricted geographically to one area (Sara Lake; Fig 2).

We therefore have evidence for primary magmas with MgO contents that range from a possible low of 11·0 wt % to as high as 17·4 wt % with inferred mantle potential temperatures from 1340 to 1520°C. This is similar to the range displayed by lavas from the Ontong Java Plateau determined by Herzberg (2004), who found that primary magma compositions, assuming a peridotite source, would contain ~17 wt % MgO and ~10 wt % CaO (Table 6), and that these magmas would have formed by 27% melting at a mantle potential temperature of ~1500°C (first melting occurring at 3·6 GPa). Fitton & Godard (2004) estimated 30% partial melting for the Ontong Java lavas based on the Zr contents of primary magmas of Kroenke-type basalt calculated by incremental addition of equilibrium olivine. However, if a considerable amount of eclogite was involved in the formation of the Ontong Java plateau magmas, the excess temperatures estimated by Herzberg *et al.* (2007) may not be required (Korenaga, 2005). The variability in mantle potential temperature for the Keogh Lake picrites is also similar to the wide range of temperatures that have been calculated for

lavas from single volcanoes in the Galapagos, Hawaii, and elsewhere by Herzberg & Asimow (2008). Those workers interpreted the range to reflect the transport of magmas from both the cool periphery and the hotter axis of a plume. A thermally heterogeneous plume will yield primary magmas with different MgO contents and the range of primary magma compositions and their inferred mantle potential temperatures for Karmutsen lavas may reflect melting from different parts of the plume.

Source of the Karmutsen Formation lavas

The Sr–Nd–Hf–Pb isotopic compositions of the Karmutsen volcanic rocks on Vancouver Island indicate that they formed from plume-type mantle containing a depleted component that is compositionally similar to but distinct from other oceanic plateaus that formed in the Pacific Ocean (e.g. Ontong Java and Caribbean; Fig. 13). Trace element and isotopic constraints can be used to test whether the depleted component of the Karmutsen Formation was intrinsic to the mantle plume, and distinct from the source of MORB, or the result of mixing or involvement of ambient depleted MORB mantle with plume-type mantle. The Karmutsen tholeiitic basalts have initial ε_{Nd} and $^{87}Sr/^{86}Sr$ ratios that fall within the range of basalts from the Caribbean Plateau (e.g. Kerr *et al.*, 1996, 1997; Hauff *et al.*, 2000; Kerr, 2003) and a range of Hawaiian isotope data (e.g. Frey *et al.*, 2005), and lie within and above the range for the Ontong Java Plateau (Tejada *et al.*, 2004; Fig. 13a). Karmutsen tholeiitic basalts with the highest initial ε_{Nd} and lowest initial $^{87}Sr/^{86}Sr$ lie within and just below the field for age-corrected northern EPR MORB at 230 Ma (e.g. Niu *et al.*, 1999; Regelous *et al.*, 1999). Initial Hf and Nd isotopic compositions for the Karmutsen samples are noticeably offset to the low side of the ocean island basalt (OIB) array (Vervoort *et al.*, 1999) and lie below, and slightly overlap, the low ε_{Hf} end of fields for Hawaii and the Caribbean Plateau (Fig. 13c); the Karmutsen samples mostly fall between, and slightly overlap, a field for age-corrected Pacific MORB at 230 Ma and Ontong Java (Mahoney *et al.*, 1992, 1994; Nowell *et al.*, 1998; Chauvel & Blichert-Toft, 2001). Karmutsen lava Pb isotope ratios overlap the broad range for the Caribbean Plateau and the linear trends for the Karmutsen samples intersect the fields for EPR MORB, Hawaii, and Ontong Java in ^{208}Pb–^{206}Pb space, but do not intersect these fields in ^{207}Pb–^{206}Pb space (Fig. 13d and e). The more radiogenic $^{207}Pb/^{204}Pb$ for a given $^{206}Pb/^{204}Pb$ of the Karmutsen basalts requires high U/Pb ratios at an ancient time when ^{235}U was abundant, similar to the Caribbean Plateau, and enriched in comparison with EPR MORB, Hawaii, and Ontong Java.

The low ε_{Hf}–low ε_{Nd} component of the Karmutsen basalts that places them below the OIB mantle array and partly within the field for age-corrected Pacific MORB can form from low ratios of Lu/Hf and high Sm/Nd over time (e.g. Salters & White, 1998). MORB will develop a Hf–Nd isotopic signature over time that falls below the mantle array. Low Lu/Hf can also lead to low $^{176}Hf/^{177}Hf$ from remelting of residues produced by melting in the absence of garnet (e.g. Salters & Hart, 1991; Salters & White, 1998). The Hf–Nd isotopic compositions of the Karmutsen Formation indicate the possible involvement of depleted MORB mantle; however, similar to Iceland (Fitton *et al.*, 2003), Nb–Zr–Y variations provide a way to distinguish between a depleted component within the plume and a MORB-like component. The Karmutsen basalts and picrites fall within the Iceland array and do not overlap the MORB field in a logarithmic plot of Nb/Y vs Zr/Y (Fig. 13b), using the fields established by Fitton *et al.* (1997). Similar to the depleted component within the Caribbean Plateau (Thompson *et al.*, 2003), the trend of Hf–Nd isotopic compositions towards Pacific MORB-like compositions is not followed by MORB values in Nb–Zr–Y systematics, and this suggests that the depleted component in the source of the Karmutsen basalts is distinct from the source of MORB and probably an intrinsic part of the plume. The relatively radiogenic Pb isotopic ratios and REE patterns distinct from MORB also support this interpretation.

Trace-element characteristics suggest the possible involvement of sub-arc lithospheric mantle in the generation of the Karmutsen picrites. Lassiter *et al.* (1995) suggested that mixing of a plume-type source with $\varepsilon_{Nd} + 6$ to $+7$ with arc material with low Nb/Th could reproduce the variations observed in the Karmutsen basalts; however, they concluded that the absence of low Nb/La ratios in their sample of tholeiitic basalts restricts the amount of arc lithosphere involved. The study of Lassiter *et al.* (1995) was based on major and trace element and Sr, Nd, and Pb isotopic data for a suite of 29 samples from Buttle Lake in the Strathcona Provincial Park on central Vancouver Island (Fig. 1). Whereas there are no clear HFSE depletions in the Karmutsen tholeiitic basalts, the low Nb/La (and Ta/La) of the Karmutsen picritic lavas in this study indicate the possible involvement of Paleozoic arc lithosphere on Vancouver Island (Fig. 8).

REE modeling: dynamic melting and source mineralogy

The combined isotopic and trace-element variations of the picritic and tholeiitic Karmutsen lavas indicate that differences in trace elements may have originated from different melting histories. For example, the Lu/Hf ratios of the Karmutsen picritic lavas (mean 0·08) are considerably higher than those in the tholeiitic basalts (mean 0·02); however, the small range of overlapping initial ε_{Hf} values for the two lava suites suggests that these differences developed during melting within the plume (Fig. 9b). Below, we model the effects of source mineralogy and depth of

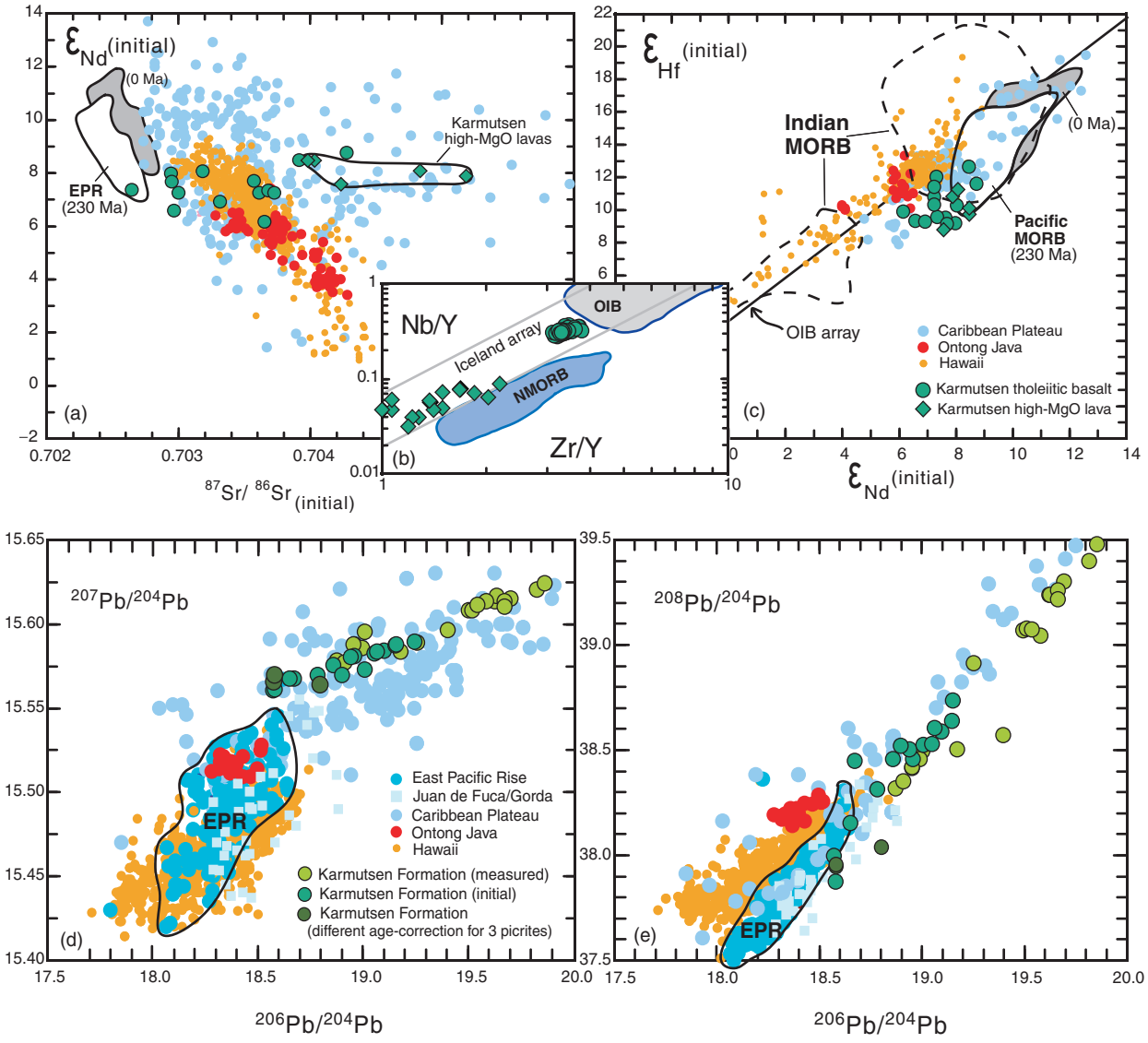

Fig. 13. Comparison of age-corrected (230 Ma) Sr–Nd–Hf–Pb isotopic compositions for Karmutsen flood basalts on Vancouver Island with age-corrected OIB and MORB and Nb–Zr–Y variation. (a) Initial ε_{Nd} vs $^{87}Sr/^{86}Sr$. (b) Nb/Y and Zr/Y variation (after Fitton *et al.*, 1997). (c) Initial ε_{Hf} vs ε_{Nd}. (d) Measured and initial $^{207}Pb/^{204}Pb$ vs $^{206}Pb/^{204}Pb$. (e) Measured and initial $^{208}Pb/^{204}Pb$ vs $^{206}Pb/^{204}Pb$. References for data sources are listed in Electronic Appendix 4. Most of the compiled data were extracted from the GEOROC database (http://georoc.mpch-mainz.gwdg.de/georoc/). OIB array line in (c) is from Vervoort *et al.* (1999). EPR, East Pacific Rise. Several high-MgO samples affected by secondary alteration were not plotted for clarity in Pb isotope plots. Estimation of fields for age-corrected Pacific MORB and EPR at 230 Ma were made using parent–daughter concentrations (in ppm) from Salters & Stracke (2004) of Lu = 0·063, Hf = 0·202, Sm = 0·27, Nd = 0·71, Rb = 0·086, and Sr = 8·36. In the Nb/Y vs Zr/Y plot, the normal (N)-MORB and OIB fields, not including Icelandic OIB, are from data compilations of Fitton *et al.* (1997, 2003). The OIB field is data from 780 basalts (MgO > 5 wt %) from major ocean islands given by Fitton *et al.* (2003). The N-MORB field is based on data from the Reykjanes Ridge, EPR, and Southwest Indian Ridge from Fitton *et al.* (1997). The two parallel gray lines in (b) (Iceland array) are the limits of data for Icelandic rocks.

melting on differences in trace-element concentrations in the tholeiitic basalts and picrites.

Dynamic melting models simulate progressive decompression melting where some of the melt fraction is retained in the residue and only when the degree of partial melting is greater than the critical mass porosity, and the source becomes permeable, is excess melt extracted from the residue (Zou, 1998). For the Karmutsen lavas, evolution of trace element concentrations was simulated using the incongruent dynamic melting model developed by Zou & Reid (2001). Melting of the mantle at pressures greater than ~1 GPa involves incongruent melting (e.g. Longhi, 2002)

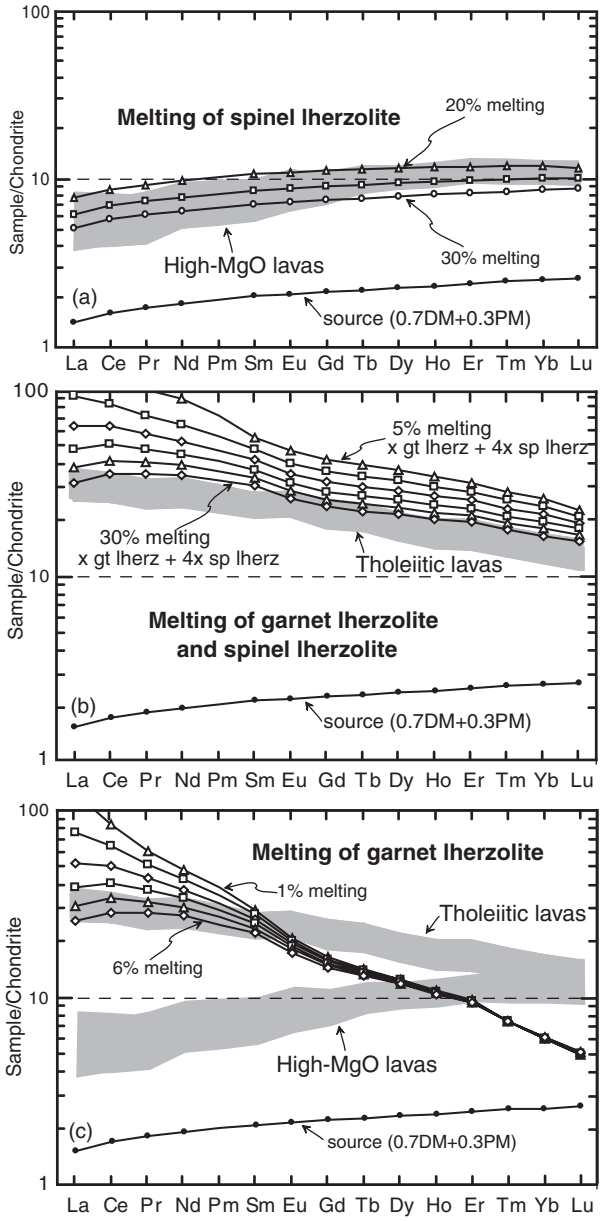

Fig. 14. Trace-element modeling results for incongruent dynamic mantle melting for picritic and tholeiitic lavas from the Karmutsen Formation. Three steps of modeling are shown: (a) melting of spinel lherzolite compared with high-MgO lavas; (b) melting of garnet lherzolite and spinel lherzolite compared with tholeiitic lavas; (c) melting of garnet lherzolite compared with tholeiitic and picritic lavas. Shaded fields in each panel for tholeiitic basalts and picrites are labeled. Patterns with symbols in each panel are modeling results (patterns are 5% melting increments in (a) and (b) and 1% increments in (c). PM, primitive mantle; DM, depleted MORB mantle; gt lherz, garnet lherzolite; sp lherz, spinel lherzolite. In (b), the ratios of per cent melting for garnet and spinel lherzolite are indicated (*x* gt lherz + 4*x* sp lherz means that for 5% melting, 1% melt in garnet facies and 4% melt in spinel facies, where *x* is per cent melting in the interval of modeling). The ratio of the respective melt proportions in the aggregate melt (*x* gt lherz + 4*x* sp lherz) was kept constant and this ratio of melt contribution provided the best fit to the data. A range of proportion of source components (0·7DM + 0·3PM to 0·9DM + 0·1PM) can reproduce the variation in the high-MgO lavas. Melting modeling uses the formulation of Zou & Reid (2001); an example calculation is shown in their Appendix. PM from McDonough & Sun (1995) and DM from Salters & Stracke (2004). Melt reaction coefficients of spinel lherzolite from Kinzler & Grove (1992) and garnet lherzolite from Walter (1998). Partition coefficients from Salters & Stracke (2004) and Shaw (2000) were kept constant. Source mineralogy for spinel lherzolite (0·18cpx:0·27opx:0·52ol:0·03sp) from Kinzler (1997) and for garnet lherzolite (0·34cpx:0·08opx:0·53ol:0·05gt) from Salters & Stracke (2004). A range of source compositions for melting of spinel lherzolite (0·7DM + 0·3PM to 0·3DM + 0·7PM) reproduce REE patterns similar to those of the high-MgO lavas, with best fits for 22–25% melting and 0·7DM + 0·3PM source composition. Concentrations of tholeiitic basalts cannot be reproduced from an entirely primitive or depleted source.

with olivine being produced during the reaction cpx + opx + sp = melt + ol for spinel peridotites. The modeling used coefficients for incongruent melting reactions based on experiments on lherzolite melting (e.g. Kinzler & Grove, 1992; Longhi, 2002) and was separated into: (1) melting of spinel lherzolite; (2) two combined intervals of melting, for a garnet lherzolite (gt lherz) and spinel lherzolite (sp lherz) source; (3) melting of garnet lherzolite. The model solutions are non-unique and a range in degree of melting, partition coefficients, melt reaction coefficients, and proportion of mixed source components is possible to achieve acceptable solutions (see Fig. 14 caption for description of modeling parameters and uncertainties).

The LREE-depleted high-MgO lavas require melting of a depleted spinel lherzolite source (Fig. 14a). The modeling results indicate a high degree of melting (22–25%), similar to the results from PRIMELT1 based on major-element variations (discussed above), of a LREE-depleted source. The high-MgO lavas lack a residual garnet signature. The enriched tholeiitic basalts involved melting of both garnet and spinel lherzolite and represent aggregate melts produced from continuous melting throughout the depth of the melting column (Fig. 14b). Trace-element concentrations in the tholeiitic and picritic lavas are not consistent with low-degree melting of garnet lherzolite alone (Fig. 14c). The modeling results indicate that the aggregate melts that formed the tholeiitic basalts would have involved lesser proportions of enriched, small-degree melts (1–6% melting) generated at depth and greater amounts of depleted, high-degree melts (12–25%) generated at lower pressure (a ratio of garnet lherzolite to spinel lherzolite melt of 1:4 provides the best fits; see Fig. 14b and description in figure caption). The total degree of melting for the tholeiitic basalts was high (23–27%), similar to the degree of partial melting in the spinel lherzolite facies for the primary melts that erupted as the Keogh Lake picrites, of a source that was also probably depleted in LREE.

The uncertainty in the composition of the source in the spinel lherzolite melting model for the high-MgO lavas precludes determining whether the source was more depleted in incompatible trace elements than the source of the tholeiitic lavas (see Fig. 14 caption for description). It is possible that early high-pressure, low-degree melting left a residue within parts of the plume (possibly the hotter, interior portion) that was depleted in trace elements (e.g. Elliott *et al.*, 1991); further decompression and high-degree melting of such depleted regions could then have generated the depleted high-MgO Karmutsen lavas. Shallow, high-degree melting would preferentially sample depleted regions, whereas deeper, low-degree melting may not sample more refractory, depleted regions (e.g. Caribbean; Escuder-Viruete *et al.*, 2007). The picrites lie at the high end of the range of Nd isotopic compositions and have low Nb/Zr, similar to depleted Icelandic basalts (Fitton *et al.*, 2003); therefore, the picrites may represent the parts of the mantle plume that were the most depleted prior to the initiation of melting. As Fitton *et al.* (2003) suggested, these depleted melts may only rarely be erupted without combining with more voluminous, less depleted melts and they may be detected only as undifferentiated, small-volume flows, like the Keogh Lake picrites within the Karmutsen Formation on Vancouver Island. Decompression melting within the mantle plume initiated within the garnet stability field (~3·5–2·5 GPa), at high mantle potential temperatures ($T_p > 1450^\circ C$), and proceeded beneath oceanic arc lithosphere within the spinel stability field (~2·5–0·9 GPa), where more extensive degrees of melting could occur.

Magmatic evolution of Karmutsen tholeiitic basalts

Primary magmas in large igneous provinces leave extensive coarse-grained cumulate residues within or below the crust; these mafic and ultramafic plutonic sequences represent a significant proportion of the original magma that partially crystallized at depth (e.g. Farnetani *et al.*, 1996). For example, seismic and petrological studies of Ontong Java (e.g. Farnetani *et al.*, 1996), combined with the use of MELTS (Ghiorso & Sack, 1995), indicate that the volcanic sequence may represent only ~40% of the total magma reaching the Moho. Neal *et al.* (1997) estimated that 30–45% fractional crystallization took place for the Ontong Java magmas and produced cumulate thicknesses of 7–14 km corresponding to 11–22 km of flood basalts, depending on the presence of pre-existing oceanic crust and the total crustal thickness (25–35 km). Interpretations of seismic velocity measurements suggest the presence of pyroxene and gabbroic cumulates ~9–16 km thick beneath the Ontong Java Plateau (e.g. Hussong *et al.*, 1979).

Wrangellia is characterized by high crustal velocities in seismic refraction lines, which is indicative of mafic plutonic rocks extending to depth beneath Vancouver Island (Clowes *et al.*, 1995). Wrangellia crust is ~25–30 km thick beneath Vancouver Island and is underlain by a strongly reflective zone of high velocity and density that has been interpreted as a major shear zone where lower Wrangellia lithosphere was detached (Clowes *et al.*, 1995). The vast majority of the Karmutsen flows are evolved tholeiitic lavas (e.g. low MgO, high FeO/MgO), indicating an important role for partial crystallization of melts at low pressure, and a significant portion of the crust beneath Vancouver Island has seismic properties that are consistent with crystalline residues from partially crystallized Karmutsen magmas. To test the proportion of the primary magma that fractionated within the crust, MELTS (Ghiorso & Sack, 1995) was used to simulate fractional crystallization using several estimated primary magma compositions from the PRIMELT1 modeling results. The major-element composition of the primary magmas could not be estimated for the tholeiitic basalts because of extensive plag + cpx + ol fractionation, and thus the MELTS modeling of the picrites is used as a proxy for the evolution of major elements in the volcanic sequence. A pressure of 1 kbar was used with variable water contents (anhydrous and 0·2 wt % H_2O), calculated at the quartz–fayalite–magnetite (QFM) oxygen buffer. Experimental results from Ontong Java indicate that most crystallization occurs in magma chambers shallower than 6 km deep (<2 kbar; Sano & Yamashita, 2004); however, some crystallization may take place at greater depths (3–5 kbar; Farnetani *et al.*, 1996).

A selection of the MELTS results are shown in Fig. 15. Olivine and spinel crystallize at high temperature until ~15–20 wt % of the liquid mass has fractionated, and the residual magma contains 9–10 wt % MgO (Fig. 15f). At 1235–1225°C plagioclase begins crystallizing, and between 1235 and 1190°C olivine ceases crystallizing and clinopyroxene saturates (Fig. 15f). As expected, the addition of clinopyroxene and plagioclase to the crystallization sequence causes substantial changes in the composition of the residual liquid; FeO and TiO_2 increase and Al_2O_3 and CaO decrease, while the decrease in MgO lessens considerably (Fig. 15). The near-vertical trends for the Karmutsen tholeiitic basalts, especially for CaO, do not match the calculated liquid-line-of-descent very well, which misses many of the high-CaO, high-Al_2O_3, low-FeO basalts. A positive correlation between Al_2O_3/CaO and Sr/Nd indicates that accumulation of plagioclase played a major role in the evolution of the tholeiitic basalts (Fig. 15g). Increasing the crystallization pressure slightly and the water content of the melts does not systematically improve the match of the MELTS models to the observed data.

The MELTS results indicate that a significant proportion of the crystallization takes place before plagioclase (~15–20% crystallization) and clinopyroxene (~35–45%

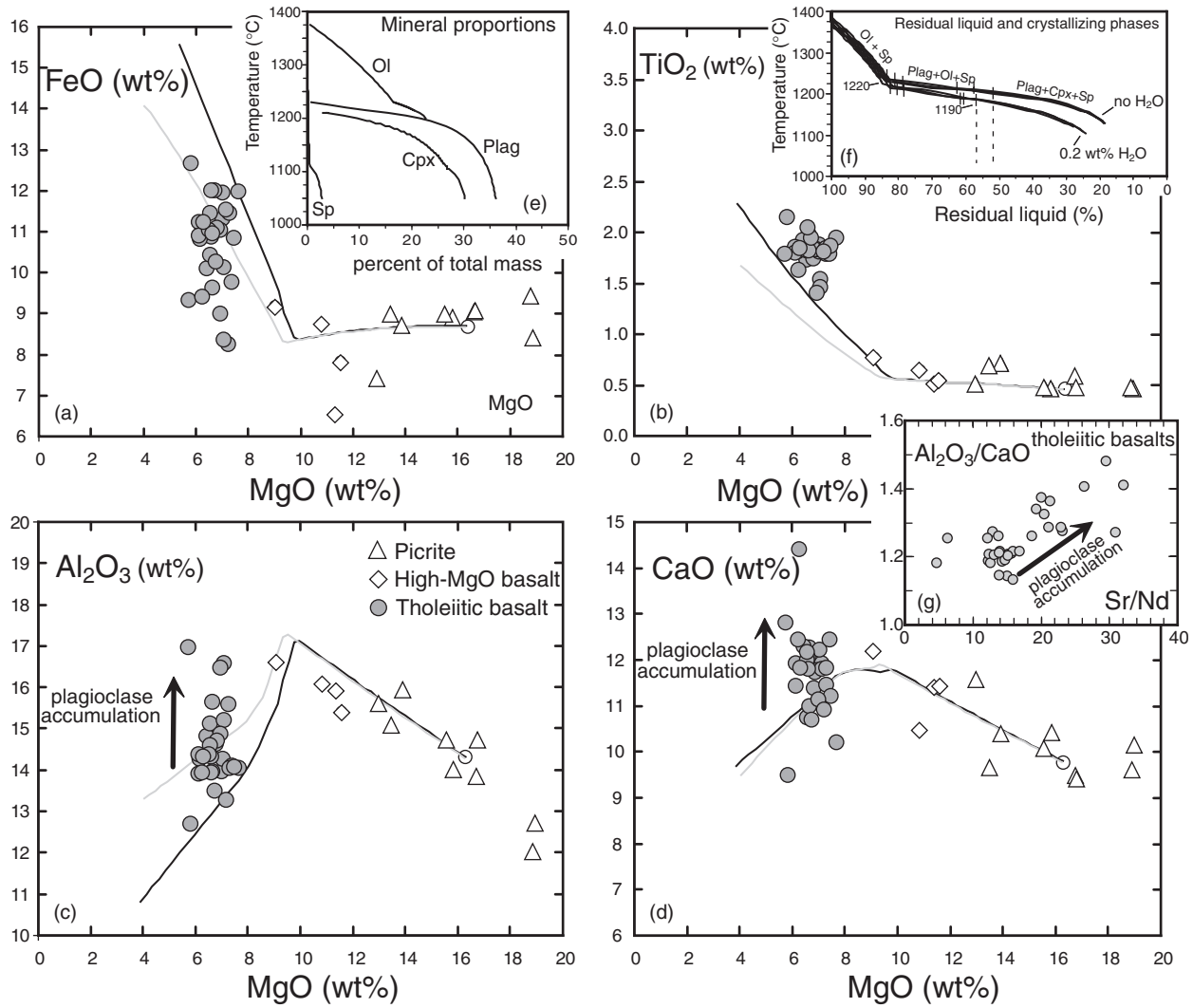

Fig. 15. Forward fractional crystallization modeling results for major elements from MELTS (Ghiorso & Sack, 1995) compared with picritic and tholeiitic lavas from the Karmutsen Formation. (a–d) Major-element compositions of residual liquids compared with Karmutsen lava compositions. For clarity, the results are shown only for one starting composition (open circle), using the composition of the estimated primary magma for the high-MgO lava series from the modeling technique of Herzberg *et al.* (2007) for sample 4723A13, as shown in Fig. 12. The estimated primary magmas for samples 4723A3 and 93G171 yield similar results. A pressure of 1 kbar was used with no H_2O and 0·2 wt % H_2O, calculated at QFM; black line is anhydrous and grey line is 0·2 wt % H_2O. The end-point for the anhydrous result is at 78% fractionation and 1130°C and the end-point for the result with 0·2 wt % H_2O is 75% fractionation and 1110°C. (e) Mineral proportions of crystallized phases from one MELT run (sample 4723A13) with no H_2O. (f) Per cent residual liquid vs temperature labelled with intervals of crystallizing phases. (g) Al_2O_3/CaO vs Sr/Nd for the tholeiitic basalts.

crystallization) join the crystallization sequence. These results suggest that >45% crystallization of the primary magmas occurred (estimated from the residual liquid per cent in Fig. 15f) and, if the original flood basalt stratigraphy on Vancouver Island was ~6 km thick, at least an equivalent amount of complementary plutonic rocks should have crystallized. The Karmutsen basalts and their plutonic residues thus represent a significant addition of crust (perhaps >12 km thickness), previously thickened during the formation of the underlying Paleozoic arc.

Growth of the Wrangellia oceanic plateau on Vancouver Island

The extrusive part of the Wrangellia oceanic plateau on Vancouver Island was constructed in a three-layer sequence of mostly tholeiitic basalts with a restricted range of composition (Fig. 16). The plateau overlies Devonian to Mississippian arc volcanic sequences and marine sediments of Mississippian to Permian ages that are intruded by gabbroic rocks related to the flood basalts. The volcanic stratigraphy of the Wrangellia plateau formed

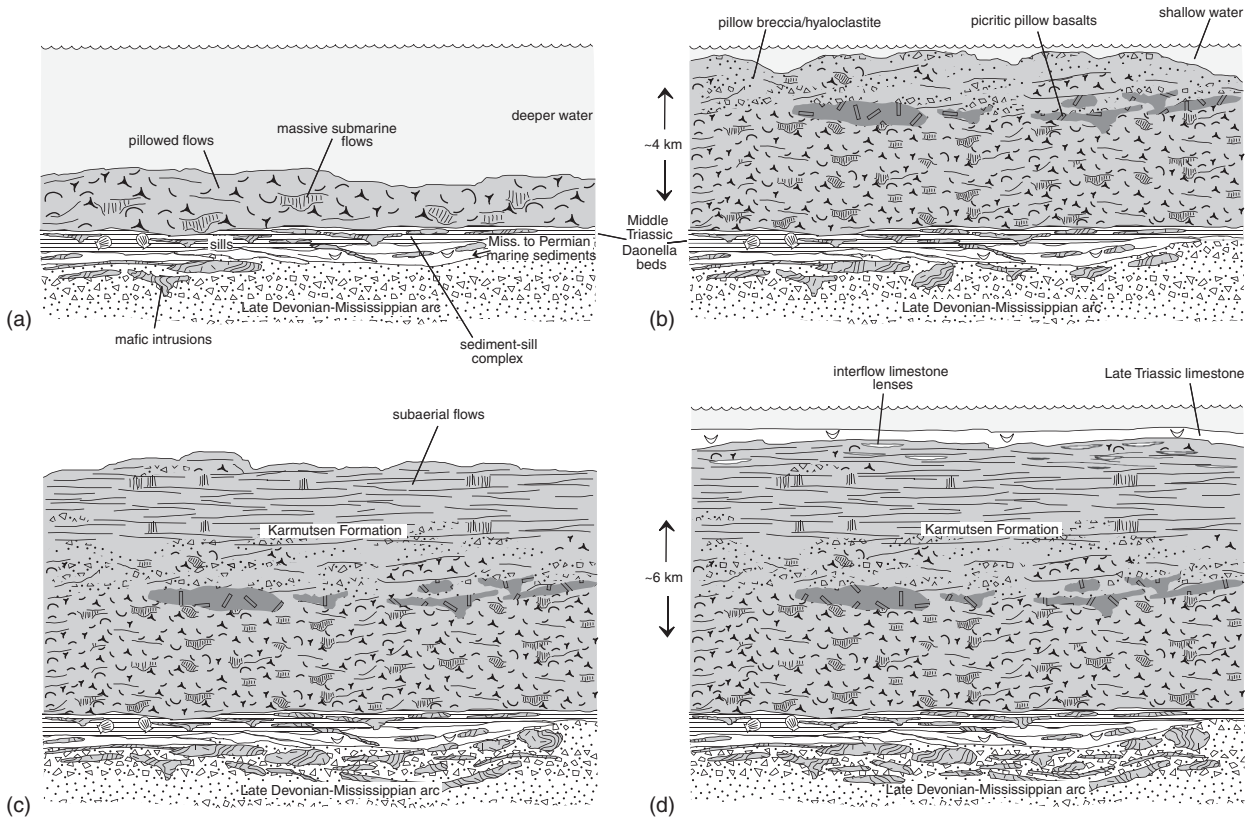

Fig. 16. Growth of the Wrangellia oceanic plateau on Vancouver Island. (a) Deep-water eruptive phase of pillowed and massive submarine flows, with almost no intervening sediments, onto Middle Triassic shale containing *Daonella* beds (*c.* 235–232 Ma). The basement of the plateau is composed of Devonian to Mississippian arc sequences overlain by Mississippian to Permian carbonates and siliciclastic sediments. (b) Shallow-water flow emplacement with increasing proportion of volcaniclastics resulted primarily from cooling–contraction granulation. Picritic pillow basalts occur primarily near the transition between pillowed submarine flows and volcaniclastic units. Pillowed and massive flows occur locally within the volcaniclastic unit. (c) Emergent stage of growth consists of overlapping subaerial flow fields, similar to continental flood basalts, with pahoehoe flow structures. Multi-tiered columnar jointing occurrs locally in response to ponding of flows (e.g. Bondre *et al.*, 2004). Interflow carbonate deposits and plagioclase megacrystic flows developed locally during the waning stage of volcanism. (d) Post-volcanic subsidence and deposition of Late Carnian to Norian (*c.* 212–223 Ma) platform carbonates on top of the plateau. Units are labeled in the diagrams. Thicknesses of the underlying units are not to scale.

in a single eruptive phase (*c.* 231–225 Ma) as an emergent basalt sequence during a deeper-water, shallow-water, and subaerial stage, and subsided below sea level relatively soon after its formation (Fig. 16). The deeper-water stage contains pillowed and massive submarine flows (~3000 m thick) that built up the submarine volcanic edifice from the seafloor. The lowest pillow basalts were emplaced on unconsolidated and lithified fine-grained siliciclastic and carbonaceous sediments containing *Daonella* beds (*c.* 235–232 Ma) that are intruded by abundant Karmutsen mafic sills (Fig. 16a). The different pillowed and massive submarine flows resulted primarily from different effusive rates and local topography. Some of the massive submarine flows, commonly recognized by radiating columnar jointing, represent master tubes for the delivery of lava to distal parts of submarine flow fields. The pillowed flows, which commonly have uneven topography in modern sequences, may have served as levees to the massive submarine flows, rather than allowing unobstructed spreading and inflation typical of the massive subaerial flows that form on shallow slopes in continental flood basalt provinces (e.g. Self *et al.*, 1997). The rapid succession of flows is evident by the near absence of sediment between submarine flows. Minor volumes of picritic pillow lavas occur in the upper part of the pillowed flow sequence in areas of the plateau exposed on northern Vancouver Island (Fig. 16; Nixon *et al.*, 2008).

The growth of the plateau in shallow water led to emplacement of an increasing proportion of volcaniclastics (pillow breccias and hyaloclastites) that accumulated up to 1500 m thick in some areas (Fig. 16b; Nixon *et al.*, 2008). Horizons of pillowed flows occur locally within the volcaniclastic stratigraphy. Sedimentary structures (e.g. graded bedding, fluidization structures) and petrographic textures

within the volcaniclastic rocks indicate formation primarily via cooling–contraction granulation, magma–water–steam interaction, autobrecciation, resedimentation, and mass-wasting, rather than pyroclastic eruption (Nixon *et al.*, 2008).

A broad subaerial platform was constructed by emplacement of subaerial lava flows during an emergent subaerial stage (Fig. 16c). The subaerial unit predominantly comprises well-layered sheet flows that formed in a similar way to continental flood basalts as hundred(s) of pahoehoe flow fields erupted on shallow slopes (Self *et al.*, 1997); however, volcaniclastic and pillowed flow units are locally present, mostly in the upper parts of the stratigraphy. Localized ponding of flows led to the formation of multitiered columnar jointing in some subaerial flows (e.g. Bondre *et al.*, 2004). As volcanism waned, local interflow carbonate deposits developed and plagioclase megacrystic flows were erupted. Subsidence of the plateau is recorded by the interflow lenses and deposits of platform carbonates (40–1500 m thick) on top of the Karmutsen basalts that contain Late Carnian to Early Norian fossils (Fig. 16d; *c.* 216–227 Ma; Nixon *et al.*, 2008).

The evolution of the internal architecture of the Wrangellia oceanic plateau was primarily related to the conditions of emplacement (i.e. water depth and eruption environment). There does not appear to have been a systematic coincident evolution or shift of lava compositions on Vancouver Island, as has been recognized in most continental flood basalts and parts of the Wrangellia oceanic plateau in Alaska and Yukon (Greene *et al.*, 2008, 2009). In general, with the exception of the picritic pillow lavas in the submarine stratigraphy and local variations between high-MgO and tholeiitic lavas, there are no significant compositional differences between lavas erupted during the different stages of growth of the plateau (i.e. submarine and subaerial flows), nor are substantial compositional differences generally found between massive submarine flows in contact with pillowed flows; tholeiitic basalt flows near the base of the Karmutsen Formation are compositionally similar to flows sampled near the top of the volcanic sequence. Where it was possible to sample continuous sections of volcanic stratigraphy greater than several hundreds of meters (e.g. Keogh–Maynard Lake area west of the Karmutsen Range; Fig. 2), there is no clear relationship between stratigraphic position and compositional variation.

CONCLUSIONS

The Karmutsen Formation covers extensive areas of Vancouver Island (~20 000 km^2) and forms part of a large oceanic plateau erupted over a geologically short interval (*c.* 225–231 Ma). The tripartite volcanic stratigraphy exposed on Vancouver Island is at least 6 km thick and comprises a succession of submarine flows, volcaniclastic deposits, and massive subaerial flows. These volcanological differences are primarily related to the eruption environment (deep-water, shallow-water or subaerial). The rapid growth of the plateau prevented significant accumulations of intervening sediment, except in the uppermost stratigraphy where isolated limestone lenses commonly associated with pillow basalt and hyaloclastite deposits preserve a record of the final stages of subsidence of the plateau.

The Wrangellia plateau on Vancouver Island was constructed dominantly of tholeiitic basalt with restricted major- and trace-element, and isotopic, compositional variations. Minor volumes of picritic pillow basalts erupted late in the submarine phase. The Karmutsen basalts were emplaced onto older Paleozoic arc volcanic sequences and low Nb/La for the picrites may indicate a contribution from the sub-arc lithospheric mantle. Modeling of the petrogenesis of the Karmutsen picrites indicates melting of anomalously hot mantle (~1500°C) and extensive degrees of partial melting (23–27%), and is consistent with a plume initiation model. Combined Sr–Nd–Hf–Pb isotopic systematics indicate that the picritic and tholeiitic lavas were derived from a depleted plume-type mantle source distinct from the source of MORB that has compositional similarities to the source of the lavas forming the Caribbean Plateau. Picrites were generated by melting of spinel lherzolite, whereas the tholeiitic basalts formed as aggregate melts of both garnet and spinel lherzolite. The tholeiitic basalts underwent extensive low-pressure fractionation (<2–3 kbar), and seismic studies indicate that some of the Wrangellia crust beneath Vancouver Island may correspond to the plutonic residues of the Karmutsen flood basalts.

ACKNOWLEDGEMENTS

We are grateful to Nick Arndt for helping us get this project started, and Nick Massey for insights into Vancouver Island geology. We greatly appreciate the assistance with PRIMELT modeling from Claude Herzberg. We thank Mikkel Schau for his insight and enthusiasm during fieldwork. Jane Barling assisted with analyses by MC-ICP-MS. Thoughtful and thorough reviews of the manuscript by John Mahoney, Fred Frey, Wendy Bohrson, Dougal Jerram, and Teal Riley are greatly appreciated. Funding was generously provided by the Rocks to Riches Program administered by the BC & Yukon Chamber of Mines in 2004, by the BC Geological Survey, and by NSERC Discovery Grants to J.S.S. and D.W. A.R.G. was supported by a University Graduate Fellowship at UBC.

SUPPLEMENTARY DATA

Supplementary data for this paper are available at *Journal of Petrology* online.

REFERENCES

Barker, F., Brown, A. S., Budahn, J. R. & Plafker, G. (1989). Back-arc with frontal-arc component origin of Triassic Karmutsen basalt, British Columbia, Canada. *Chemical Geology* **75**, 81–102.

Blichert-Toft, J., Weis, D., Maerschalk, C., Agranier, A. & Albarède, F. (2003). Hawaiian hot spot dynamics as inferred from the Hf and Pb isotope evolution of Mauna Kea volcano. *Geochemistry, Geophysics, Geosystems* **4**(2), 1–27, doi:10.1029/2002GC000340.

Bondre, N. R., Duraiswami, R. A. & Dole, G. (2004). Morphology and emplacement of flows from the Deccan Volcanic Province, India. *Bulletin of Volcanology* **66**, 29–45.

Carlisle, D. (1963). Pillow breccias and their aquagene tuffs, Quadra Island, British Columbia. *Journal of Geology* **71**, 48–71.

Carlisle, D. (1972). Late Paleozoic to Mid-Triassic sedimentary-volcanic sequence on Northeastern Vancouver Island. *Geological Society of Canada Paper. Report of Activities* **72-1**, Part B, 24–30.

Carlisle, D. & Suzuki, T. (1974). Emergent basalt and submergent carbonate–clastic sequences including the Upper Triassic Dilleri and Welleri zones on Vancouver Island. *Canadian Journal of Earth Sciences* **11**, 254–279.

Chauvel, C. & Blichert-Toft, J. (2001). A hafnium isotope and trace element perspective on melting of the depleted mantle. *Earth and Planetary Science Letters* **190**, 137–151.

Chayes, F. (1954). The theory of thin-section analysis. *Journal of Geology* **62**, 92–101.

Cho, M., Liou, J. G. & Maruyama, S. (1987). Transition from the zeolite to prehnite–pumpellyite facies in the Karmutsen metabasites, Vancouver Island, British Columbia. *Journal of Petrology* **27**(2), 467–494.

Clowes, R. M., Zelt, C. A., Amor, J. R. & Ellis, R. M. (1995). Lithospheric structure in the southern Canadian Cordillera from a network of seismic refraction lines. *Canadian Journal of Earth Sciences* **32**(10), 1485–1513.

Coffin, M. F. & Eldholm, O. (1994). Large igneous provinces: Crustal structure, dimensions, and external consequences. *Reviews of Geophysics* **32**(1), 1–36.

Cox, K. G. (1980). A model for flood basalt volcanism. *Journal of Petrology* **21**, 629–650.

Eldholm, O. & Coffin, M. F. (2000). Large igneous provinces and plate tectonics. In: Richards, M. A., Gordon, R. G. & van der Hilst, R. D. (eds) *The History and Dynamics of Global Plate Motions. American Geophysical Union, Geophysical Monograph* **121**, 309–326.

Elliott, T. R., Hawkesworth, C. J. & Grönvold, K. (1991). Dynamic melting of the Iceland plume. *Nature* **351**, 201–206.

Escuder-Viruete, J., Pérez-Estaún, A., Contreras, F., Joubert, M., Weis, D., Ullrich, T. D. & Spadea, P. (2007). Plume mantle source heterogeneity through time: Insights from the Duarte Complex, Hispaniola, northeastern Caribbean. *Journal of Geophysical Research* **112**(B04203), doi:10.1029/2006JB004323.

Farnetani, C. G., Richards, M. A. & Ghiorso, M. S. (1996). Petrological models of magma evolution and deep crustal structure beneath hotspots and flood basalt provinces. *Earth and Planetary Science Letters* **143**, 81–94.

Fitton, J. G. & Godard, M. (2004). Origin and evolution of magmas on the Ontong Java Plateau. In: Fitton, J. G., Mahoney, J. J., Wallace, P. J. & Saunders, A. D. (eds) *Origin and Evolution of the Ontong Java Plateau. Geological Society, London, Special Publications* **229**, 151–178.

Fitton, J. G., Saunders, A. D., Norry, M. J., Hardarson, B. S. & Taylor, R. N. (1997). Thermal and chemical structure of the Iceland plume. *Earth and Planetary Science Letters* **153**, 197–208.

Fitton, J. G., Saunders, A. D., Kempton, P. D. & Hardarson, B. S. (2003). Does depleted mantle form an intrinsic part of the Iceland plume? *Geochemistry, Geophysics, Geosystems* **4**(3), 1032, doi:10.1029/2002GC000424.

Frey, F. A., Huang, S., Blichert-Toft, J., Regelous, M. & Boyet, M. (2005). Origin of depleted components in basalt related to the Hawaiian hotspot: Evidence from isotopic and incompatible element ratios. *Geochemistry, Geophysics, Geosystems* **6**(1), 23, doi:10.1029/2004GC000757.

Galer, S. J. G. & Abouchami, W. (1998). Practical application of lead triple spiking for correction of instrumental mass discrimination. *Mineralogical Magazine* **62A**, 491–492.

Ghiorso, M. S. & Sack, R. O. (1995). Chemical mass transfer in magmatic processes, IV. A revised and internally consistent thermodynamic model for the interpolation and extrapolation of liquid–solid equilibria in magmatic systems at elevated temperatures and pressures. *Contributions to Mineralogy and Petrology* **119**, 197–212.

Greene, A. R., Scoates, J. S. & Weis, D. (2005). Wrangellia Terrane on Vancouver Island: Distribution of flood basalts with implications for potential Ni–Cu–PGE mineralization. In: Grant, B. (ed.) *Geological Fieldwork 2004. British Columbia Ministry of Energy, Mines and Petroleum Resources, Paper* **2005-1**, 209–220.

Greene, A. R., Scoates, J. S., Nixon, G. T. & Weis, D. (2006). Picritic lavas and basal sills in the Karmutsen flood basalt province, Wrangellia, northern Vancouver Island. In: Grant, B. (ed.) *Geological Fieldwork 2005. British Columbia Ministry of Energy, Mines and Petroleum Resources, Paper* **2006-1**, 39–52.

Greene, A. R., Scoates, J. S. & Weis, D. (2008). Wrangellia flood basalts in Alaska: A record of plume–lithosphere interaction in a Late Triassic accreted oceanic plateau. *Geochemistry, Geophysics, Geosystems* **9**(Q12004), doi:10.1029/2008GC002092.

Greene, A. R., Scoates, J. S., Weis, D. & Israel, S. (2009). Geochemistry of triassic flood basalts from the Yukon (Canada) segment of the accreted Wrangellia oceanic plateau. *Lithos*, doi:10.1016/j.lithos.2008.11.010.

Hauff, F., Hoernle, K., Tilton, G., Graham, D. W. & Kerr, A. C. (2000). Large volume recycling of oceanic lithosphere over short time scales: geochemical constraints from the Caribbean Large Igneous Province. *Earth and Planetary Science Letters* **174**, 247–263.

Hauff, F., Hoernle, K. & Schmidt, A. (2003). Sr–Nd–Pb composition of Mesozoic Pacific oceanic crust (Site 1149 and 801, ODP Leg 185): Implications for alteration of ocean crust and the input into the Izu–Bonin–Mariana subduction system. *Geochemistry, Geophysics, Geosystems* **4**(8), doi:10.1029/2002GC000421.

Herzberg, C. (2004). Partial melting below the Ontong Java Plateau. In: Fitton, J. G., Mahoney, J. J., Wallace, P. J. & Saunders, A. D. (eds) *Origin and Evolution of the Ontong Java Plateau. Geological Society, London, Special Publications* **229**, 179–183.

Herzberg, C. (2006). Petrology and thermal structure of the Hawaiian plume from Mauna Kea volcano. *Nature* **444**(7119), 605.

Herzberg, C. & Asimow, P. D. (2008). Petrology of some oceanic island basalts: PRIMELT2.XLS software for primary magma calculation. *Geochemistry, Geophysics, Geosystems* **9**(Q09001), doi:10.1029/2008GC002057.

Herzberg, C. & O'Hara, M. J. (2002). Plume-associated ultramafic magmas of Phanerozoic age. *Journal of Petrology* **43**(10), 1857–1883.

Herzberg, C., Asimow, P. D., Arndt, N., Niu, Y., Lesher, C. M., Fitton, J. G., Cheadle, M. J. & Saunders, A. D. (2007). Temperatures in ambient mantle and plumes: Constraints from basalts, picrites, and komatiites. *Geochemistry, Geophysics, Geosystems* **8**(Q02006), doi:10.1029/2006GC001390.

Huang, S. & Frey, F. A. (2005). Trace element abundances of Mauna Kea basalt from phase 2 of the Hawaii Scientific Drilling Project:

Petrogenetic implications of correlations with major element content and isotopic ratios. *Geochemistry, Geophysics, Geosystems* **4**(6), doi:10.1029/2002GC000322.

Hussong, D. M., Wipperman, L. K. & Kroenke, L. W. (1979). The crustal structure of the Ontong Java and Manihiki Oceanic Plateaus. *Journal of Geophysical Research* **84**(B11), 6003–6010.

Jerram, D. A. & Widdowson, M. (2005). The anatomy of Continental Flood Basalt Provinces: geological constraints on the processes and products of flood volcanism. *Lithos* **79**(3–4), 385–405.

Jones, D. L., Silberling, N. J. & Hillhouse, J. (1977). Wrangellia; a displaced terrane in northwestern North America. *Canadian Journal of Earth Sciences* **14**(11), 2565–2577.

Kerr, A. C. (2003). Oceanic Plateaus. In: Rudnick, R. (ed.) *The Crust. Treatise on Geochemistry, Vol. 3*. Oxford: Elsevier Science, pp. 537–565.

Kerr, A. C. & Mahoney, J. J. (2007). Oceanic plateaus: Problematic plumes, potential paradigms. *Chemical Geology* **241**, 332–353.

Kerr, A. C., Tarney, J., Marriner, G. F., Klaver, G. T., Saunders, A. D. & Thirlwall, M. F. (1996). The geochemistry and petrogenesis of the Late-Cretaceous picrites and basalts of Curacao, Netherlands Antilles; a remnant of an oceanic plateau. *Contributions to Mineralogy and Petrology* **124**(1), 29–43.

Kerr, A. C., Marriner, G. F., Tarney, J., Nivia, A., Saunders, A. D., Thirlwall, M. F. & Sinton, A. C. (1997). Cretaceous basaltic terranes in Western Colombia: Elemental, chronological and Sr-Nd isotopic constraints on petrogenesis. *Journal of Petrology* **38**(6), 677–702.

Kinzler, R. J. (1997). Melting of mantle peridotite at pressures approaching the spinel to garnet transition: Application to mid-ocean ridge basalt petrogenesis. *Journal of Geophysical Research* **102**(B1), 853–874.

Kinzler, R. J. & Grove, T. L. (1992). Primary magmas of mid-ocean ridge basalts 1. Experiments and methods. *Journal of Geophysical Research* **97**(B5), 6885–6906.

Korenaga, J. (2005). Why did not the Ontong Java Plateau form subaerially? *Earth and Planetary Science Letters* **234**, 385–399.

Kuniyoshi, S. (1972). Petrology of the Karmutsen (Volcanic) Group, northeastern Vancouver Island, British Columbia. Ph.D. dissertation, University of California, Los Angeles, 242 pp.

Lassiter, J. C., DePaolo, D. J. & Mahoney, J. J. (1995). Geochemistry of the Wrangellia flood basalt province: Implications for the role of continental and oceanic lithosphere in flood basalt genesis. *Journal of Petrology* **36**(4), 983–1009.

LeBas, M. J. (2000). IUGS reclassification of the high-Mg and picritic volcanic rocks. *Journal of Petrology* **41**(10), 1467–1470.

Longhi, J. (2002). Some phase equilibrium systematics of lherzolite melting: I. *Geochemistry, Geophysics, Geosystems* **3**(3), doi:10.1029/2001GC000204.

MacDonald, G. A. & Katsura, T. (1964). Chemical composition of Hawaiian lavas. *Journal of Petrology* **5**, 82–133.

Mahoney, J. J. (1987). An isotopic survey of Pacific oceanic plateaus: implications for their nature and origin. In: Keating, B. H., Fryer, P., Batiza, R. & Boehlert, G. W. (eds) *Seamounts, Islands, and Atolls. American Geophysical Union, Geophysical Monograph* **43**, 207–220.

Mahoney, J., LeRoex, A. P., Peng, Z., Fisher, R. L. & Natland, J. H. (1992). Southwestern limits of Indian Ocean Ridge mantle and the origin of low $^{206}Pb/^{204}Pb$ mid-ocean ridge basalt: isotope systematics of the central Southwest Indian Ridge (17°–50°E). *Journal of Geophysical Research* **97**(B13), 19771–19790.

Mahoney, J. J., Sinton, J. M., Kurz, M. D., MacDougall, J. D., Spencer, K. J. & Lugmair, G. W. (1994). Isotope and trace element characteristics of a super-fast spreading ridge: East Pacific rise, 13–23°S. *Earth and Planetary Science Letters* **121**, 173–193.

Massey, N. W. D. (1995*a*). Geology and mineral resources of the Alberni–Nanaimo Lakes sheet, Vancouver Island 92F/1W, 92F/2E, and part of 92F/7E. *British Columbia Ministry of Energy, Mines and Petroleum Resources, Paper* **1992-2**, 132 pp.

Massey, N. W. D. (1995*b*). Geology and mineral resources of the Cowichan Lake sheet, Vancouver Island 92C/16. *British Columbia Ministry of Energy, Mines and Petroleum Resources, Paper* **1992-3**, 112 pp.

Massey, N. W. D., MacIntyre, D. G., Desjardins, P. J. & Cooney, R. T. (2005*a*). Digital Geology Map of British Columbia: Tile NM9 Mid Coast, B.C. *British Columbia Ministry of Energy and Mines Geofile* **2005-2**.

Massey, N. W. D., MacIntyre, D. G., Desjardins, P. J. & Cooney, R. T. (2005*b*). Digital Geology Map of British Columbia: Tile NM10 Southwest B.C. *British Columbia Ministry of Energy and Mines Geofile* **2005-3**.

McDonough, W. F. & Sun, S. (1995). The composition of the Earth. *Chemical Geology* **120**, 223–253.

Monger, J. W. H. & Journeay, J. M. (1994). Basement geology and tectonic evolution of the Vancouver region. In: Monger, J. W. H. (ed.) *Geology and Geological Hazards of the Vancouver Region, Southwestern British Columbia. Geological Survey of Canada Bulletin* **481**, 3–25.

Muller, J. E. (1977). Geology of Vancouver Island. *Geological Survey of Canada Open File Map* **463.**

Muller, J. E. (1980). *The Paleozoic Sicker Group of Vancouver Island, British Columbia. Geological Survey of Canada, Paper* **79-30**, 22 pp.

Muller, J. E., Northcote, K. E. & Carlisle, D. (1974). Geology and mineral deposits of Alert Bay–Cape Scott map area, Vancouver Island, British Columbia. *Geological Survey of Canada, Paper* **74-8**, 77 .

Neal, C. R., Mahoney, J. J., Kroenke, L. W., Duncan, R. A. & Petterson, M. G. (1997). The Ontong–Java Plateau. In: Mahoney, J. J. & Coffin, M. F. (eds) *Large Igneous Provinces: Continental, Oceanic, and Planetary Flood Volcanism. American Geophysical Union, Geophysical Monograph* **100**, 183–216.

Niu, Y., Collerson, K. D., Batiza, R., Wendt, J. I. & Regelous, M. (1999). Origin of enriched-typed mid-ocean ridge basalt at ridges far from mantle plumes: The East Pacific Rise at 11°20'N. *Journal of Geophysical Research* **104**, 7067–7088.

Nixon, G. T. & Orr, A. J. (2007). Recent revisions to the Early Mesozoic stratigraphy of Northern Vancouver Island (NTS 102I; 092L) and metallogenic implicatinos, British Columbia. In: Grant, B. (ed.) *Geological Fieldwork 2006. British Columbia, Ministry of Energy, Mines and Petroleum Resources, Paper* **2007-1**, 163–177.

Nixon, G. T., Hammack, J. L., Koyanagi, V. M., Payie, G. J., Haggart, J. W., Orchard, M. J., Tozer, T., Friedman, R. M., Archibald, D. A., Palfy, J. & Cordey, F. (2006*a*). Geology of the Quatsino–Port McNeill area, northern Vancouver Island. *British Columbia Ministry of Energy, Mines and Petroleum Resources, Geoscience Map* **2006-2**, scale 1:50 000.

Nixon, G. T., Kelman, M. C., Stevenson, D., Stokes, L. A. & Johnston, K. A. (2006*b*). Preliminary geology of the Nimpkish map area (NTS 092L/07), northern Vancouver Island, British Columbia. In: Grant, B. & Newell, J. M. (eds) *Geological Fieldwork 2005. British Columbia, Ministry of Energy, Mines and Petroleum Resources, Paper* **2006-1**, 135–152.

Nixon, G. T., Laroque, J., Pals, A., Styan, J., Greene, A. R. & Scoates, J. S. (2008). High-Mg lavas in the Karmutsen flood basalts, northern Vancouver Island (NTS 092L): Stratigraphic setting and metallogenic significance. In: Grant, B. (ed.) *Geological Fieldwork 2007. British Columbia, Ministry of Energy, Mines and Petroleum Resources, Paper* **2008-1**, 175–190.

Nowell, G. M., Kempton, P. D., Noble, S. R., Fitton, J. G., Saunders, A., Mahoney, J. J. & Taylor, R. N. (1998). High precision Hf isotope measurements of MORB and OIB by thermal ionisation

mass spectrometry: insights into the depleted mantle. *Chemical Geology* **149**, 211–233.

Parrish, R. R. & McNicoll, V. J. (1992). U–Pb age determinations from the southern Vancouver Island area, British Columbia. In: *Radiogenic Age and Isotopic Studies: Report 5. Geological Survey of Canada, Paper* **91-2**, 79–86.

Peate, D. W. (1997). The Parana–Etendeka Province. In: Coffin, M. F. & Mahoney, J. (eds) *Large Igneous Provinces: Continental, Oceanic, and Planetary Flood Volcanism. American Geophysical Union, Geophysical Monograph* **100**, 217–245.

Perfit, M. R., Fornari, D. J., Ridley, W. I., Kirk, P. D., Casey, J., Kastens, K. A., Reynolds, J. R., Edwards, M., Desonie, D., Shuster, R. & Paradis, S. (1996). Recent volcanism in the Siqueiros transform fault: picritic basalts and implications for MORB magma genesis. *Earth and Planetary Science Letters* **141** (1–4), 91–108.

Pretorius, W., Weis, D., Williams, G., Hanano, D., Kieffer, B. & Scoates, J. S. (2006). Complete trace elemental characterization of granitoid (USGSG-2,GSP-2) reference materials by high resolution inductively coupled plasma-mass spectrometry. *Geostandards and Geoanalytical Research* **30** (1), 39–54.

Regelous, M., Niu, Y., Wendt, J. I., Batiza, R., Greig, A. & Collerson, K. D. (1999). Variations in the geochemistry of magmatism on the East Pacific Rise at 10°30'N since 800 ka. *Earth and Planetary Science Letters* **168**, 45–63.

Révillon, S., Chauvel, C., Arndt, N. T., Pik, R., Martineau, F., Fourcade, S. & Marty, B. (2002). Heterogeneity of the Caribbean plateau mantle source: Sr, O and He isotopic compositions of olivine and clinopyroxene from Gorgona Island. *Earth and Planetary Science Letters* **205** (1–2), 91.

Rhodes, J. M. (1996). Geochemical stratigraphy of lava flows samples by the Hawaii Scientific Drilling Project. *Journal of Geophysical Research* **101** (B5), 11729–11746.

Rhodes, J. M. & Vollinger, M. J. (2004). Composition of basaltic lavas sampled by phase-2 of the Hawaii Scientific Drilling Project: Geochemical stratigraphy and magma types. *Geochemistry, Geophysics, Geosystems* **5** (3), doi:10.1029/2002GC000434.

Richards, M. A., Jones, D. L., Duncan, R. A. & DePaolo, D. J. (1991). A mantle plume initiation model for the Wrangellia flood basalt and other oceanic plateaus. *Science* **254**, 263–267.

Salters, V. J. M. & Hart, S. R. (1991). The mantle sources of ocean ridges, islands and arcs: the Hf-isotope connection. *Earth and Planetary Science Letters* **104**, 364–380.

Salters, V. J. M. & Stracke, A. (2004). Composition of the depleted mantle. *Geochemistry, Geophysics, Geosystems* **5** (Q05B07), doi:10.1029/2003GC000597.

Salters, V. J. & White, W. (1998). Hf isotope constraints on mantle evolution. *Chemical Geology* **145**, 447–460.

Sano, T. & Yamashita, S. (2004). Experimental petrology of basement lavas from Ocean Drilling Program Leg 192: implications for differentiation processes in Ontong Java Plateau magmas. In: Fitton, J. G., Mahoney, J. J., Wallace, P. J. & Saunders, A. D. (eds) *Origin and Evolution of the Ontong Java Plateau. Geological Society, London, Special Publications* **229**, 185–218.

Saunders, A. D. (2005). Large igneous provinces: Origin and environmental consequences. *Elements* **1**, 259–263.

Self, S., Thordarson, T. & Keszthely, L. (1997). Emplacement of continental flood basalt lava flows. In: Mahoney, J. J. & Coffin, M. F. (eds) *Large Igneous Provinces: Continental, Oceanic, and Planetary Flood Volcanism. American Geophysical Union, Geophysical Monograph* **100**, 381–410.

Shaw, D. M. (2000). Continuous (dynamic) melting theory revisited. *Canadian Mineralogist* **38** (5), 1041–1063.

Sluggett, C. L. (2003). Uranium–lead age and geochemical constraints on Paleozoic and Early Mesozoic magmatism in Wrangellia Terrane, Saltspring Island, British Columbia. B.Sc. thesis, University of British Columbia, Vancouver, 84 pp.

Storey, M., Mahoney, J. J. & Saunders, A. D. (1997). Cretaceous basalts in Madagascar and the transition between plume and continental lithospheric mantle sources. In: Mahoney, J. J. & Coffin, M. F. (eds) *Large Igneous Provinces: Continental, Oceanic, and Planetary Flood Volcanism. Aamerican Geophysical Union, Geophysical Monograph* **100**, 95–122.

Surdam, R. C. (1967). Low-grade metamorphism of the Karmutsen Group. Ph.D. dissertation, University of California, Los Angeles, 288 pp.

Sutherland-Brown, A., Yorath, C. J., Anderson, R. G. & Dom, K. (1986). Geological maps of southern Vancouver Island, LITHOPROBE I 92C/10, 11, 14, 16, 92F/1, 2, 7, 8. *Geological Survey of Canada, Open File* **1272**.

Tejada, M. L. G., Mahoney, J. J., Castillo, P. R., Ingle, S. P., Sheth, H. C. & Weis, D. (2004). Pin-pricking the elephant: evidence on the origin of the Ontong Java Plateau from Pb–Sr–Hf–Nd isotopic characteristics of ODP Leg 192 basalts. In: Fitton, J. G., Mahoney, J. J., Wallace, P. J. & Saunders, A. D. (eds) *Origin and Evolution of the Ontong Java Plateau. Geological Society, London, Special Publications* **229**, 133–150.

Thompson, P. M. E., Kempton, P. D. & Kerr, A. C. (2008). Evaluation of the effects of alteration and leaching on Sm–Nd and Lu–Hf systematics in submarine mafic rocks. *Lithos* **104** (1–4), 164–176.

Thompson, P. M. E., Kempton, P. D., White, R. V., Kerr, A. C., Tarney, J., Saunders, A. D., Fitton, J. G. & McBirney, A. (2003). Hf-Nd isotope constraints on the origin of the Cretaceous Caribbean plateau and its relationship to the Galapagos plume. *Earth and Planetary Science Letters* **217** (1–2), 59–75.

Vervoort, J. D., Patchett, P., Blichert-Toft, J. & Albarède, F. (1999). Relationships between Lu–Hf and Sm–Nd isotopic systems in the global sedimentary system. *Earth and Planetary Science Letters* **168**, 79–99.

Walter, M. J. (1998). Melting of garnet peridotite and the origin of komatiite and depleted lithosphere. *Journal of Petrology* **39** (1), 29–60.

Weis, D., Kieffer, B., Maerschalk, C., Barling, J., de Jong, J., Williams, G. A., Hanano, D., Mattielli, N., Scoates, J. S., Goolaerts, A., Friedman, R. A. & Mahoney, J. B. (2006). High-precision isotopic characterization of USGS reference materials by TIMS and MC-ICP-MS. *Geochemistry, Geophysics, Geosystems* **7** (Q08006), doi:10.1029/2006GC001283.

Weis, D., Kieffer, B., Hanano, D., Silva, I. N., Barling, J., Pretorius, W., Maerschalk, C. & Mattielli, N. (2007). Hf isotope compositions of U.S. Geological Survey reference materials. *Geochemistry, Geophysics, Geosystems* **8** (Q06006), doi:10.1029/2006GC001473.

Wheeler, J. O. & McFeely, P. (1991). Tectonic assemblage map of the Canadian Cordillera and adjacent part of the United States of America. *Geological Survey of Canada Map* **1712A.**

White, W. M., Albarède, F. & Télouk, P. (2000). High-precision analysis of Pb isotope ratios by multi-collector ICP-MS. *Chemical Geology* **167**, 257–270.

Yorath, C. J., Sutherland Brown, A. & Massey, N. W. D. (1999). *LITHOPROBE, southern Vancouver Island, British Columbia. Geological Survey of Canada Bulletin* **498**, 145 pp.

Zou, H. (1998). Trace element fractionation during modal and non-model dynamic melting and open-system melting: A mathematical treatment. *Geochimica et Cosmochimica Acta* **62** (11), 1937–1945.

Zou, H. & Reid, M. R. (2001). Quantitative modeling of trace element fractionation during incongruent dynamic melting. *Geochimica et Cosmochimica Acta* **65**(1), 153–162.

APPENDIX: SAMPLE PREPARATION AND ANALYTICAL METHODS

Only the freshest rocks in the field were sampled and only the least altered samples were selected for chemical and isotopic analysis based on thorough petrographic inspection. Fifty-nine of the 129 collected samples were crushed (400 g) into small pieces <2 mm in diameter in a Rocklabs hydraulic piston crusher between WC plates to minimize contamination. The coarse-crush was mixed and 100 g was powdered in a planetary mill using agate jars and balls cleaned with quartz sand between samples.

ActLabs analytical methods

The major- and trace-element compositions of the whole-rock powders were determined at Activation Laboratories Ltd. (Actlabs) in Ancaster, Ontario. Analytical techniques and detection limits are also available from Actlabs (http://www.actlabs.com/methsub.code4ere.htm). The analytical method for each of the elements analyzed is indicated in Table 2. For the major elements, a 0·2 g sample was mixed with a lithium metaborate–lithium tetraborate mixture and fused in a graphite crucible. The molten mixture was poured into a 5% HNO_3 solution and shaken until dissolved ($\sim$30 min). The samples were analyzed for major oxides and selected trace elements by inductively coupled plasma optical emission spectrometry (ICP-OES) on a combination simultaneous–sequential Thermo Jarrell-Ash Enviro II system. Internal calibration was achieved using a variety of international reference materials (e.g. W-2, BIR-1, DNC-1) and independent control samples. Additional trace elements were analyzed by both instrumental neutron activation analysis (INAA) and inductively couple plasma mass spectrometry (ICP-MS). For INAA, 1·5–2·5 g of sample was weighed into small polyethylene vials and irradiated with a control international reference material CANMET WMS-1 and NiCr flux wires at a thermal neutron flux of 7×10^{12} neutrons/cm^2 per s in the McMaster Nuclear Reactor. Following a 7 day waiting period, the samples were measured on an Ortec high-purity Ge detector linked to a Canberra Series 95 multichannel analyzer. Activities for each element were decay- and weight-corrected and compared with a detector calibration developed from multiple international certified reference materials. For ICP-MS, 0·25 g of sample was digested in HF, followed by HNO_3–$HClO_4$, heated and taken to dryness. The samples were brought back into solution with HCl. Samples were analyzed using a Perkin Elmer Optima 3000 ICP. In-lab standards or certified reference materials (e.g. W-2, BIR-1, DNC-1) were used for quality control. A total of 15 blind duplicates were analyzed from the same sample powders to assess reproducibility.

University of Massachusetts analytical methods

Fourteen sample duplicate powders taken from the same 100 g sample aliquot (high-MgO basalts and picrites) were also analyzed at the Ronald B. Gilmore X-Ray Fluorescence (XRF) Laboratory at the University of Massachusetts. Major elements were measured on a fused La-bearing lithium borate glass disc using a Siemens MRS-400 spectrometer. Trace element concentrations (Rb, Sr, Ba, Ce, Nb, Zr, Y, Pb, Zn, Ga, Ni, Cr, V) were measured on a separate powder pellet using a Philips PW2400 sequential spectrometer using a Rh tube. LOI and ferrous iron measurements were made as described by Rhodes & Vollinger (2004). Precision and accuracy estimates for the data have been described by Rhodes (1996) and Rhodes & Vollinger (2004). Results for each sample are the average of two separate analyses and are shown in Electronic Appendix 2, for a comparison of analyses of duplicate powders using XRF and ICP-MS.

PCIGR analytical methods

A subset of 19 samples was selected for high-precision trace-element analysis and Sr, Nd, Pb, and Hf isotopic analysis at the Pacific Centre for Isotopic and Geochemical Research (PCIGR) at the University of British Columbia (UBC). Samples were selected from the 59 samples analyzed for whole-rock chemistry at ActLabs, based on major- and trace-element chemistry, alteration (low LOI and petrographic alteration index), and sample location. Samples were prepared for trace-element analysis at the PCIGR by the technique described by Pretorius *et al.* (2006) on unleached rock powders. Sample powders ($\sim$100 mg) were weighed in 7 ml screw-top Savillex® beakers and dissolved in 1 ml $\sim$14N HNO_3 and 5 ml 48% HF on a hotplate for 48 h at 130°C with periodic ultrasonication. Samples were dried and redissolved in 6 ml 6N HCl on a hotplate for 24 h and then dried and redissolved in 1 ml concentrated HNO_3 for 24 h before final drying. Trace element abundances were measured by high-resolution inductively coupled plasma-mass spectrometry (HR-ICP-MS) with a Thermo Finnigan Element2 system, following the procedures described by Pretorius *et al.* (2006), within 24 h of redissolution. HFSE and LILE were measured in medium-resolution mode at 2000× dilution using a PFA Teflon spray chamber washed with aqua regia for 3 min between samples. REE were measured in high-resolution mode, and U and Pb in low-resolution mode, at 2000× dilution using a glass spray chamber washed with 2% HNO_3 between samples. Total procedural blanks and reference materials (BCR-2, BHVO-2) were analyzed with the batch of samples. Indium was used as an internal

standard in all samples and standard solutions. Background and standard solutions were analyzed after every five samples to detect memory effects and mass drift. Results for PCIGR trace-element analyses are shown in Electronic Appendix 3 for the full set of analyzed trace elements.

Sample digestion for purification of Sr, Nd, Hf, and Pb for column chemistry began by weighing each sample powder (400–500 mg) prior to leaching. All samples were leached with 6N HCl and placed in an ultrasonic bath for 15 min. Samples were rinsed twice with 18 MΩ-cm H_2O between each leaching step (15 total) until the supernatant liquid was clear [following the method of Mahoney (1987)]. Samples were then dried on a hotplate for 24 h and weighed again. Sample solutions were then prepared by dissolving ~100–250 mg of the leached powder dissolved in 1 ml ~14N HNO_3 and 10 ml 48% HF on a hotplate for 48 h at 130°C with periodic ultrasonication. Samples were dried and redissolved in 6 ml 6N HCl on a hotplate for 24 h and then dried. Pb was separated using anion exhange columns and the discard was used for Sr, REE, and Hf separation. Nd was separated from the other REE and Hf required two additional purification steps. Detailed procedures for column chemistry for separating Sr, Nd, and Pb at the PCIGR have been described by Weis *et al.* (2006) and Hf purification has been described by Weis *et al.* (2007). Sr and Nd isotope ratios were measured by thermal ionization mass spectrometry (TIMS) on a Thermo Finnigan Triton system in static mode with relay matrix rotation on a single Ta and double Re–Ta filament, respectively. Four to five filaments per barrel of 21 were occupied by standards (NBS 987 for Sr and LaJolla for Nd) for each barrel where samples were run. Sample Sr and Nd isotopic compositions were corrected for mass fractionation using $^{86}Sr/^{88}Sr = 0{\cdot}1194$ and $^{146}Nd/^{144}Nd = 0{\cdot}7219$. Each sample was then normalized using the barrel average of the reference material relative to the values of $^{143}Nd/^{144}Nd = 0{\cdot}511858$ and $^{87}Sr/^{86}Sr = 0{\cdot}710248$ (Weis *et al.*, 2006). During the course of the Vancouver Island analyses, the La Jolla Nd standard gave an average value of $0{\cdot}511856 \pm 6$ ($n = 7$) and NBS987 standard gave an average of $0{\cdot}710240 \pm 8$ ($n = 11$) (2σ error is reported as times 10^6). $^{147}Sm/^{144}Nd$ errors are ~1·5%, or ~0·006. US Geological Survey (USGS) reference material BHVO-2 was processed with the samples and yielded Sr and Nd isotopic ratios of $0{\cdot}703460 \pm 7$ and $0{\cdot}512978 \pm 6$, respectively. These are in agreement with the published values of $0{\cdot}703479 \pm 20$ and $0{\cdot}512984 \pm 11$, respectively (Weis *et al.*, 2006).

Pb and Hf isotopic compositions were analyzed by multiple collector-inductively coupled plasma-mass spectrometry (MC-ICP-MS) on a static multi-collection on a Nu Plasma (Nu Instruments) system. The detailed analytical procedure for Pb isotopic analyses on the Nu Plasma at the PCIGR has been described by Weis *et al.* (2006). The configuration for Pb analyses allows for collection of Pb, Tl, and Hg together. Tl and Hg are used to monitor instrumental mass discrimination and isobaric overlap, repectively. All sample solutions were analyzed with approximately the same Pb/Tl ratio (~4) as the reference material NIST SRM 981. To accomplish this, a small aliquot of each sample solution from the Pb columns was analyzed on the Element2 to determine the precise amount of Pb available for analysis on the Nu Plasma. The SRM 981 standard was run after every two samples on the Nu Plasma. During the time samples were run, analyses of the SRM 981 Pb reference material gave values of $^{206}Pb/^{204}Pb = 16{\cdot}9403 \pm 22$, $^{207}Pb/^{204}Pb = 15{\cdot}4958 \pm 23$, and $^{208}Pb/^{204}Pb = 36{\cdot}7131 \pm 64$ ($n = 61$; 2σ error is reported as times 10^4); these values are in excellent agreement with reported TIMS triple-spike values of Galer & Abouchami (1998). Fractionation-corrected Pb isotopic ratios were further corrected by the sample-standard bracketing method or the ln–ln correction method described by White *et al.* (2000) and Blichert-Toft *et al.* (2003). Leached powders of USGS reference material BHVO-2 yielded Pb isotopic ratios of $^{206}Pb/^{204}Pb = 18{\cdot}6454 \pm 8$, $^{207}Pb/^{204}Pb = 15{\cdot}4910 \pm 5$, and $^{208}Pb/^{204}Pb = 38{\cdot}2225 \pm 14$, and BCR-2 yielded $^{206}Pb/^{204}Pb = 18{\cdot}8046 \pm 6$, $^{207}Pb/^{204}Pb = 15{\cdot}6251 \pm 8$, and $^{208}Pb/^{204}Pb = 38{\cdot}8349 \pm 6$ (2σ error is reported as times 10^4). These values are in agreement with those for leached residues of BHVO-2 and BCR-2 from Weis *et al.* (2006).

Hf isotopic compositions were analyzed following the procedures detailed by Weis *et al.* (2007). The configuration for Hf analyses monitored Lu mass 175 and Yb mass 172 to allow for interference correction to masses 174 and 176. Hf isotopic ratios were normalized internally for mass fractionation to a $^{179}Hf/^{177}Hf$ ratio of 0·7325 using an exponential correction. Standards were run after every two samples and sample results were normalized to the ratio of the in-run daily average and a $^{176}Hf/^{177}Hf$ ratio for JMC-475 of 0·282160. During the course of analyses, the Hf standard JMC-475 gave an average value $0{\cdot}282167 \pm 9$ ($n = 130$). USGS reference materials BCR-2 and BHVO-2 were processed with the samples and yielded Hf isotopic ratios of $0{\cdot}282867 \pm 5$ and $0{\cdot}283100 \pm 5$, respectively. Published values for BCR-2 and BHVO-2 are $0{\cdot}282871 \pm 7$ and $0{\cdot}283104 \pm 8$, respectively (Weis *et al.*, 2007).